technische universität
dortmund

On the structural evolution towards germanene

A photoemission study of the structural formation of a 2D material at the surface and interface

Dissertation

submitted in partial fulfillment of the requirements
for the degree of

doctor rerum naturalium
(Dr. rer. nat.)

of the Department of Physics
TU Dortmund University, Germany

by

Lukas Kesper
born in Lünen, Germany

- 2022 -

A dissertation submitted to the department of physics of TU Dortmund University in partial fulfillment of the requirements for the degree of doctor of science.

First corrector:	Prof. Dr. Carsten Westphal
Second corrector:	Prof. Dr. Roland Böhmer
Head of commission:	Prof. Dr. Johannes Albrecht
Representative of scientific staff:	Dr. Jens Weingarten
Date of submission:	30.09.2022
Date of disputation:	30.11.2022

Abstract

In the past decade, research on 2D materials has expanded massively due to the popularity of graphene. Its superb electronic and mechanical properties have attracted attention, which opened a new field in solid-state physics. Various elements of the carbon group IVA and beyond have been proven to be stable in a single monolayer (ML) formed in a honeycomb structure. Although the chemical engineering of two-dimensional elemental materials and heterostructures has been extensively pursued, the fundamental understanding of the synthesis of 2D materials is not yet complete. Structural parameters, such as the corrugation of the honeycomb lattice, called buckling, or the interface structure of a 2D material to the substrate, directly influence its electronic characteristics.

In order to proceed with understanding the element-specific growth, this work presents a study on the structural evolution of the promising 2D material germanene on Ag(111). It provides a survey of germanium formations discovered at different layer thicknesses, like the Ag_2Ge surface alloy (SAP), the striped phase (SP), and the mixed phase (MP), right up to the arising of quasi-freestanding germanene (QFG). Using robust surface analysis tools like low-energy electron diffraction (LEED), the long-range and high order of the epitaxially grown Ge structures are demonstrated. The internal and interfacial structure of all germanene phases is revealed by utilizing high-resolution x-ray photoelectron spectroscopy (XPS) with synchrotron radiation. Furthermore, a clear distinction between all phases can be drawn by their electronic structure, the same as collecting evidence for chemically freestanding germanene synthesized on Ag(111). The additionally performed x-ray photoelectron diffraction (XPD) allows to present specific models of the atomic and chemical structure of selected germanene phases, focusing on the structural parameters and electronic interaction at the interfaces. Moreover, the SAP is encapsulated with a capping layer of Al_2O_3 in order to examine its structural development as a buried interlayer upon the encapsulation.

This work offers a perspective on synthesizing promising germanene phases on Ag(111) and provides a prospect to protect the structures from ambient conditions.

Kurzfassung

In den letzten Jahren hat sich die Forschung zu 2D-Materialien aufgrund der Popularität von Graphen massiv ausgeweitet. Die erstaunlichen elektronischen und mechanischen Eigenschaften von Graphen haben Aufmerksamkeit erweckt und einen neuen Bereich der Festkörperphysik eröffnet. Es zeigte sich, dass verschiedene Elemente der Gruppe IVA und darüber hinaus in nur einer Monolage (ML) als Honigwabenstruktur stabil sind. Obwohl das *chemical engineering* zweidimensionaler Elementmaterialien sowie das von Heterostrukturen intensiv vorangetrieben wurde, ist das grundlegende Verständnis der Synthese von 2D-Materialien noch nicht vollständig. Strukturelle Parameter, wie die Welligkeit des Wabengitters, das sogenannte *buckling*, oder die Grenzflächenstruktur eines 2D-Materials zum Substrat, wirken sich direkt auf seine elektronischen Eigenschaften aus.
Um das Verständnis des elementspezifischen Wachstums voranzutreiben, wird in dieser Arbeit eine Studie über die strukturelle Entwicklung des vielversprechenden 2D-Materials Germanen auf Ag(111) präsentiert. Sie bietet einen Überblick über Germaniumformationen, die bei verschiedenen Schichtdicken entstehen, wie die Ag_2Ge -Oberflächenlegierung (SAP), die *striped* Phase (SP) und die gemischte Phase (MP), bis hin zu quasi-freistehendem Germanen (QFG). Mit Hilfe bewährter Oberflächenanalysemethoden, wie der niederenergetischen Elektronenbeugung (LEED), wird die langreichweitige und hohe Ordnung der epitaktisch gewachsenen Ge-Strukturen nachgewiesen. Mittels hochauflösender Photoelektronenspektroskopie (XPS) mit Synchrotronstrahlung wird die interne Struktur und Grenzflächenstruktur aller Germanen-Phasen aufgelöst. Zudem kann die klare Unterscheidung zwischen allen Phasen anhand ihrer elektronischen Struktur gezeigt und der Nachweis von chemisch freistehendem Germanen auf Ag(111) erbracht werden. Die zusätzlich durchgeführte Photoelektronenbeugung (XPD) ermöglicht die Darstellung spezifischer Strukturmodelle ausgewählter Germanenphasen mit besonderem Augenmerk auf die strukturellen Parameter und elektronischen Wechselwirkungen an der Grenzfläche. Außerdem wird die SAP mit einer Deckschicht aus Al_2O_3 bedeckt, um seine strukturelle Entwicklung als verborgene Zwischenschicht zu untersuchen.
Diese Arbeit bietet einen Ausblick auf die Synthese vielversprechender Germanenphasen auf Ag(111) und zeigt die Möglichkeit, diese Strukturen vor Umgebungsbedingungen zu schützen.

Chapter

Contents

Chapter

List of Acronyms

ARPES	Angle-resolved photoelectron spectroscopy	20, 64
ARXPS	Angle-resolved x-ray photoelectron spectroscopy	21, 71
BG	Background of XPS spectra	25
BL11	Beamline 11 at DELTA	43, 51, 52, 64
BM	Bending magnets	52
BoDo	Booster Dortmund, pre-accelerator of DELTA	52
BZ	Brillouin zone	8, 58
CEM	Channel electron multiplier	49, 50
DELTA	Electron storage ring, Center for Synchrotron Radiation (Dortmund, Germany)	43, 52, 101
DFT	Density-functional theory	5, 9
DS	Doniach-Sunjic profile	28, 68, 75
EB	Electron beam heating mode	46, 47, 58
EED	Effective escape depth	21, 65
ESCA	Electron spectroscopy for chemical analysis	13
fcc	Face-centered cubic crystal structure	57, 74
FEL	Free-electron laser	52

FET	Field effect transistor	1, 92
FV	Fore-vacuum	44
FWHM	Full width half maximum	22, 26
HAXPS	Hard x-ray photoelectron spectroscopy	11
hcp	Hexagonal closed packed crystal structure	74
HEA	Hemispherical energy analyzer	49
HighRes	High energy-resolution XPS spectra	21, 34, 64, 101
ID	Information depth	21
IMFP	Inelastic mean free path	16, 18, 65
LEED	Low-energy electron diffraction	39, 48, 101
LINAC	Linear accelerator, *here:* pre-accelerator of DELTA	52
MED	Mean escape depth	21
ML	Monolayer	5, 60
MP	Mixed phase	61, 78, 80, 102
NEG	Non-evaporable getter pump	44
PES	Photoelectron spectroscopy	11, 12, 20
PGM	Plane-grating monochromator	54
PVD	Physical vapor deposition	7, 47, 58, 101
QCM	Quartz crystal microbalance	59

QFG	Quasi-freestanding germanene	61, 78, 80, 83, 102
QHE	Quantum Hall effect	8
QSHE	Quantum spin Hall effect	3
RES	Resistive heating mode	46, 57
RT	Room temperature	8
SAP	Ag_2Ge surface alloy phase	61, 63, 67, 78, 92, 101
SCW	Superconducting Wiggler	52
SOC	Spin-orbit coupling	23
SP	Striped phase	61, 74, 80, 102
TSP	Titanium sublimation pump	44
U250	Undulator 250 of DELTA	52
U55	Undulator 55 of DELTA	52
UHV	Ultra-high vacuum	43
UPS	Ultraviolet photoelectron spectroscopy	11, 20
VB	Valence band	13, 101
VdW	Van der Waals	5, 102
XPD	X-ray photoelectron diffraction	20, 31, 63, 101
XPS	X-ray photoelectron spectroscopy	11, 13, 63, 101

Chapter

List of Symbols

a	lattice constant	6
α	Asymmetry parameter	28
A_{rel}	Relative area of a component in a XPS HighRes spectrum	66
χ^{2^*}	Reduced chi-squared	29
d	nearest neighbor distance	6, 7
δ	buckling parameter of a corrugated honeycomb lattice	6
d_z	Spacing between crystal planes	65
E_{bin}	Binding energy	13
E_{chem}	Chemical shift	24
E_{F}	Fermi energy, Fermi edge, Fermi level	13
E_{vac}	Vacuum level of a solid	13
E_{g}	Energy gap of band structures	8
E_{kin}	Kinetic energy	13, 48, 49
E_{pass}	Pass energy of the hemispherical energy analyzer	49
E_{SOC}	Spin-orbit splitting	22, 23
hν	photon energy: Planck constant times frequency of light	13

I_{em}	Emission current inside the electron beam evaporator	47
$\vec{k}$	Wavevector	8, 16, 32
κ	Film thickness of an epitaxially grown adsorbate	59
l_{ac}	Periodic length of a honeycomb structure along the armchair direction	9
λ	Inelastic mean free path IMFP	16, 18
Λ	Coverage of a surface by epitaxial growth	59
m_{e}	Proper mass of an electron	39
P_{em}	Evaporation power of the electron beam evaporator	47
Φ	Azimuthal angle of sample rotation around its surface normal	20, 46
Φ	Work funktion	13
r_{scat}	Scattering radius of photoelectron emitter (XPD)	37
Θ	PES emission angle/polar angle regarding the surface normal	20, 46
Θ_{HEA}	Acceptance angle of the hemispherical energy analyzer	16, 49
U_{HV}	High voltage inside the electron beam evaporator	47
V_0	Inner potential of a solid	33

Chapter

List of Figures

Chapter

List of Tables

Chapter 1

Introduction

Every once in a while, a new
technology, an old problem, and a
big idea turn into an innovation.

attributed to Dean Kamen

Technology is the driving force for progress in modern times. Physical science, especially materials research in solid state physics, significantly contributed to this, as exemplified by the development of the transistor [1]. Incorporating of silicon-based semiconductor devices in integrated circuits was a great leap towards handy high-performance devices. Silicon technology has become indispensable in the information society as silicon represents the fundamental building block of electronic devices nowadays. Not least because of this, silicon lends its name to the world's most innovative technology campus.

In the past decades, the downscaling of silicon-based microprocessors, sensors, and memory chips rose in order to magnify the power and performance of electronic devices. In 1965, Gordon Moore proposed that the number of transistors incorporated in integrated circuits would increase exponentially [2]. Using dimensional and equivalent scaling processes, feature sizes of electronic constituents like gate lengths of field effect transistors (FET) of about 7 nm could be fabricated [3]. However, the physical limit of downscaling feature sizes of silicon-based devices is proposed to be approximately 5 nm since interfering quantum effects take effect. A prospect of preventing the end of Moore's law was delivered with a new class of materials, called 2D materials [4, 5]. The first synthesis of freestanding graphene and the experimental proof of its predicted, outstanding electronic properties [6, 7] paved the way for next-generation computation technology [8].

Graphene was the first synthesized two-dimensional (2D) material consisting of an atomically thin, planar honeycomb layer of carbon atoms [6]. Exceptionally high charge carrier mobilities and outstanding thermal and electric conductivities arise from electrons propagating over large distances through graphene without electron-phonon scattering [6, 9, 10]. In addition to its optical absorption spectrum, graphene's electronic properties are desirable for improving devices based on metal oxide semiconductor field effect transistors (MOSFET) and complementary metal oxide semiconductors (CMOS) [8, 11]. Since transistors require semiconducting materials, graphene as a zero-band gap semiconductor, is not capable of replacing silicon, at all.
Shortly after the theoretical prediction of 2D materials beyond graphene [12, 13], silicene and germanene as the two-dimensional counterparts of silicon and germanium, respectively, were synthesized [14, 15]. These materials often referred as *Xenes*, show similar electronic properties as graphene's, such as the presence of charge carriers behaving as massless Dirac fermions and linear energy dispersions [13]. Due to a corrugated honeycomb arrangement, called buckling, instead of planar layers, 2D materials beyond graphene showed rather semiconducting than metallic behavior. Thus, it makes them promising candidates for new-generation transistors and computing technology [8, 16–18]. Apart from the multitude of graphene-based applications [19], also outstandingly performing silicene- and germanene-based transistors with high-mobility charge carriers have been recently realized [20–22]. Joining Xenes, like stanene [23], plumbene [24], gallenene [25], phosphorene [26], *et cetera*, but also heterostructures and functionalized Xenes were added to the set of 2D materials, foreshadowing a broader field of applications [27–31]. Even the kick-off for the fabrication of 2D material-based devices occurred through the progress in large-scale synthesis of the related materials and the on-chip implementation [32, 33]. Since the challenges of fabricating 2D material devices are getting less, prospects of sub-nanotechnology are steadily taking shape [34]. However, as intensive efforts are still underway to optimize electronic devices made of 2D materials, research into the synthesis and structural properties of Xenes plays an essential role in progress.

This work examines the structural formation stages of germanene in more detail. Germanene was initially predicted to exist in 2009 [13] and was firstly synthesized by epitaxial growth on Pt(111) and Au(111) in 2014 [15, 35]. In contrast to the previously fabricated silicene, whose Dirac characteristic is still the subject of controversial

discussions [36–40], Dirac cones in germanene's band structure have been predicted theoretically and proven experimentally [13, 41–43]. Intriguingly, the corresponding massless Dirac fermions in germanene are able to reach mobilities twice as high as metal-like graphene [44] since its band gap can be additionally tuned by an external electric field [13, 45]. Even though germanene turned out to be an auspicious material for new-generation electronics, it still has not been achieved to synthesize freestanding germanene sheets. Due to its weakened in-plane bonds, it is recommended to grow germanene on metallic substrates [46]. However, the structural and chemical properties of the carrier substrate strongly influence the structural formation of the on-growing 2D material. Lattice mismatches between substrate and adsorbate and external strain have a sublime impact on structural parameters, such as the lattice constant a or the buckling parameter δ of the grown layer, as observed for various 2D materials [47–49]. The desirable electronic properties of freestanding germanene prospected for applications are modified by altered structural parameters much the same as a strong interaction between the substrate and the 2D material, like a thriving charge transfer at the interface. One way of gaining the ability to preserve and tune the electronic properties of freestanding germanene is to take hold of structural key parameters, for example, the buckling and the interface structure, by choosing a suitable substrate [16, 50]. As a high buckling of the honeycomb lattice leads to a large band gap in germanene's band structure [51, 52], a low-buckled germanene phase is also of great interest. In such a phase, the respective band gap is still larger than silicene's, which allows the realization of the quantum spin Hall effect (QSHE) [53].

Ag(111) turned out to be an encouraging candidate for synthesizing freestanding-like germanene by considering predictions of Dirac cones in germanene on Ag [41], as well as moderate interaction and poor charge transfer at the interface compared to other substrates [15, 46, 54]. Thus, the structural investigation of the germanene/Ag(111) sample system is key for enhancing the understanding of the structural formation mechanism of 2D materials but also for drawing a roadmap for germanene-based electronic devices with customized properties [55]. Recent studies on this system found a variety of phases formed on Ag(111) at different germanium coverages, which can be assigned to different stages of the structural evolution of germanene. The first experimental study of thin films epitaxially grown germanium on Ag(111) mainly reported a surface alloy formes at a coverage of 1/3 ML, arranged in a

$\left(\sqrt{3} \times \sqrt{3}\right)$ R30° reconstruction [56, 57]. However, this Ag_2Ge alloy phase at a layer thickness of 1/3 ML germanium is still controversially discussed in literature to either form reconstructions of a $\left(\sqrt{3} \times \sqrt{3}\right)$ R30° [58–60], a $\left(9\sqrt{3} \times 9\sqrt{3}\right)$ R30° [61], or a rectangular Rec $\left\{c\left(31 \times \sqrt{3}\right)\right\}$ [62]. It was also consideres as a striped phase due to tensile strains of the uppermost layer [63] with a long-range order of $\left(6\sqrt{3} \times \sqrt{3}\right)$ R30° [59]. The following germanium assembly is called a mixed phase, as a superposition of a coexisting $\left(\sqrt{3} \times \sqrt{3}\right)$ phase and a quasi-freestanding germanene formation with sharp domain edges [63]. At a coverage of 1.06 ML the germanene phase can be identified [63]. All the same, its superstructure is debated, which might be described as a $\left(\sqrt{7} \times \sqrt{7}\right)$ [56], a Rec $\left\{c\left(\sqrt{3} \times 7\right)\right\}$ [61, 64], or a (1.35×1.35)R30° [65, 66] with a long-range order of $\left(7\sqrt{7} \times 7\sqrt{7}\right)$ R19.1° [65, 67].

At this point, the question to clear up is which phases are undergone within the structural formation process towards germanene on Ag(111) and how these can be characterized. Based on the characteristics of the phases found, the knowledge gained can be used to prepare germanene phases for further application specifically.
To add clarity on this particular issue, this work presents an experimental study on the structural evolution towards quasi-freestanding germanene formed on Ag(111). Powerful surface analysis tools, such as low-energy electron diffraction (LEED), are used to outline the evolution of different phases of germanium formations with increasing layer thicknesses. The internal and interfacial electronic and chemical structures of clearly distinctive Ge phases were resolved by recording high-resolution photoelectron spectroscopy (XPS) spectra of the Ge $3d$ and Ag $3d$ core levels using synchrotron radiation. In combination with photoelectron diffraction (XPD), structure models will be proposed for structural development throughout the evolution. Moreover, a method is probed to preserve germanene structures from atmospheric contamination by the encapsulation with a capping layer of Al_2O_3.

This thesis is organized into 7 chapters. Chapter 2 introduces 2D materials with particular attention to their electronic properties and the theoretical findings on freestanding germanene. The analysis methods used here are comprehensively presented in chapter 3 and also associated with the experimental setup in chapter 4. A description of the preparation procedure of the investigated samples is provided in chapter 5. All results worked out are discussed in detail in chapter 6. Finally, a summary and outlook of this thesis are given in chapter 7.

Chapter 2

2D Materials

The crystalline structure of a three-dimensional bulk crystal consists of an atomic basis, which is periodically arranged and expanded in all three directions of space, called lattice [68]. However, when concerning only the surface of this crystal, the structure can often be described as a two-dimensional object. The translation symmetry normal to the surface is broken, which often causes a rearrangement of surface atoms, but the chemical bonds to the bulk keep these two-dimensional structures stable. [69, 70] The existence of freestanding two-dimensional (2D) structures and whether these structures are stable or not was controversially discussed in the literature [71–75]. Finally, in 1994 Kyozaburo Takeda and Kenji Shiraishi delivered the theoretical proposal that 2D materials are stable to exist using density-functional theory (DFT)[12]. They carried out first-principle total-energy calculations at the example of C, Si, and Ge arranged in a 2D aromatic stage. They also proposed that carbon atoms preferentially form planar honeycomb structures while Si and Ge assemble in corrugated (buckled) stages [12]. The experimental proof was eventually provided by Konstantin Novoselov and Andre Geim with the experimental synthesis of graphene, as the "father" of all 2D materials, from a graphite crystal [6].
The term 2D materials is commonly referred to as a class of crystalline substances that are stable to exist in two-dimensional sheets expanded only in xy-plane with the thickness of a single atomic monolayer (ML). These called "Xenes" [1] show strong in-plane bonds, but only weak Van der Waals (VdW) interaction in z-direction [76]. These characteristics result from the electronic structure of the respective elements and shall be explained in the following at the example of graphene. The carbon's ground-state electronic configuration shows that only the in-plane orbitals $2s$, $2p_x$, and $2p_y$, which contribute to bonding, but not the out of plane $2p_z$ orbital, are

[1] Named after the common suffix of all termed 2D materials: "X-ene", with X = Si, Ge, Sn, Pb, etc.

occupied by a total of 4 valence electrons. This electronic distribution favors the formation of covalent σ-bonds between carbon atoms by an overlap of sp^2-hybridized orbitals, resulting in a honeycomb structure, as visualized in figure 2.1(a). These strong σ-bonds, as well as the resonance and the delocalization of the sp^2-electrons are mainly responsible for the extraordinary mechanical stability of the carbon hexagons and the outstanding electronic properties of graphene. [77] Stepping down

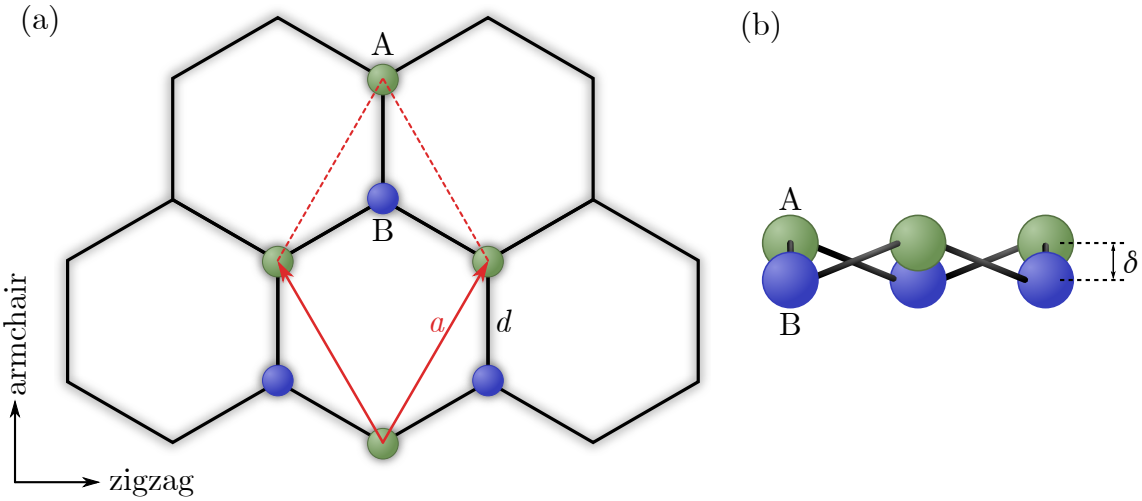

Figure 2.1: (a) Illustration of the general geometry of honeycomb lattices, expanded in zigzag and armchair direction, with the lattice parameter a and the nearest-neighbor distance d. (b) The buckling distance δ is defined as the z-difference between the basis atoms A and B.

group IVA of the periodic table, the so-called carbon group, 2D materials from Si, Ge, *et cetera*, have also initially been predicted to be stable in a honeycomb structure [13]. However, due to the increasing atomic masses of the elements, the inter-atomic distances become larger, which weakens the σ-bonds [78, 79]. An energy-efficient arrangement for this class of materials is a corrugated honeycomb structure. Such a corrugation of the formation, displayed in figure 2.1(b), is called buckling [16, 80]. It enables the additional overlap of the π-bonding $2p_z$-orbitals, leading to a mixed sp^2/sp^3-hybridization, which makes the buckled honeycomb lattice the most stable structure of all elemental materials [81]. The buckling distance δ depends on the material and defines the share of the sp^2/sp^3-hybridization. The kind of hybridization has a direct impact on the electronic properties of the 2D material, which will be discussed later. [16, 80] Besides the buckling parameter, the honeycomb structure can be described by the lattice vector $\vec{a}$, which defines the unit cell of the lattice, as

depicted in figure 2.1(a). The unit cell generally contains a basis of two atoms, A and B, with the nearest-neighbor distance d and the buckling distance δ, as shown in figure 2.1(b). Moreover, the directions within a honeycomb lattice, called armchair and zigzag, are defined with respect to the orientation of the hexagons, as labeled in figure 2.1(a).

After the first experimental synthesis of graphene, a large number of further 2D materials have been investigated. Stand-alone graphene was obtained by exfoliation of a monolayer from a graphite crystal [6] as stacked graphene layers with weak VdW-like interlayer bonds. The same procedure could be applied to MoS_2, hexagonal boron nitride, and black phosphorus. [47] However, not every 2D material is related to a bulk crystal as stacked corresponding Xene layers, which no longer permits the exfoliation method as a universal synthesis procedure. For example, group IVA elemental 2D materials, like silicene (Si), germanene (Ge), stanene (Sn), and plumbene (Pb) have been epitaxially grown on metal substrates by physical vapor deposition (PVD) and segregation [14, 15, 23, 24]. Epitaxial growth on carrier substrates offers the possibility to tune structural parameters, such as the lattice constant or the buckling parameter by the choice of the substrate [46]. Moreover, elemental 2D materials besides group IVA elements have been synthesized, for example, borophene from group IIIA [82], antimonene from group VA [83], tellurene from group VIA [84], and even stable 2D halogens, like iodine and astatine, are already predicted [85]. However, the fabrication of heterostructures as stacked combinations of elemental 2D materials [86, 87] and of functionalized Xenes, namely MXenes [88], emerges to achieve particular material properties.

2.1 Electronic Properties

The popularity of graphene mainly results from its extraordinary mechanical and electronic properties. The latter is going to be the subject of this section.
Novoselov and Geim reported on the synthesis of "the thinnest known material in the universe and the strongest ever measured" [6, 89]. Additionally, charge carriers in graphene reach mobilities of $\mu \approx 10{,}000\,\mathrm{cm}^2/(\mathrm{V\,s})$ and up to $60{,}000\,\mathrm{cm}^2/(\mathrm{V\,s})$ in multilayer graphene [6, 90, 91]. From the remarkably high thermal conductivity in

graphene [92], a similarly high electric conductivity can be estimated [68, 93], which makes it a promising candidate for efficient electronic devices.
The reason for it lies in the electronic band structure of planar honeycomb systems like graphene, whose dispersion relation can be obtained by the tight-binding approach. A detailed discussion on this can be found in numerous publications [7, 77, 94, 95]. The geometry of the honeycomb lattice, which can be considered as two equivalent carbon sublattices A and B, leads to a superimposed band structure of these sublattices. An intersection of the energy bands of two sublattices at the edges of the Brillouin zone (BZ) forms a linear course of the electron dispersion at the K and K' points [9, 95]. Consequently, the electron dispersion in graphene can no longer be described by the parabolic dispersion for electrons with an effective mass m^* in solids as obtained by the Schrödinger equation. However, they can be seen as quasi-particles, called Dirac fermions, obeying the relativistic Dirac equation. Electrons in graphene behave like massless particles with assigned energy of $E(|\vec{k}|) = \hbar v_{\mathrm{F}} |\vec{k}|$ near the Dirac points $E(|\vec{k}|) < 1\,\mathrm{eV}$, traveling with a Fermi velocity v_{F} equal to the speed of light c [9, 10]. Graphene is a zero-gap semiconductor with touching Dirac cones at the K points which gave rise to a new class of materials called Dirac materials. [9, 77, 89, 95] Dirac materials unite silicene, germanene, and stanene since a Dirac-like dispersion was discovered [46, 96]. In addition to high charge carrier mobilities in the corresponding Dirac materials, quantum effects like the quantum Hall effect (QHE) can also occur. For graphene, it was even possible to observe the QHE at room temperature (RT) [97]. Moving to higher-Z materials than graphene, quantum effects like an increasing spin-orbit coupling promoting the behavior as topological insulators [98, 99] and structural properties as the buckling takes effect. The latter is an essential aspect since the buckling of a material directly affects the electronic structure of a material [16]. It was shown that the size of the band gap E_{g} is depending on the buckling height δ [51, 52, 100]. Since a particular buckling for each freestanding 2D material is predicted, epitaxially grown layers feature a buckling distance that varies by the choice of the carrier substrate [16]. Thus, within the preparation process, it is possible to yield a particular size of buckling and band gap, respectively, which can additionally be tuned by functionalization or the application of electric fields [45, 52]. Therefore, the chemical engineering of 2D material-based electronic devices offers massive potential for devices with highly customized electronic properties [8, 101, 102].

2.2 Freestanding germanene

A 2D material is termed freestanding when it is entirely decoupled from other material layers, such as bilayers or a carrier substrate, and independent in its structural and electronic properties [103]. It is desirable to prepare freestanding Xenes to take advantage of their predicted material properties. As mentioned above, only a couple of 2D materials can be obtained from their 3D counterparts, for example, by means of exfoliation. Nevertheless, silicene, germanene, *et cetera* can be grown epitaxially on a carrier substrate in order to subsequently detach the layer and transfer them to an insulating surface [20, 103]. For the detachment, it is helpful to find a weakly interacting sample system, which can be identified from the interface structure and the Xenes' structure parameters. Using DFT calculations, a preferable structural arrangement of freestanding 2D materials can be obtained. Table 2.1 displays the theoretically proposed structure parameters of freestanding germanene in the highlighted row, as well as those of other group IVA Xenes for comparison. The lattice constant a, the nearest neighbor distance d, and the buckling parameter δ are demonstrated in figure 2.1. The distance $l_{\mathrm{ac}}= \sqrt{3}\,a$ means the (2×2)-periodic length as the distance between two atoms of the same sublattice along the armchair direction. Additionally, it can be seen that the values of the band gap energy E_{g}, obtained by DFT and provided in table 2.1, increase with larger buckling and atomic number Z. Here, only the low-buckling distances are shown, although an additional high-buckling phase for many 2D materials is proposed, as it is for germanene $\delta_{\mathrm{hb}} = 2.23\,\text{Å}$ [13].

Table 2.1: Theoretical structure parameters of freestanding 2D materials. a denotes the hexagonal lattice constant, l_{ac} the length of the unit cell along the armchair direction, d the nearest-neighbor distance,δ the buckling height, and E_{g} the bandgap energy.

Xene	a [Å]	l_{ac} [Å]	d [Å]	δ [Å]	E_{g} [meV]	Ref.
C	2.46 – 2.47	4.25 – 4.28	1.41 – 1.42	0	0.001	[16, 104]
Si	3.82 – 3.87	6.62 – 6.70	2.25 – 2.28	0.44	1.5 – 2.0	[13, 104, 105]
Ge	3.97 – 4.06	6.88 – 7.03	2.38	0.64 – 0.71	23.9 – 30.0	[13, 104, 106]
Sn	4.68	8.11	2.83	0.85	100	[107]
Pb	4.93	8.54	3.00	0.71	400	[108, 109]

Chapter 3

Theoretical Background

In this chapter, a brief introduction to the theoretical background underlying the analysis methods performed is given. Firstly, the basic concept of photoemission is introduced in order to present the photoelectron spectroscopy method in chapter 3.1. Subsequently, also diffraction methods are mentioned, such as the photoelectron diffraction and the low-energy electron diffraction in chapters 3.2 and 3.3, respectively.

3.1 X-Ray Photoelectron Spectroscopy (XPS)

Photoelectron spectroscopy (PES) is the most commonly used and most meaningful surface analysis tool for determining the chemical composition, resolving chemical bonding structures, or even enabling conclusions about the electronic and atomic structures of a sample system at the same time. In addition to high energy and spatial resolutions within the measurements, traces of elements down to 0.1 at.% in a sample can be detected [110]. Depending on the photons' energy used to perform PES experiments, different terms for electron spectroscopy are used, as presented in table 3.1. Here, we will focus on x-ray photoelectron spectroscopy (XPS), which is carried out with soft x-ray radiation in this work. The high surface sensitivity and

Table 3.1: Energy ranges of photoelectron spectroscopy types [69, 111].

method	range of photon energy hν	range of wavelength λ
UPS	1 eV – 100 eV	12.40 nm – 1239.85 nm
XPS	100 eV – 2000 eV	0.62 nm – 12.4 nm
HAXPS	2000 eV – 8000 eV	0.15 nm – 0.62 nm

unique ability to resolve bonding structures of buried interlayers and interfaces make XPS the apposite technique for the problem at hand. All types of PES are based on the photoelectric effect, which is illustrated in detail in the following section.

3.1.1 The Photoelectric Effect

In 1839, Alexandre-Edmond Becquerel was able to generate a current between electrodes in an electrolytic solution by the illumination of one electrode with ultraviolet light [112]. This first discovery of the photoelectric effect was further investigated by Heinrich Hertz in 1897, who reported the formation of electric sparks after irradiating a metallic cathode with ultraviolet light [113]. In 1888, Wilhelm Hallwachs observed charging effects of a cathode with a similar experimental setup, supporting these novel findings [114]. Since no explanation of this effect had been published, the direct dependency of the light's frequency ν on the velocity of the emitted electrons was determined by Philipp Lenard in the following years [115].

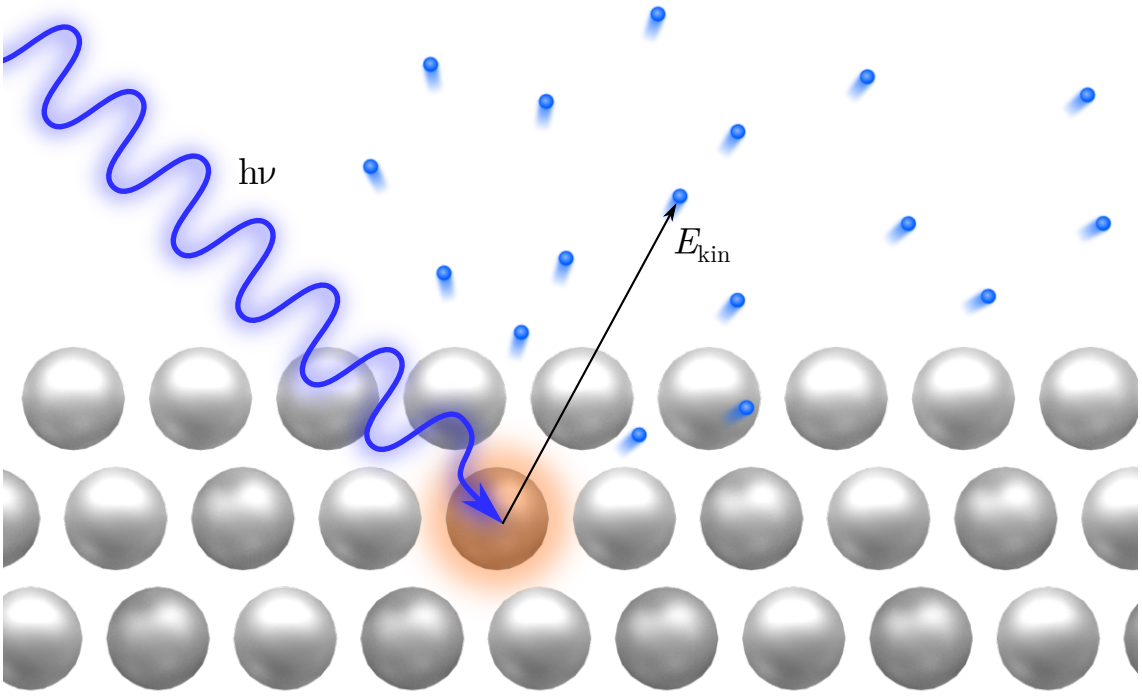

Figure 3.1: Principle illustration of the photoelectric effect. Incoming photons with an energy hν stimulate the emission of photoelectrons with kinetic energies of E_{kin} from the solid into the vacuum.

Only Albert Einstein brought light into the darkness in 1905 with his work on the electrodynamics of moving bodies [116]. He considered light as photon particles with assigned energy of $E_{\text{photon}} = \text{h}\nu$, which are able to induce the emission of electrons from a solid by fully transferring its energy to the electrons, as visualized in figure3.1. With the progress in providing sufficient monochromatic light, the Einstein equation [116],

$$E_{\text{kin}} = \text{h}\nu - E_{\text{bin}} - \Phi \tag{3.1}$$

was additionally confirmed by Robert A. Millikan in 1916, including a precise determination of the Planck constant h [117]. Equation (3.1) returns the kinetic energy E_{kin} of an emitted photoelectron after the illumination of a solid with electromagnetic radiation hν. The electrons are bound with a binding energy of E_{bin} in the solid that features a work function of $\Phi = E_{\text{vac}} - E_{\text{F}}$ determined by the vacuum level E_{vac} and the Fermi energy E_{F}. In the following years, the photoemission process generated the awareness of obtaining binding energies of core levels in a sample system. By using sufficiently high excitation energy, electron spectroscopy for chemical analysis (ESCA), formally known as x-ray photoelectron spectroscopy (XPS), was launched. [111, 118]

The interaction of radiation with matter is generally a sophisticated topic. However, interaction processes, such as the Compton effect and pair production, can be neglected due to the substantial energy dependency of the corresponding cross-sections. For excitation energies of $\text{h}\nu \leq 1000\,\text{eV}$, the photoelectric effect is the dominating absorption process for the matter of all elements [119]. Figure 3.2(a) illustrates the principle of photoemission with x-ray radiation. The photoemission process can be divided into three steps in a model concept. After the photoexcitation of core level and valence band (VB) electrons with radiation of a photon energy hν as a first step, the emitted photoelectrons propagate subsequently through the solid in a second step. Electrons with binding energies of $E_{\text{bin}} < \text{h}\nu - \Phi$ can finally escape from the sample into the vacuum as a third step. This useful three-step model serves as a comprehensive approximation of the photoemission process as long as it is sufficiently applicable [118, 120]. For a more accurate description, the three-step model must be divided into single one-step models, which treat all steps as individual quantum mechanical processes [121–123]. The kinetic energy of the photoemitted electrons reveals a spectral distribution, as exemplarily displayed at the top of

figure 3.2(a), while some of the signals can be attributed to the binding energies E_{bin} via equation (3.1). The binding energy is commonly referred to as the Fermi energy E_{F} and individually depends on the element, the orbital, and the chemical environment of the corresponding atom. Next to elastic lines of core level photoelectrons, features of secondary electrons at low kinetic energies and a continuous inelastic background

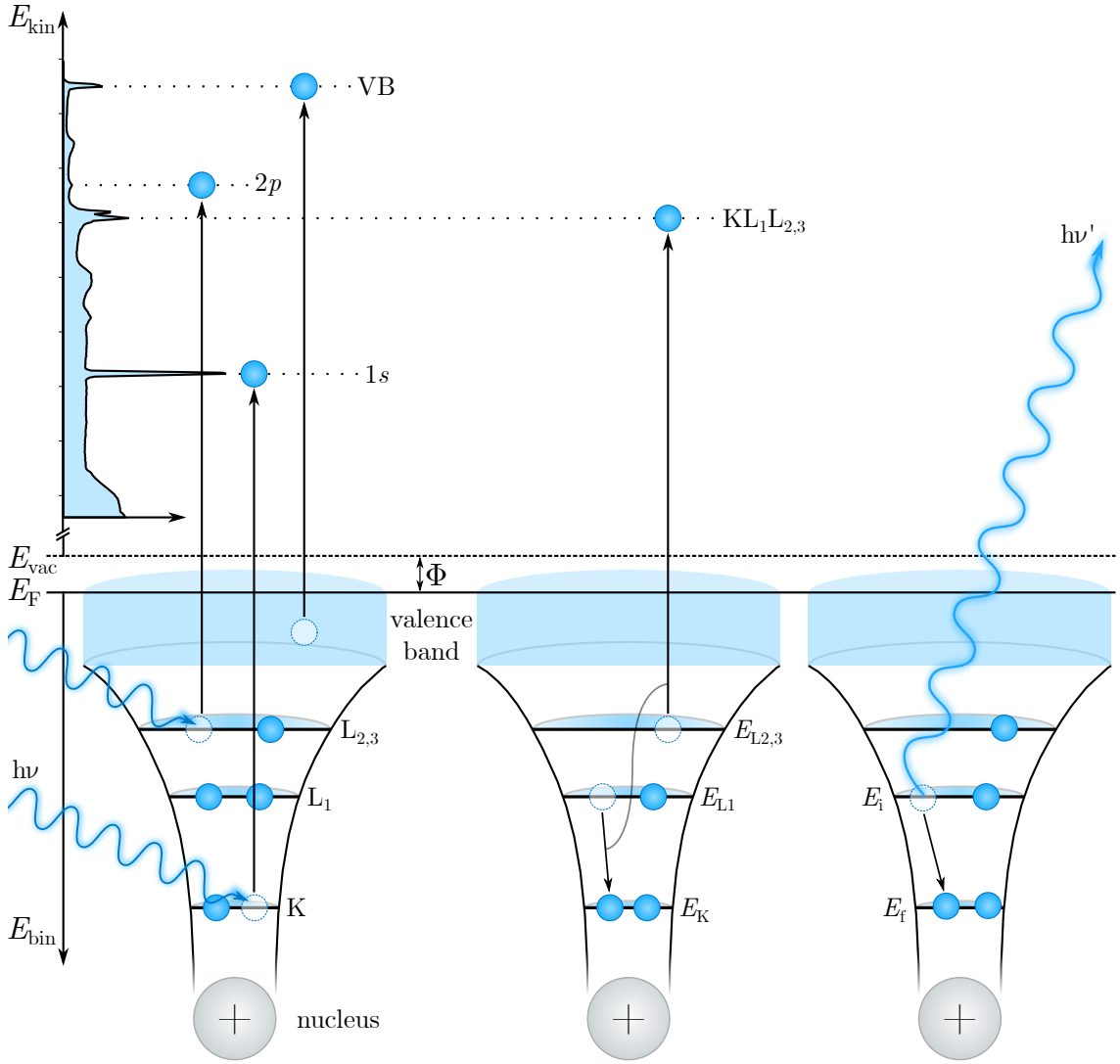

(a) Photoemission (b) Auger process (c) Fluorescence

Figure 3.2: The principle of photoemission as (a) the excitation of core level and VB electrons with radiation hν and the subsequent relaxation processes of (b) the Auger-Meinter effect, and (c) the fluorescence. Photoelectrons and Auger electrons are detected and typically plotted against their kinetic energy E_{kin}, as depicted at the top of (a).

contributes to the spectrum [111]. Moreover, signals of Auger electrons appear, which are part of the relaxation from the photoexcitation. Photoemitted electrons leave unoccupied hole-states with lifetimes of typically $\tau \approx 1\,\mathrm{fs}$ [124], which are filled by core level electrons with lower binding energies. The energy difference between the excited initial state with energy E_i and the relaxed final state E_f is released by the Auger-Meitner effect [125, 126] and fluorescence [127, 128]. The probability which of these processes dominates depends on the excitation energy $\mathrm{h}\nu$ and the atomic number Z of the investigated elements [69, 111]. Since the fluorescence process is dominant for elements with $Z \gtrapprox 30$, the Auger-Meitner effect occurs for relatively light elements with $Z \lessapprox 30$ [129]. The relaxation effects are depicted in figure 3.2(b) and (c). In the case of fluorescence, the energy difference is released by the emission of photons with the energy of

$$\mathrm{h}\nu' = E_\mathrm{f} - E_\mathrm{i}\ . \tag{3.2}$$

Within the Auger process, which is shown in figure 3.2(b), the energy difference of the relaxation is transferred to a weaker bonded electron, which is emitted from the solid as an Auger electron. The electron will be detected in the XPS spectrum with kinetic energy as

$$E_\mathrm{kin}([\mathrm{Auger}]) = E_\mathrm{f} - E_\mathrm{i} - E_\mathrm{Auger}\ . \tag{3.3}$$

In the example visualized in figure 3.2(b), this means

$$E_\mathrm{kin}(\mathrm{KL_1L_{2,3}}) = E_\mathrm{K} - E_\mathrm{L1} - E_\mathrm{L2,3}\ .$$

As illustrated in figure 3.2(b) and equation (3.3), only binding energies of initial and final states contribute to the kinetic energy, so it is entirely independent of the irradiating photon energy $\mathrm{h}\nu$. For this reason, features of Auger electron can be identified in the XPS spectrum when its kinetic energies remain constant while the excitation energy is varied.

3.1.2 Photoionization Cross-section

The intensity of the detected electrons from different elements and core levels in the vacuum is not necessarily proportional to the occupation number of the corresponding

orbitals, but it is related to the photoelectric cross-section $\sigma_{\mathrm{i}\to\mathrm{f}}$ for a transition from an initial state $|\Psi_\mathrm{i}\rangle$ to a final state $|\Psi_\mathrm{f}\rangle$. The intensity $I(E_\mathrm{F})$ of core level peak, which is detected at a kinetic energy $E_\mathrm{kin} = E_\mathrm{F} - \Phi$ depends on,

$$I(E_\mathrm{F}) \propto n\,\sigma_{\mathrm{i}\to\mathrm{f}}\,\lambda\,A\,J_{\mathrm{h}\nu}\ , \tag{3.4}$$

with the number of atoms per volume n, the inelastic mean free path (IMFP, see section 3.1.3) λ, the illuminated area A on the sample, and the photon flux $J_{\mathrm{h}\nu}$ at an energy $\mathrm{h}\nu$ [1] [69, 111]. The transition probability $\omega_{\mathrm{i}\to\mathrm{f}}$ per unit time of a solid, as a many-electron system, can be calculated by applying the time-dependent perturbation theory for a harmonic perturbation which results in Fermi's golden rule,

$$\omega_{\mathrm{i}\to\mathrm{f}} \propto \frac{2\pi}{\hbar}\left|\langle\Psi_\mathrm{f}|\,\Delta\,|\Psi_\mathrm{i}\rangle\right|^2\,\delta(E_\mathrm{f} - E_\mathrm{i} - \mathrm{h}\nu)\ . \tag{3.5}$$

Here $|\Psi_\mathrm{i}\rangle$ is the initial state of the solid with the energy E_i, which is usually close to the ground state, and $|\Psi_\mathrm{f}\rangle$ is the excited state with the energy E_f which consists of the electron-hole state of the solid and the free-electron state in the vacuum [111]. The perturbation operator in equation (3.5) represents the general interaction-Hamiltonian between radiation and matter and can be written as

$$\Delta = \sum_{i=1}^{N}\frac{1}{2m}\left(\vec{p}_i - \frac{e}{c}\vec{A}(\vec{r}_i,\,t)\right)^2\ . \tag{3.6}$$

The sum in equation (3.6) includes N electrons, with momentum $\vec{p}_i$ and location $\vec{r}_i$, which are influenced by the vector potential $\vec{A}(\vec{r},\,t)$. Assuming weak fields of radiation with wavelengths λ, which are large compared to atomic distances (see table 3.1), the interaction parameter (3.6) can be reduced to $\Delta \propto \vec{A(t)}\cdot\vec{p}_j$. [118] Turning to the one-electron picture, the matrix element $\langle\Psi_\mathrm{f}|\,\Delta\,|\Psi_\mathrm{i}\rangle$ in equation (3.5) can be divided into the transition probability of a single electron j with the energy ϵ_j to a final state $|\phi_\mathrm{f}(\epsilon_\mathrm{f},\vec{k})\rangle$ with the energy ϵ_f and the momentum $\vec{k}$. If many-body interactions are neglectable, the vector potential can be assumed to be time-independent by applying the dipole approximation. With the use of commutation relations, the

[1] For the measured intensity, the acceptance angle of the electron analyzer Θ_HEA, as well as the differential cross-section $\left(\frac{\mathrm{d}\sigma}{\mathrm{d}\Omega}\right)_{(\Theta,\phi)}$ have to be taken into account.

dipole matrix element of photoemitted, localized core level electrons can be expressed as [111, 118]

$$m_{j,\mathrm{f}} \propto \langle \phi_{\mathrm{f}}(\epsilon_{\mathrm{f}}, \vec{k})|\ \vec{A}_0 \cdot \vec{r}_j\ |\phi_j(\epsilon_j)\rangle\ \delta(\epsilon_{\mathrm{f}} - \epsilon_j - \mathrm{h}\nu)\ . \tag{3.7}$$

Figure 3.3 shows the cross-sections of particular subshells for silver and germanium depending on the exciting photon energy hν, obtained by calculations of the Hartree-Fock-Slater one-electron central potential model, also known as the dipole approximation mentioned above [130]. All the displayed curves have a similar shape. After a steep rise of the curve from the ionization energy of the corresponding atomic orbital, a monotonous falloff of the cross-section towards higher energies can be observed. The reason for this lies in the spatial shapes of the electrons' wave function: the maximum cross-section is expected when the photoelectrons' wavelength is of a similar size to the spatial amplitude of the localized core level electrons' wave function [111].

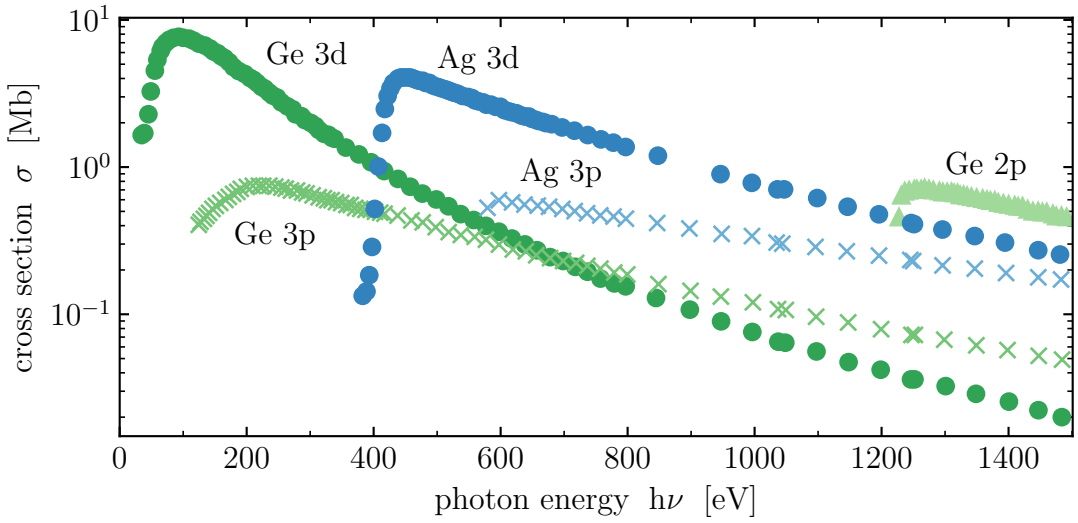

Figure 3.3: Calculated cross-sections in dipole approximation of selected elemental subshells of silver and germanium, in dependency of the excitation energy hν. The figure was reproduced with the data from [130].

3.1.3 Inelastic Mean Free Path (IMFP)

It was already mentioned in equation (3.4) that the yielded intensity of photoelectrons depends on the inelastic mean free path λ (IMFP). Due to inelastic scattering processes during the core level electrons' propagation through the solid, their kinetic energy is reduced so the total number of photoemitted electrons is attenuated. Its initial intensity I_0 decays exponentially with the traveling path d inside the solid,

$$I(\lambda) = I_0 \, \exp\left(-\frac{d}{\lambda(E)}\right) , \tag{3.8}$$

where $\lambda(E)$ denotes the energy-dependent IMFP. The energy dependency originates from the interaction probability of electrons with the matter in terms of mainly electron-electron interaction and electron-phonon interaction [131]. A measure characterizing the energy loss of electrons with kinetic energies E_{kin} is the inelastic mean free path, which describes the distance λ an electron travels on average in a solid before it is attenuated to 1/e of its initial intensity I_0. It was found that the course of the IMFP as a function of the kinetic energy of the electrons is roughly independent of the corresponding material and can be described by a universal curve. The universal curve was determined as a fit of experimentally obtained data of various materials, approximately following the relation [132],

$$\lambda_{\mathrm{uc}}(E) = \frac{538\,a}{E^2} + 0.41\sqrt{a^3\,E} \quad [\mathrm{nm}] , \tag{3.9}$$

with the thickness of a monolayer a,

$$a^3 = \frac{A}{\rho\, n\, N_{\mathrm{A}}} \, [\mathrm{nm}] . \tag{3.10}$$

Here, A is the atomic or molecular weight, n is the number of atoms in the molecule, and N_{A} is the Avogadro constant [132]. The universal curve and the data set of measured IMFP of different materials are displayed in figure 3.4. The material independency of the universal curve can be explained through the kinetic energy range of interest, where electrons in the solid can approximately be treated as a free-electron gas. In this case, the energy loss function is mainly determined by the plasma frequency, roughly equal for all materials [118, 131]. The minimum of

the universal curve with $\lambda_{\mathrm{uc,min}} = 0.4\,\mathrm{nm}$ can be achieved for a kinetic energy of $E_{\mathrm{kin}} \approx 40\,\mathrm{eV}$.

A more accurate description for the IMFP, especially for kinetic energies of $E_{\mathrm{kin}} > 50\,\mathrm{eV}$ was established by the *TPP-2M*-formula [133]:

$$\lambda_{TPP-2M} = \frac{E_{\mathrm{kin}}}{{E_{\mathrm{p}}}^2 \left[\beta \ln\left(\gamma E_{\mathrm{kin}}\right) - \left(C/E_{\mathrm{kin}}\right) + \left(D/{E_{\mathrm{kin}}}^2\right)\right]} \tag{3.11}$$

However, the empirical values of β, γ, C, and D, as well as the plasmon energy of the free electron gas E_{p} are element specific. The obtained data of the *TPP-2M*-formula for the elements germanium and silver using the Penn algorithm are illustrated in figure 3.4 [133].
Thus, the surface sensitivity of electron spectroscopy and diffraction experiments

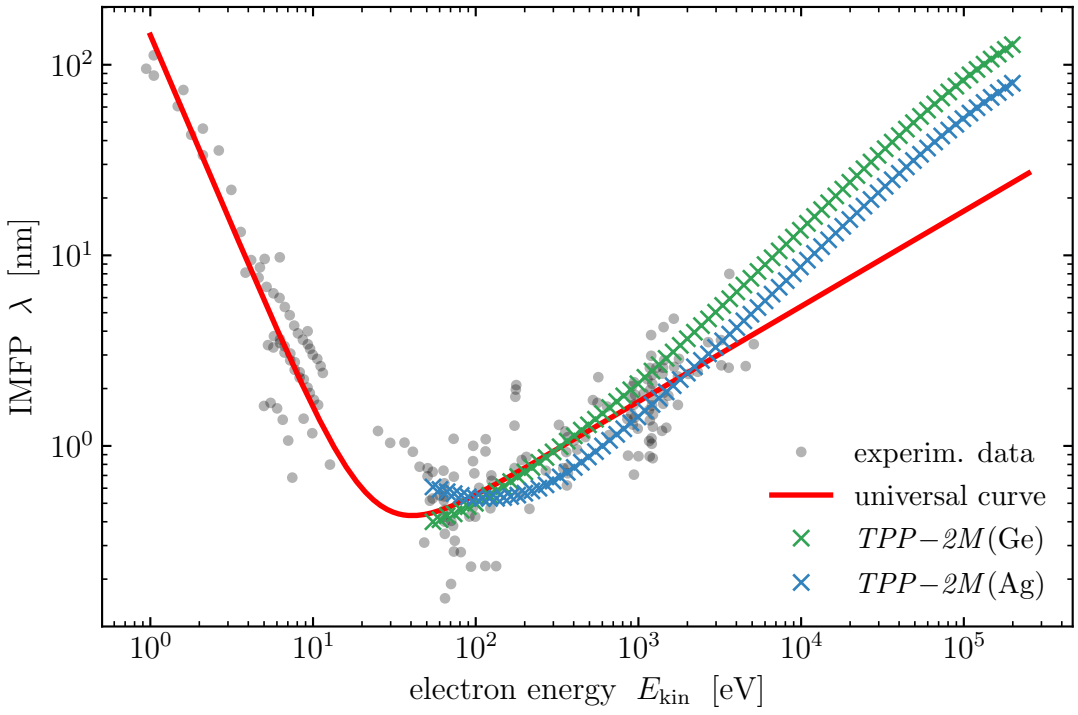

Figure 3.4: The universal curve (solid red line) as a fit of experimental data (grey dots) follows the form of $\lambda_{\mathrm{uc}}(E) = 143 \cdot E^{-2} + 0.054\sqrt{E}$ [132]. Computationally obtained data of the IMFP after the *TPP-2M*-formula for germanium (green) and silver (blue) show deviations from the universal curve. All data are taken from [132, 133].

can be tuned by choice of suitable kinetic energy. According to equation(3.8), on average 63 % of the total photoexcited electrons are inelastically scattered after a propagation path of $d = 1\,\lambda$, so that mainly electrons originating from upper surface layers of $d < \lambda$ are detected.

3.1.4 Angle-Resolved Photoelectron Spectroscopy (ARPES)

One way to gain additional structural information about a sample system via XPS measurements is to consider the angular effects of PES by performing angle-resolved photoelectron spectroscopy (ARPES).
Basically, ARPES means the aquisition of PES spectra at different emission angles Θ or orientation angles Φ. The most common use for ARPES is the angle-resolved UPS,

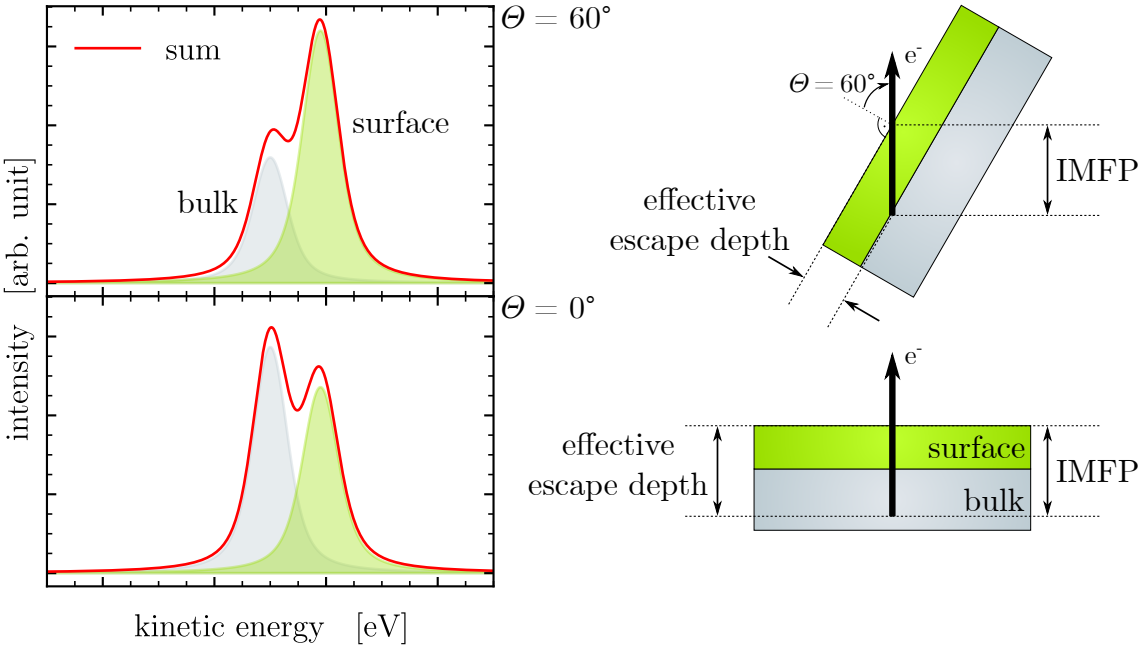

Figure 3.5: Principle of angle-resolved XPS measurements by taking advantage of the effective escape depth. Spectra recorded under high polar angles Θ (top) are more sensitive to surface components than normal emission-XPS spectra (bottom), as indicated by the bulk and surface component share.

as an analysis tool for the electronic structure of a material to resolve the energy dispersion of the VB in k-space. Also, XPD belongs to photoemission experiments with an angular resolution, which focuses on the structural examination of a sample.

The principle procedure for ARPES measurements, as performed in this work, so-called angle-resolved XPS (ARXPS), is to record XPS high-resolution and survey spectra at different polar angles Θ. The polar angle Θ is defined as the angle between the surface normal of the sample and the analyzer axis, which can be varied by rotating the sample, as visualized in figure 3.5. The effect of this method is also demonstrated in figure 3.5 using a fictional example of a layered system: while the IMFP is constant for a measured photoelectron peak at kinetic energy E_{kin}, the effective escape depth (EED)[2] of photoelectrons can be reduced by varying the emission angle Θ [135]. As is exemplified in figure 3.5, the EED can be reduced by a factor of 2 when changing the angle Θ and rotating the sample, respectively, from $\mathrm{EED}(0°) = \lambda$ to $\mathrm{EED}(60°) = \lambda \cdot \cos(60°)$. It results in a varying intensity ratio of bulk and surface components within an XPS signal of a sample system, as indicated by figure 3.5. Consequently, the decreased probing depth EED for high emission angles Θ leads to an increased surface sensitivity. Thus, this method allows the assignment of particular components originating from different chemical environments to the surface, the interface, or the bulk of a sample system. [111, 136, 137]

3.1.5 XPS-Data analysis

In order to extract information from XPS data about the chemical composition and bonding structure of a sample system, a quantitative analysis is necessary. XPS survey spectra are created by scanning a wide energy range for the purpose of determining the chemical constitution of a sample system. As shown in figure 3.2, characteristic elastic line features of photoelectrons and Auger electrons are identified in the spectrum and assigned to the corresponding elements with the help of databases such as NIST [138]. Using equation (3.4), the elemental concentration within a sample system indicated by its respective intensity $I(E_{\mathrm{F}})$ can be determined with a few percent precision and even more precise for relative compositions [111]. Moreover, angle-resolved or energy-resolved XPS survey measurements can be used to estimate the film thicknesses of layered sample systems [111, 136, 137, 139].
XPS spectra with a high energy resolution (HighRes) are used for investigations

[2] This work is confined to only qualitative conclusions drawn from ARXPS measurements. Anyhow, it must be avoided to confuse the EED used here with terms such as the mean escape depth (MED) or the information depth (ID) [134].

of the chemical binding structure of a sample. By involving angular resolution in HighRes measurements, even findings about the atomic structure can be obtained [111]. In this section, effects contributing to the shaping of XPS peaks are introduced before discussing the line shape and processing of HighRes spectra.

Spin-Orbit Coupling

An artificially created XPS HighRes spectrum of a $3d$ core level is displayed in figure 3.6. Since the peak shape and background are discussed in the following section, especially the multiplet splitting of the signal stands out, which means the split-up of the displayed peak into a doublet signal. Bound electrons are allocated to different quantum states, which can be characterized by the quantum numbers n, l, and s. These quantum numbers correspond to the eigenvalues of their respective operators commutating with the Hamiltonian. The principle quantum number n denotes the main energy level, which splits off into atomic orbitals with orbital angular

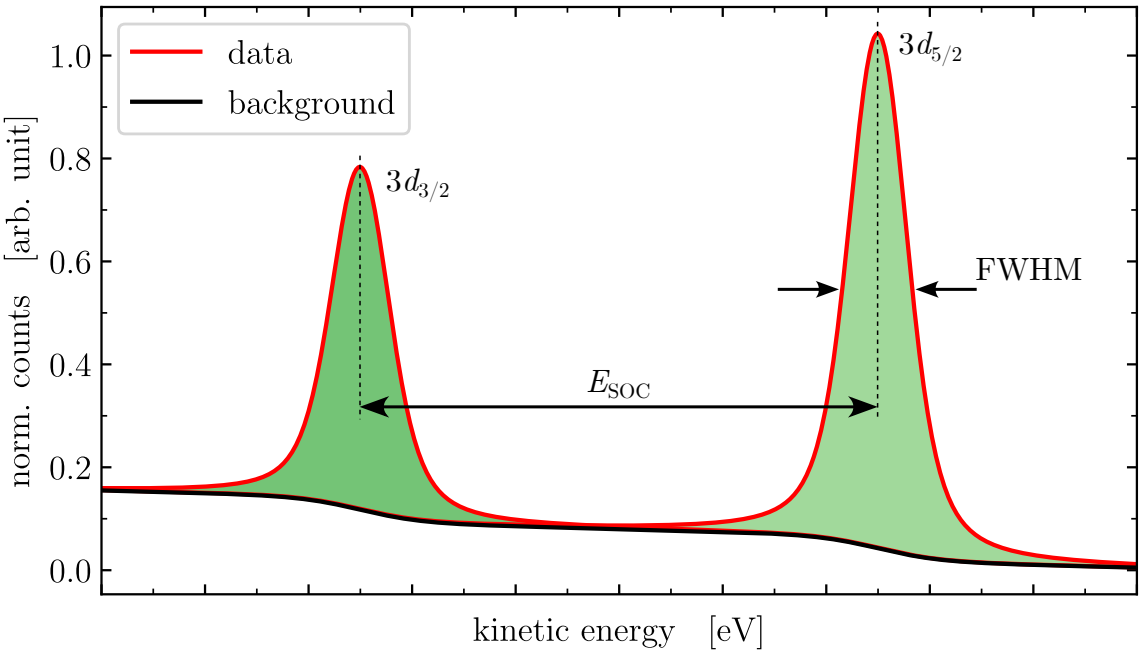

Figure 3.6: Typical HighRes XPS spectrum of a fictive $3d$ core level, consisting of a Shirley background (solid black line) and two spin-orbit split components $3d_{3/2}$ (dark green) and $3d_{5/2}$ (light green). The components, each of which has a full width half maximum FWHM, are separated by a spin-orbit separation of E_{SOC}.

momentum numbers l, also known as so-called subshells, occupied by electrons with a spin s. Due to the interaction of the induced magnetic dipole of the electron and its orbital motion in the field of the atomic nucleus, the spin-orbit coupling (SOC), a total angular momentum number j for electron states with $l > 0$ has to be defined as

$$j = l + s \ , \tag{3.12}$$

to retain the conserved quantities. In equation (3.12), the spin quantum number can be either $s_\uparrow = +\frac{1}{2}$ or $s_\downarrow = -\frac{1}{2}$ for parallel and anti-parallel electron spins, respectively. The multiplets are $(2j + 1)$-degenerated, which results in the fine structure for a solid containing slightly different energy levels E_j. [136, 140] The difference E_{SOC} between these energy levels is the spin-orbit separation, which can be observed in XPS spectra of atomic orbitals with $l > 0$. Its magnitude mainly increases with the atomic number Z of an element [140],

$$E_{\mathrm{SOC}} \propto \frac{Z^4}{n^3\, l(l+1)} \ . \tag{3.13}$$

Due to the degeneracy of the multiplet splitting, also the intensity, defined as the integrated counts and the peak area, respectively, of the spin-orbit split peak can be determined as a ratio of,

$$\frac{I_{j<l}}{I_{j>l}} = \frac{2(l+s)+1}{2(l-s)+1} \ . \tag{3.14}$$

Using the quantum number l, formerly denoted as *s*-, *p*-, *d*-, *f*-, and *g*-orbital for $l = 0$, 1, 2, 3, 4, respectively, the area ratio for the displayed *d* core level in figure 3.6 is $I_{3/2}/I_{5/2} = 2/3$.

Chemical Shift

The most fundamental achievement for analyzing the chemical bond structure of a sample system using XPS was discovered by Kai Siegbahn, who was also awarded the Nobel prize for this in 1981 [141]. Chemical shifts of core level signals mean a shift in binding energies of the same signal, which are caused by different electronic surroundings of the atoms, either in the initial or the final state [142]. The most famous example of initial state chemical shifts is the C 1*s* core level of an ethyl

trifluoroacetate molecule, which is displayed in figure 3.7 [143, 144]. Prior to the photoemission, all contributing carbon atoms within the molecule are placed in different chemical environments regarding its binding partners. As a result of the difference in electronegativity, the valence electrons involved in the bond are displaced towards the atoms with higher electronegativity. This leads to changes in the effective

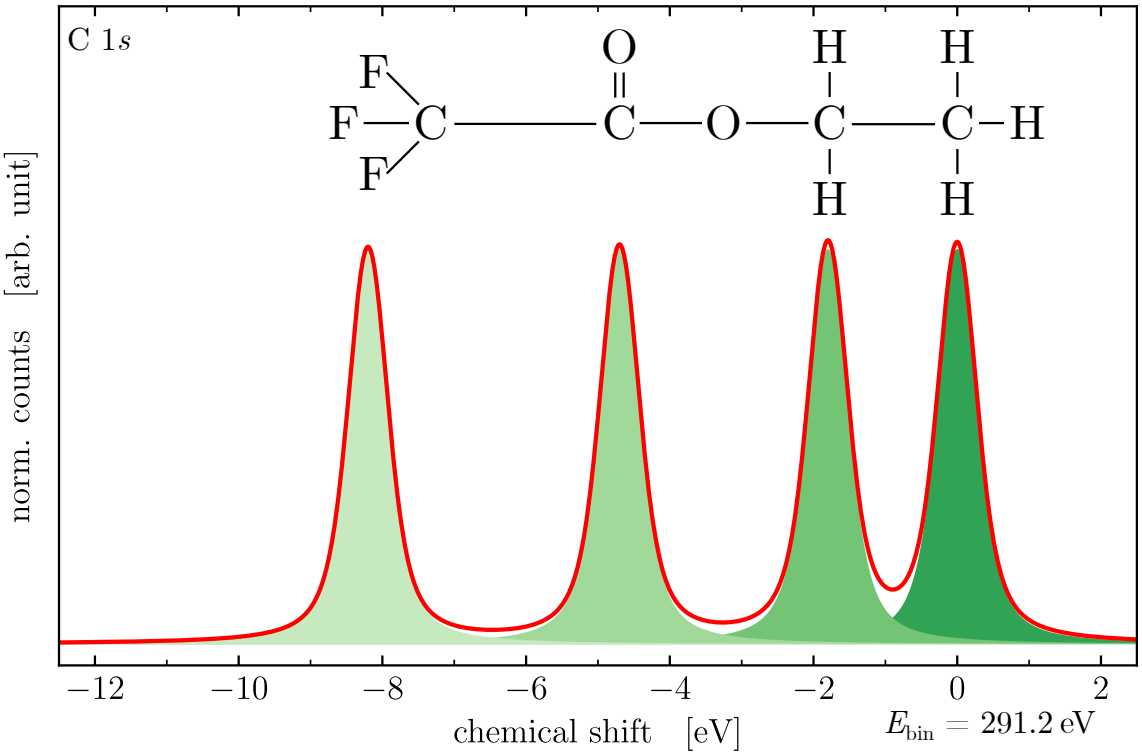

Figure 3.7: The C 1s core level of the ethyl trifluoroacetate molecule illustrates the chemical shifts E_{chem} of carbon atoms in different chemical environments. Reproduced from [143, 144].

charge potential of the respective atom nuclei, which affect small changes in binding energies E_{chem} [118, 145]. In the case of $C_4H_5F_3O_2$ in figure 3.7, the CF_3 component is shifted by $E_{chem} = 8.1\,eV$ regarding the CH_3 component at a binding energy of $E_{bin} = 291.2\,eV$ [144] because of its bond to fluorine, which has the highest electronegativity of all elements [146]. Using this method, the chemical environment of identified components in a HighRes spectrum can be analyzed. A special case of initial state chemical shifts is the surface core level shift, which is affected by the differing atomic coordination according to the symmetry break of the bulk structure at the surface [111, 147]. Final state chemical shifts arise from screening

effects, prevalently induced by charge transfer from the bulk to the surface and the interaction with photo-holes [118, 145].

Background and Peak shape

Within step two of the three-step model of photoemission, for example, during the propagation of the photoexcited electrons through the solid, the electrons are inelastically scattered at bulk atoms. These processes lead to kinetic energy losses and the creation of secondary electrons. The secondary electrons can be observed as a continuous background (BG) in the XPS spectra, which increases for lower kinetic energies. Energy loss features, such as plasmon excitation, are discrete background signals that background profiles can model, but commonly, they are treated as fittable components to separate them from the spectra. In order to derive quantitative conclusions from XPS measurements, a subtraction of the background is commonly performed. [111, 118, 120, 136]
The first approach to model background of a HighRes XPS spectrum is to apply a Shirley background profile to the data $S(E)$, which follows the form of [148, 149],

$$B_{\mathrm{S}}(E, e) = e \int_{E}^{E_2} S(E')\,\mathrm{d}E' \ , \quad e \geq 0. \tag{3.15}$$

This deterministic background profile is based on a uniform energy loss function and, thus, does not account for an asymmetric line shape [142, 149]. Therefore, the background profile, as introduced by Sven Tougaard [149, 150],

$$B_{\mathrm{T}}(E, B, C, C', D, T_0) = \lambda(E) \int_{E}^{\infty} K(E, T) M^*(E')\,\mathrm{d}E' \ , \tag{3.16}$$

combined with a polynomial background $B_{\mathrm{P}}(E)$ [151] in $M^*(E) = M(E) - B_{\mathrm{P}}(E)$, is more suitable. In this case, the energy loss $T = E' - E$ is considered under the probability $K(E, T)$ that an electron of energy E loses energy T per unit energy loss and per unit path length traveled in the solid. Since the energy loss function can only be measured by electron energy loss spectroscopy (EELS) for any material

[131], here, the product of probability $K(E,T)$ and the IMFP $\lambda(E)$ is fitted by the parameters B, C, C', and D in terms of the 5-PIESCS approximation [151],

$$\lambda(E)\cdot K(E,T) = \Theta(T-T_0)\frac{B(T-T_0)}{\left(C+C'(T-T_0)^2\right)^2 + D(T-T_0)^2}\,, \tag{3.17}$$

with the gap energy T_0. The application of a Tougaard background requires an energy range of at least 50 eV [151]. However, the background is described in a physically more meaningful way as it considers the energy loss and provides better results compared to a Shirley background [149].

Signals of photoelectrons originating from discrete core levels with defined binding energies E_{bin} are ideally assumed to be shaped as a delta distribution $I\cdot\delta(E_{\mathrm{bin}})$. In reality, physical and instrumental influences cause a broadening of the elastic lines in a measured XPS spectrum [111, 118]. Due to the lifetime of the photoinduced core-hole states, a Lorentzian $L(E)$ distribution of the core level signal is generated, which can be written as

$$L(E) = \left\{1+\left[\frac{(E-E_0)}{\beta_{\mathrm{L}}}\right]^2\right\}^{-1}\,. \tag{3.18}$$

An example of a Lorentzian distribution is plotted in figure 3.8(a), shaped as the dashed green line curve. Taking the instrumental effects, such as the analyzer transmission, energy width of excitation radiation, electron-phonon interaction, and temperature broadening, into account, also a Gaussian blur $G(E)$ of the signal needs to be applied [118, 136, 152–154]:

$$G(E) = \exp\left\{-\ln 2\left[\frac{(E-E_0)}{\beta_{\mathrm{G}}}\right]^2\right\}\,. \tag{3.19}$$

The profile of a Gaussian is also visualized in figure 3.8(a) by the dashed blue line. Furthermore, a structural disorder of the sample can lead to an additional Gaussian broadening of the peak [155, 156]. The FWHM of each profile in (3.18) and (3.19) is

defined as $\mathrm{FWHM}_i = 2 \cdot \beta_i$. Finally, the core level peak can be modeled by a Voigt profile [157] as a convolution of the Lorentzian and Gaussian:

$$V(E) = (L * G)(E) = \int_{-\infty}^{\infty} L(E')G(E - E')\,\mathrm{d}E' \ . \tag{3.20}$$

Figure 3.8(a) shows an example of a Voigt profile V compared to its deconvoluted Gaussian G and Lorentzian L. Moreover, approximated Voigt profiles, so-called

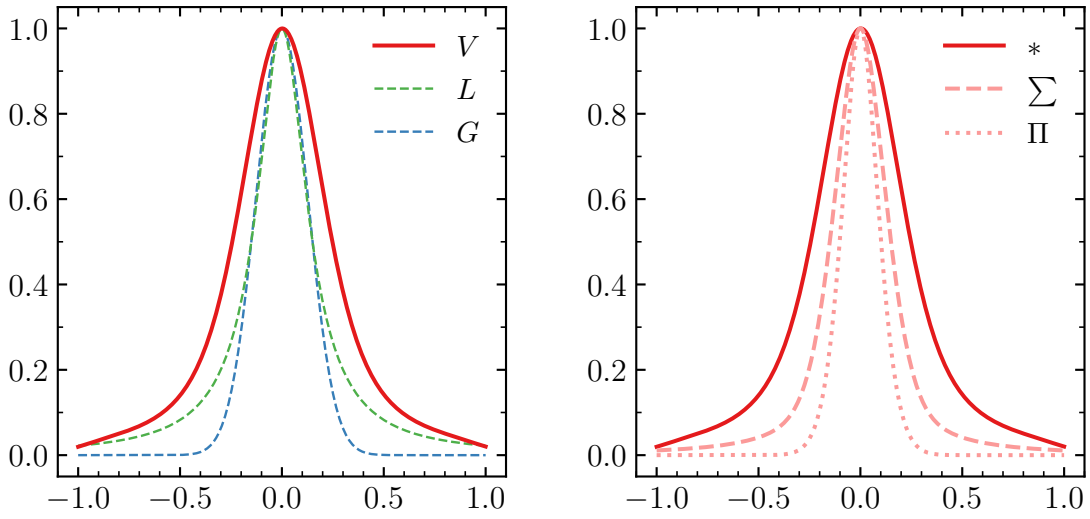

(a) Convoluted Voigt profile.

(b) Voigt and Pseudo-Voigt.

Figure 3.8: (a) Visualization of a Voigt profile V as the convolution of a Lorentzian L and a Gaussian G. (b) Due to computational resources, some Voigt profiles ($*$) are approximated by Pseudo-Voigt profiles as a sum ($\sum$) or a product ($\prod$) of a Gaussian and a Lorentzian.

Pseudo-Voigt functions, as the sum or product of a Gaussian and Lorentzian are commonly used for XPS data fitting to simplify the analysis [152]. Figure 3.8(b) illustrates the difference between convoluted ($*$), summed ($\sum$), and multiplied ($\prod$) profiles of a Gaussian and a Lorentzian since the convolution of both profiles is physically the most accurate and adequate model [153]. However, a Voigt profile is not universal for all materials because metallic samples often show an intrinsic asymmetry of their peak shape, tailing towards lower kinetic energies [142, 158]. Thus, an asymmetric Pseudo-Voigt profile [152, 153] or a profile, as introduced by

Sebastian Doniach and Marijan Šunjić [159] with an asymmetry parameter α and a FWHM β_{DS}, should be used:

$$DS(E) = \frac{\cos\left\{\frac{\pi\,\alpha}{2} + (1-\alpha)\tan^{-1}\left[\frac{(E-E_0)}{\beta_{\mathrm{DS}}}\right]\right\}}{\left[(E-E_0)^2 + {\beta_{\mathrm{DS}}}^2\right]^{\frac{1-\alpha}{2}}} \,. \tag{3.21}$$

In contrast to non-metals, metals typically have a higher density of occupied and unoccupied states below and above the Fermi level E_{F}, respectively, which causes the interaction of photoelectrons and holes, often described as electron-hole pairs [160]. The asymmetry of the respective core level peak then results from the continuous energy loss. Figure 3.9 visualizes equation (3.21) for different asymmetry parameters α while the profile converges towards a Lorentzian for $\alpha = 0$. The profile applied to the asymmetric peaks is a convolution of a Gaussian and a Doniac-Sunjic profile (DS)[3], whose asymmetry parameter depends on the probed material [158].

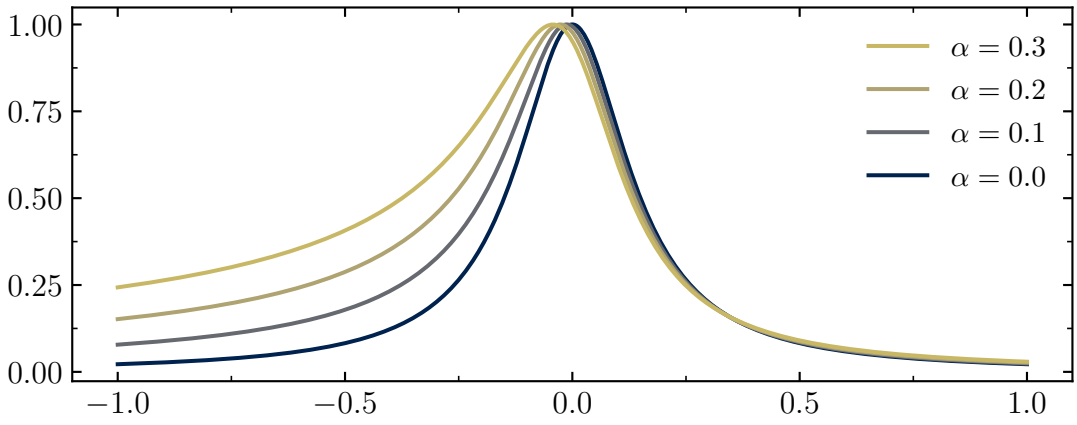

Figure 3.9: Illustration of a convoluted profile of a Gaussian and a Doniach-Sunjic function with different asymmetry parameters α. The DS profile for $\alpha = 0$ conforms a Voigt profile at the same time.

Fitting of XPS-Data

All HighRes XPS spectra were fitted using the program *UNIFIT 2022* [139]. Since no conclusions are drawn from the absolute number of counts, all spectra are normalized

[3] In the following, the convolution of Doniac-Sunjic and Gaussian is denoted as DS profile.

to their maximum. Although it is likely in comparative literature to present XPS spectra in dependency of binding energies E_{bin} instead of the directly measured kinetic energies E_{kin}, the challenges of referencing correct binding energies, such as adjusting reproducible contact potentials of sample and analyzer or obtaining reliable reference data, often are neglected [161, 162]. As long as no referencing via the measured Fermi energy E_{F} is possible, in this work, XPS spectra are presented in dependency of their kinetic energy [136]. After applying a background and an adequate number of profiles in the correct shape, the fit, as the sum curve of all components applied, can be evaluated concerning the measured data using ${\chi^2}^*$, the residual, and the Abbe criterion [163, 164]. To get an idea of the fit quality in dependency of the degrees of freedom $(N - P)$, the reduced chi-square can be used as,

$$ {\chi^2}^*(\vec{p}) = \frac{1}{N-P} \sum_{i=1}^{N} \frac{\left[M(i) - S(i,\vec{p})\right]^2}{M(i)} \,, \tag{3.22} $$

with the measured spectrum $M(i)$ of N data points and fitted spectrum $S(i,\vec{p})$ with a vector of fit parameters $\vec{p}$ containing P independent fit parameters. A value of ${\chi^2}^* = 1$ is expected for a perfect fit, while values of ${\chi^2}^* > 1$ and ${\chi^2}^* < 1$ indicate a "bad" fit and a overfit, respectively [165]. A visualization of the derivation between fitted and measured data can be provided by the normalized residual,

$$ \mathrm{Res}(i) = \frac{S(i,\vec{p}) - M(i)}{\sqrt{M(i)}} \,. \tag{3.23} $$

Using the unnormalized residual $\mathrm{Res}'(i) = S(i,\vec{p}) - M(i)$, the Abbe criterion as a further quality mark of the fit can be defined as,

$$ \mathrm{Abbe} = \frac{1}{2} \frac{\sum_{i=1}^{N-1} \left[\mathrm{Res}'(i+1) - \mathrm{Res}'(i)\right]^2}{\sum_{i=1}^{N} \left(\mathrm{Res}'(i)\right)^2} \,. \tag{3.24} $$

Here, a value of Abbe = 0 means that the fit is constantly above or below the experimental data, while Abbe = 2 indicates an anti-correlated relation between fit and measured data. Consequently, Abbe = 1 is the expected value for randomly noised data points and statistically distributed residuals [164]. Figure 3.10 depicts a typical illustration of a fitted XPS spectrum. In this case, an artificial spectrum with normally distributed noise (black crosses) was created to demonstrate a perfect

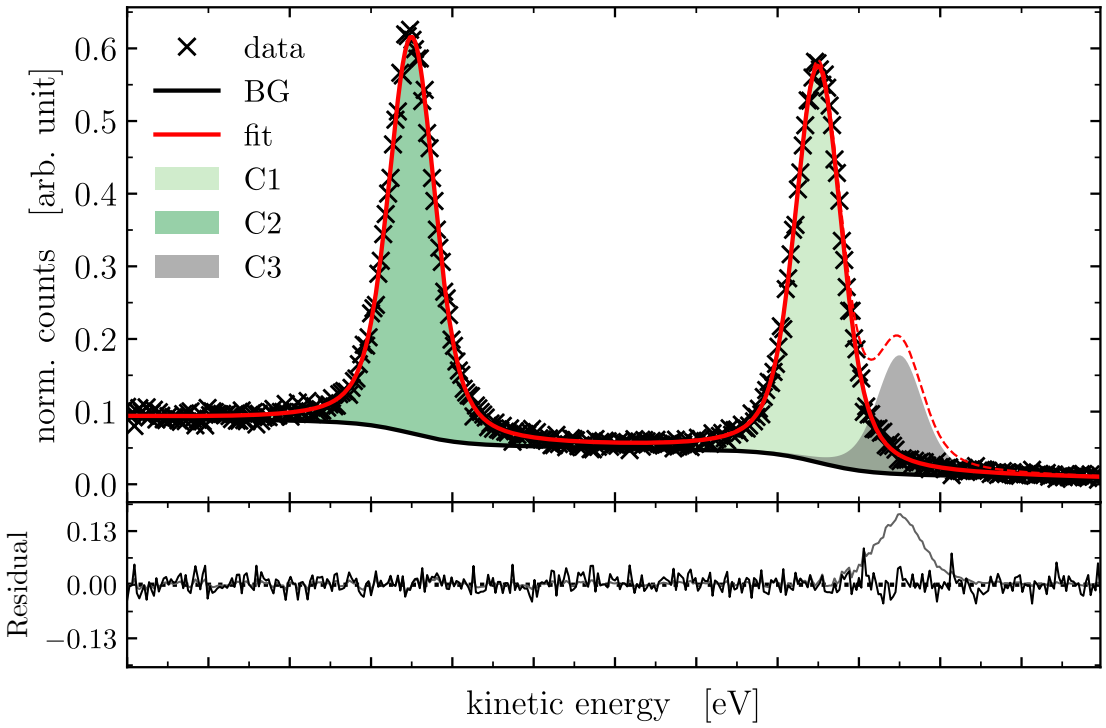

Figure 3.10: A virtual XPS data set fitted by two Voigt-like components, C1 and C2, and a Shirley BG. A perfect fit (solid red line) is indicated by the residual below (black line) and Abbe = 1.02. Adding C3 results in a poor fit (dashed red line) with a significant deviation in the residual (grey line) and a value of Abbe = 0.04.

fit (solid red line) of a Shirley background (solid black line) and two correctly shaped Voigt profiles C1 and C2 at the actual energy positions. The corresponding residual mirrors the normal distribution of the data points, which leads to a low residual and an excellent value of Abbe = 1.016. In contrast, a poor fit (dashed red line) generated by C3 can be directly identified by the deviation in the respective residual and confirmed by a poor Abbe = 0.039. To achieve the best fit of the experimental data, *UNIFIT 2022* takes usage of the Marquardt-Levenberg algorithm [139, 166]. This algorithm is based on the Gaussian-Newton algorithm purposing to minimize $\chi^2 = \chi^{2^*} \cdot (N-P)$ of the fit in dependency of the fit parameter set $\vec{p}$. The Marquardt-Levenberg algorithm is known for being very successful in finding a global minimum of χ^2, even for a non-optimal guess of initial start parameters $\vec{p}_\mathrm{i}$ [139]. Helpful advice for choosing a reasonable set of fit parameters can be found in further literature [154, 164, 167].

3.2 X-Ray Photoelectron Diffraction (XPD)

Up to this point, the propagation of photoexcited electrons through the solid has been considered a particle process. The fundamental approach for x-ray photoelectron diffraction (XPD) is the treatment of electrons as waves, which are scattered at the crystal potential and are able to interfere with primary and multiply scattered waves [111]. The first report about a significant angular dependency of the photoelectrons' intensities due to elastic scattering at neighboring atoms was released in 1970 by Kai Siegbahn [168]. In the following years, similar observations of the XPD effect were already used to determine the crystal structure of single crystals and adsorbate systems by the comparison of theoretically and experimentally obtained angular intensity distributions [169–171]. The resulting interference pattern of photoelectron waves over the hemisphere of the sample surface contains information on the structure of the sample. According to the chemical selectivity of the XPS-based technique, the

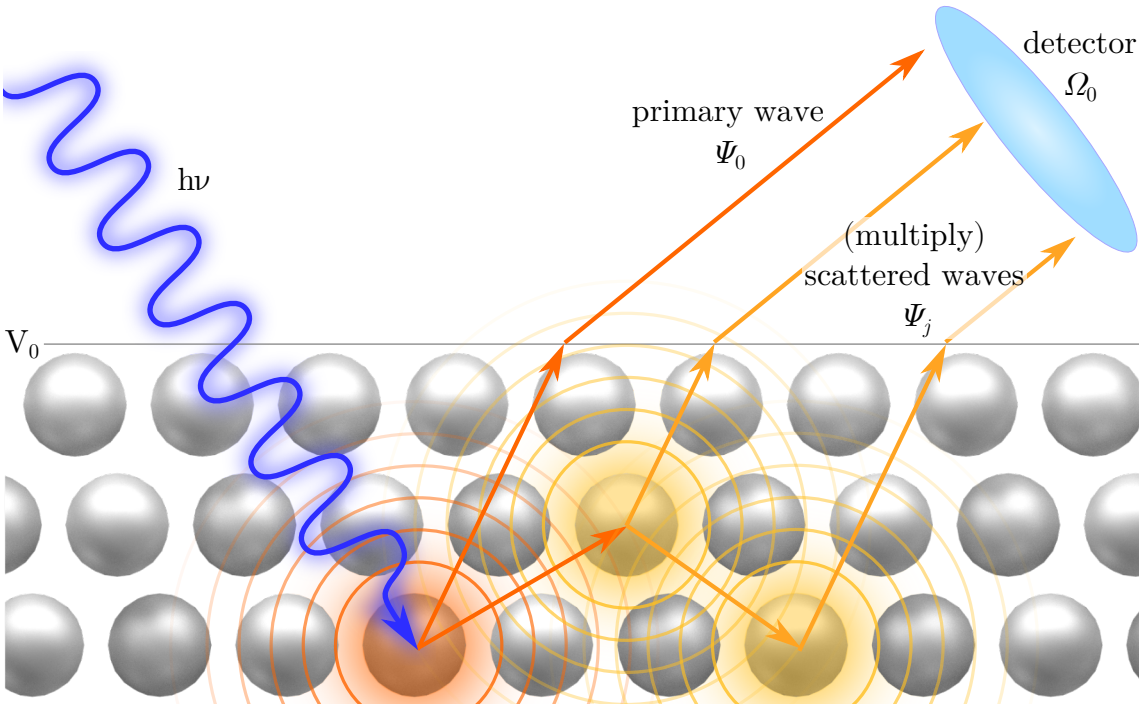

Figure 3.11: Illustration of the principle of photoelectron diffraction. The superposition of an emitted primary photoelectron wave Ψ_0 and (multiply) scattered waves Ψ_j result in an interference pattern recorded by a detector Ω_0, which contains the structure information of the sample.

structure data can be obtained for particular chemical environments [118, 172, 173]. Figure 3.11 shows the principle of photoelectron diffraction. A primary photoelectron wave $\Psi_0(\vec{k})$ from a localized emitter atom propagates through the crystal with a spherical wave function of

$$\Psi_0(\vec{k},\vec{r}) \propto \frac{1}{|\vec{r}|}\,\exp\left(i\,\vec{k}\,\vec{r}\right)\ . \tag{3.25}$$

Its $1/r$ dependency illustrates the method's high sensitivity to the local surrounding of the emitter instead of the long-range order of the sample. During the spreading of the primary wave in the solid, elastic scattering processes at neighboring atoms j lead to the emission of secondary and multiply scattered waves $\Psi_j(\vec{k})$. Because of the elastic scattering, all waves have the same wave vector $\vec{k}$, differing only by a phase shift regarding its location $\vec{r}_j$. Thus, the measured intensity $I(\vec{k})$ can be written as the sum over the final-state primary wavefunction $\Psi_0(\vec{k})$ and all final-state scattered wave functions $\Psi_j(\vec{k})$:

$$I(\vec{k}) = \left|\Psi_0(\vec{k}) + \sum_j \Psi_j(\vec{k})\right|^2\ . \tag{3.26}$$

It shall be noted that the phase shift of all waves, from which the crystal structure could be reconstructed, is lost during squaring the sum. However, a path-length difference between waves originating from two emitters k and l can geometrically be expressed as

$$\exp\left(i\,\vec{k}\,\vec{r}_k\right)\cdot\exp\left(i\,\vec{k}\,\vec{r}_l\right) = \exp\left\{i\,|\vec{k}|\,|\vec{r}_l|\cdot[1-\cos(\Theta_l)]\right\}\ , \tag{3.27}$$

with the scattering angle Θ_l, defined by polar and azimuthal angles [173, 174]. Equation (3.27) shows that the atomic distance $|\vec{r}_l|$ can be obtained from experiments with either varying $|\vec{k}|$ and E_{kin}, respectively, at fixed angles Θ_l (energy-scanned XPD) and *vice versa* (angle-scanned XPD) [173]. In this work, only angle-scanned XPD measurements $I(\Theta,\phi)$ are performed at constant kinetic energies E_{kin} and photon energies hν, respectively. However, an additional distinction between the

scattering angle Θ_l and the observation angle Θ has to be considered due to the refraction of the photoelectron waves at the surface [171, 175]:

$$\frac{\sin(\Theta_{\text{in}})}{\sin(\Theta)} = \sqrt{\frac{E_{\text{kin}} + V_0}{E_{\text{kin}}}} \,. \tag{3.28}$$

Hereby, Θ_{in} denotes the angle of the electron wave inside the solid with an inner potential V_0 and the emission and observation angle Θ, respectively.
Since a more detailed discussion of equation (3.26), including all contributing factors, can be found in further literature [172, 173], the influence of the atomic scattering factor $f_j(\vec{k})$ is briefly mentioned here. Besides the phase shift, the complex scattering factor $f_j(\vec{k})$ mainly defines the amplitude of the scattered waves. It strongly depends on the element of the emitter atom, the kinetic energy, and the scattering direction

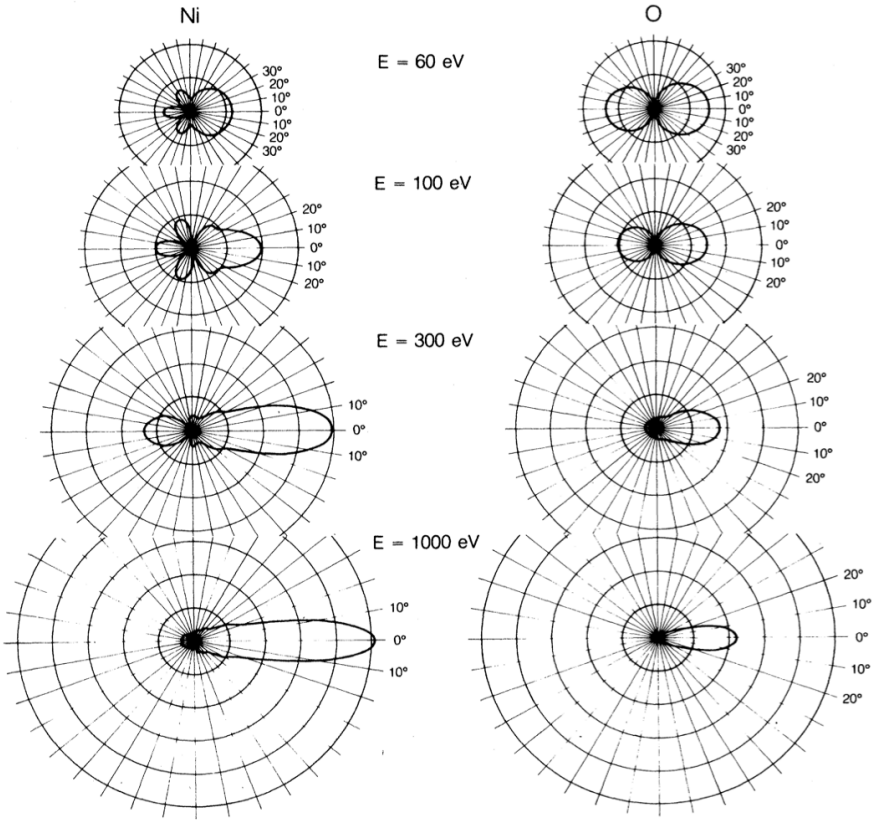

Figure 3.12: Visualization of the scattering amplitude mainly influenced by the complex scattering factor $f_j(\vec{k})$ at different kinetic energies E for Ni and O. Figure is taken from [176].

[176]. Figure 3.12 depicts exemplarily the angular distribution of the scattering factors $f_j(\Theta)\big|_{E_{\mathrm{kin}}}$ for the elements nickel and oxygen. For high kinetic energies $E_{\mathrm{kin}} < 300\,\mathrm{eV}$ a dominant amplitude is formed towards the $\Theta = 0°$-direction, which is called forward scattering [173, 176]. By choice of the kinetic energy of the emitter, not only the surface sensitivity but also the scattering behavior can be influenced. The plotted scattering amplitudes in figure 3.12 clearly demonstrate that diffraction patterns recorded for emitters with high kinetic energy have a dominant forward-scattering amount which is not as sensitive to the structure of the local environment as patterns obtained for lower kinetic energies. The accuracy of the XPD method for determining the atomic positions of a sample system is $\pm 0.5\,\text{Å}$ [173].

3.2.1 XPD-Data analysis

This section introduces the experimental procedure of the XPD measurements, followed by the data analysis. In this work, angle-resolved XPD measurements are performed, meaning the acquisition of intensity data I of a particular core level signal at E_{kin} for varying polar and azimuthal angles (Θ, Φ) and at a fixed excitation energy $h\nu$.

Experimental Data. The intensity modulation $I(\Theta, \Phi)$ of an XPD pattern, as exemplified on the left-hand side of figure 3.13, results from constructive and destructive interference of primary and scattered photoelectron waves. Single XPS HighRes spectra often do not allow to identify diffraction effects, whereas angle-resolved XPS measurements of the hemisphere above a well-ordered sample reveal an obvious diffraction pattern. Therefore, single HighRes XPS spectra are recorded for every angular matrix element (Θ, Φ) in a range of $2° \leq \Theta \leq 72°$ with an increment of $\Delta\Theta = 2°$ and $0° \leq \Phi < 360°$ with $\Delta\Phi = 1.8°$. Thus, an XPD pattern consists of 7200 data points. As shown on the right-hand side of figure 3.13, the intensities I correspond to integrated XPS spectra, which are color-coded visualized in a polar plot.

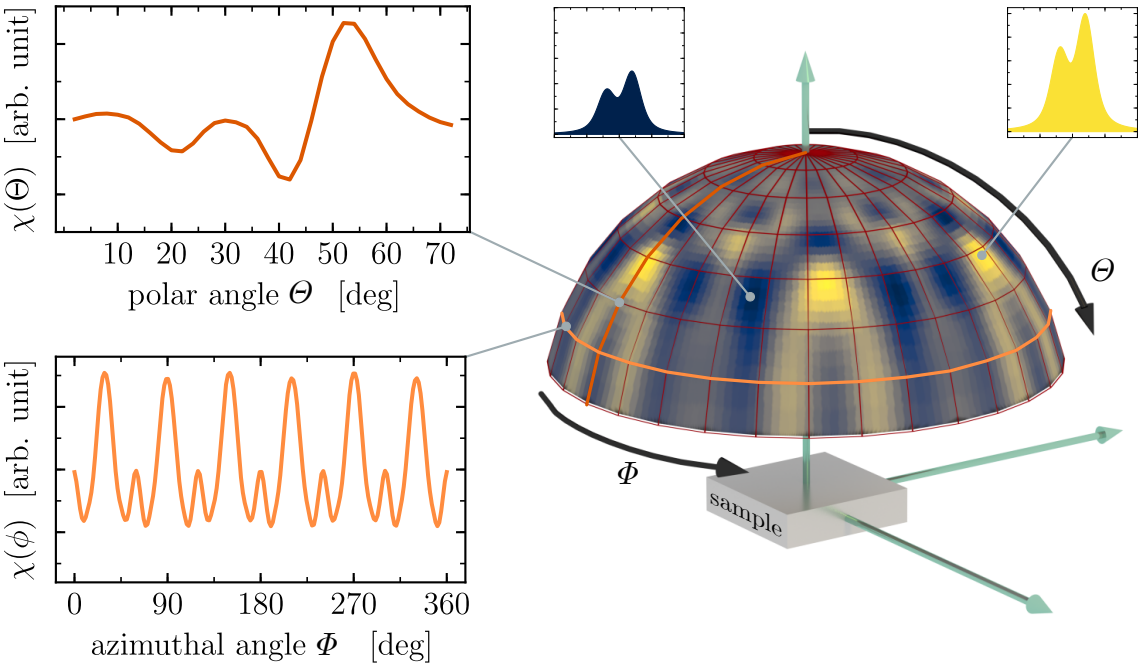

Figure 3.13: An experimental XPD pattern (right) represents the interference projection over the upper hemisphere of the sample's surface. The color-coded intensity modulation in polar Θ and azimuthal Φ direction (left) corresponds to integrated XPS spectra.

Due to the intensity decay of the synchrotron radiation (see section 4.2) during the recording of an XPD pattern, a normalizing anisotropy function $\chi(\Theta, \Phi)$ is applied to the data,

$$\chi(\Theta, \Phi) = \frac{I(\Theta, \Phi) - \overline{I(\Theta)}}{\overline{I(\Theta)}} \,. \tag{3.29}$$

$I(\Theta, \Phi)$ means the measured intensity at the hemisphere element (Θ, Φ), while $\overline{I(\Theta)}$ is the average intensity over the azimuthal angles Φ per polar angle Θ. The normalization of the raw experimental data by the anisotropy function $\chi(\Theta, \Phi)$ is part of the post-processing, which is shown in figure 3.14. Here, a pattern of the Ge $3d$ core level of a Ag_2Ge surface alloy is exemplarily used in order to demonstrate the typical post-production process of experimental XPD patterns. Figure 3.14(b) displays the obtained diffraction pattern after applying the anisotropy function (3.29) to the raw data (a). After subtracting a background (c) and the correction of the angular orientation of the pattern (d), the data are blurred by a Gaussian filter (e) in order to minimize statistical noise. Finally, adequate symmetry operations, for example, regarding the sample's crystal symmetries, can be applied to the pattern.

Figure 3.14(f) demonstrates the application of a mirror symmetry and a threefold rotational symmetry to the XPD data.

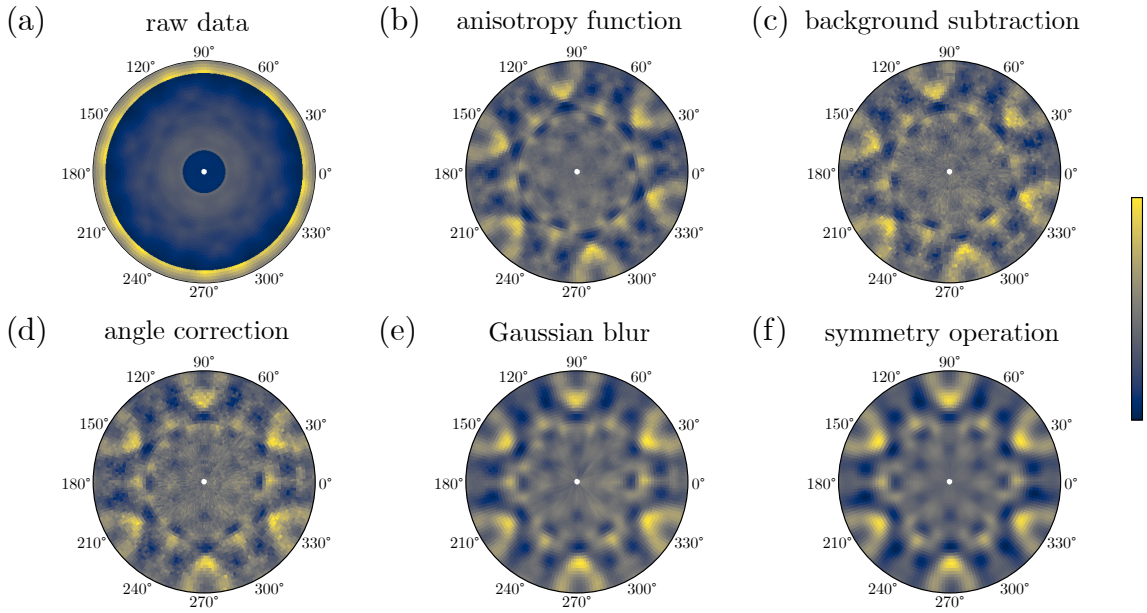

Figure 3.14: Overview of the post-processing steps of experimentally obtained raw data (a) up to the finally presented data (f).

Simulated Data. Because of the loss of the phase information within the measured intensity, a direct reconstruction of the investigated sample's structure is impossible. However, in order to determine the atomic structure of a sample system employing XPD measurements, XPD patterns of test structures are simulated. By comparing these patterns to the experimentally obtained XPD pattern, a consistency between test structure and sample structure can be achieved. Therefore, the reliability factor (R-factor), according to John Pendry [177], is used to evaluate the degree of agreement between simulation and experiment [174]:

$$\mathrm{R} = \frac{\sum_{\Theta,\Phi} \left[\chi_{\mathrm{sim}}(\Theta,\Phi) - \chi_{\mathrm{exp}}(\Theta,\Phi)\right]^2}{\sum_{\Theta,\Phi} {\chi_{\mathrm{sim}}}^2(\Theta,\Phi) + {\chi_{\mathrm{exp}}}^2(\Theta,\Phi)} \,. \tag{3.30}$$

The R-factor yields values between 0 and 2, while $R = 0$ indicates a perfect agreement between simulated and experimental patterns. Figure 3.15 further illustrates a complete independence of two patterns indicated by an R-factor of $R = 1$ and

the total anti-correlation at $R = 2$. Hence, an R-factor as close to 0 as possible between simulation and experiment should be achieved to obain the corresponding test structure with a sufficient consistency to the probed structure.

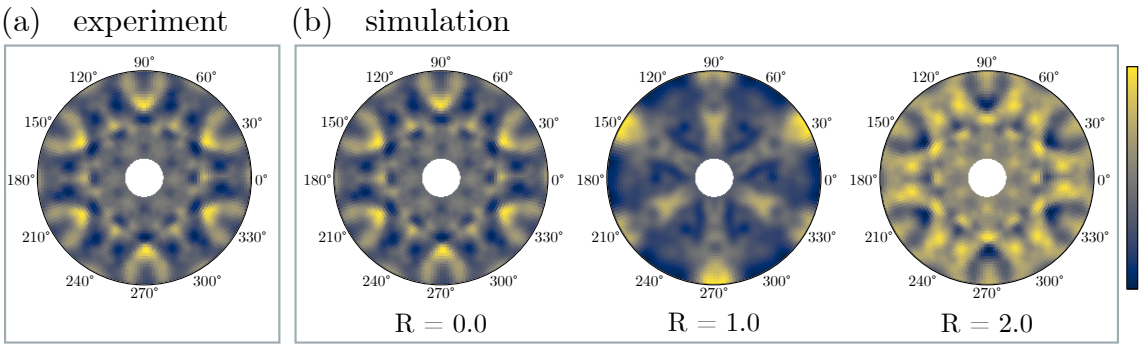

Figure 3.15: Examples of obtained R-factors for comparing the experimental XPD pattern (a) and simulated patterns (b).

The simulation package *EDAC* (electron diffraction in atomic clusters) is used in this work to calculate the XPD pattern of given test structures [175]. The package considers multiple scattering processes of electron waves at the nucleus potentials of cluster atoms, in the muffin-tin model [178], up to a scattering order of $n = 20$. Using an interative method to calculate the scattering path of propagating electrons, which includes a series expansion of the scattering matrix and exact Green's functions for the electrons' propagation, cluster structures of up to 1000 atoms can be regarded. Moreover, additional refraction of the emitted photoelectron waves at the inner potential V_0 of the solid is taken into account. The scattering radius r_{scat} of an emitter atom defines the reach of elastic scattering around the respective emitter and should be assumed as $r_{\mathrm{scat}} \approx 1.5 \cdot \lambda$ [175]. The IMFP λ is determined by the *TPP-2M* formula (3.11) within *EDAC*, which makes the simulation package most applicable for the XPD pattern of $E_{\mathrm{kin}} > 50\,\mathrm{eV}$, due to the energy domain of λ_{TPP-2M} [179]. The computation time of *EDAC* amounts $N^2(l_{\mathrm{max}}+1)^3$, with N contributing cluster atoms and the maximum angular momentum number considered l_{max}. [175]

A successful approach to finding a test structure whose simulated XPD pattern provides the minimum R-factor with respect to the experimental XPD pattern is to take advantage of a genetic algorithm as part of the analysis process [180, 181]. A schematic illustration of the operating principle of the genetic algorithm applied here is depicted in figure 3.16. At first, an initial start structure is developed from

literature or further measurements, which is subsequently forwarded to the algorithm. It creates a current set of 60 test structures by a random variation of the structural parameters of the initial test structure in a given range. A simulated diffraction pattern is calculated for each structure in order to evaluate its resemblance with the experimental pattern by means of the R-factor analysis (3.30). A set of test structures corresponding to the best-matching XPD patterns is created, which is updated at every iteration round. If a customized stop criterion is met, such as

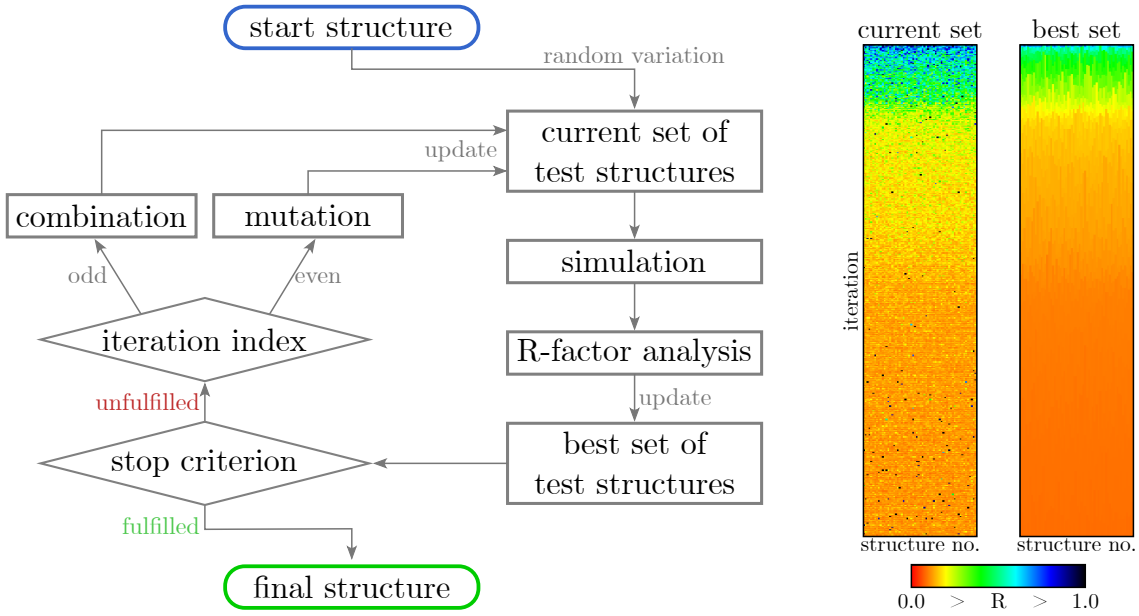

Figure 3.16: Flowchart of the proceeding of the genetic algorithm as an essential tool within the XPD analysis (left). An exemplary evolution of the R-factors of the current and the best set from an input start structure to the final output structure is color-coded depicted, resulting in R = 0.09 after 446 iteration steps (right).

reaching a certain R-factor value or a certain runtime, the algorithm is aborted, and the associated test structure of the lowest R-factor pattern is output as the final structure. If the stop criterion is not fulfilled, all structures are modified to set a new generation of the current set of structures. Depending on the iteration index, the modification of the test structures either means a combination of two structures or a random mutation, including translation, rotation, or scaling, of structural parameters. After a couple of iterations, a final structure can be found. [182] On the right-hand side of figure 3.16 an example of a simulation process is shown, visualizing the development of the R-factor in a heatmap. Sixty pixel in a line refer to each test

structure within the current and the best set, while every line represents an iteration step. The color code is explained by the color bar at the bottom indicating R = 0.0 and R = 1.0 in red and black, respectively. In this case, an R-factor of R = 0.09 was achieved after 446 iteration steps.

3.3 Low-Energy Electron Diffraction (LEED)

Low-energy electron diffraction (LEED) is probably the most prevalent technique in surface science because it provides a convenient and rapid way to gain knowledge about the long-range geometric structure of a probed sample's surface. Its high surface sensitivity is caused by the energy-depending IMFP of electrons in matter, as discussed in section 3.1.3. The most commonly used energy range for LEED experiments is $E_{\mathrm{kin}} \leq 200\,\mathrm{eV}$ [69]. The LEED technique is based on the wave character of propagating electrons and the associated ability to interfere [183]. Electrons with a mass of m_{e} have an attributed de Broglie wavelength of,

$$\lambda_{\mathrm{Brog}}(E_{\mathrm{kin}}) = \frac{\mathrm{h}}{\sqrt{2\,m_{\mathrm{e}} E_{\mathrm{kin}}}}\,, \tag{3.31}$$

which results in wavelengths of $1\,\text{Å} \leq \lambda_{\mathrm{Brog}} \leq 2\,\text{Å}$ within the energy range of operation. Thus, low-energy electrons satisfy the atomic diffraction condition to resolve interatomic distances [69]. When an electron beam with kinetic energy E_{kin} is accelerated onto an ordered sample surface, elastically backscattered electrons interfere constructively if the Laue condition is fulfilled:

$$\vec{k}_f - \vec{k}_0 = \vec{G}_{\mathrm{hk}}\,. \tag{3.32}$$

Here, $\vec{k}_0$ and $\vec{k}_f$ denote the wavevectors of the incoming and scattered electron beam, respectively, and $\vec{G}_{\mathrm{hk}}$ is the two-dimensional reciprocal lattice vector, as long as we only consider diffraction at the surface. The reciprocal lattice vector $\vec{G}_{\mathrm{hk}}$ of the surface is described by,

$$\vec{G}_{\mathrm{hk}} = \mathrm{h}\,\vec{a}^* + \mathrm{k}\,\vec{b}^*\,, \tag{3.33}$$

with the reciprocal unit vectors $\vec{a}^*$ and $\vec{b}^*$ to the corresponding real space unit vectors $\vec{a}$ and $\vec{b}$. Figure 3.17(a) shows the Laue condition (3.32), which can be visualized

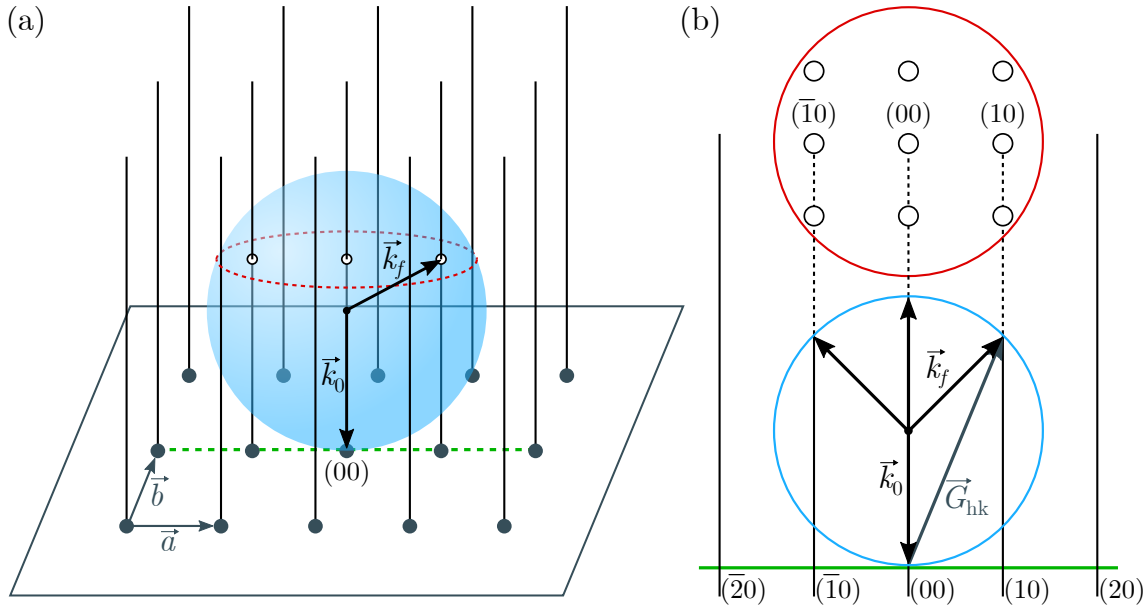

Figure 3.17: (a) The intersection points of reciprocal lattice rods and the Ewald sphere of the radius $\left|\vec{k}_0\right| = \left|\vec{k}_f\right|$ can be observed as reflective LEED spots. (b) Hereby, the spots are denoted after its order (hk). Reproduced from [69].

as a sphere, namely the Ewald sphere. As a consequence of the broken translation symmetry of the crystal structure at the surface, reciprocal lattice points of a three-dimensional bulk crystal turns into reciprocal lattice rods of the two-dimensional surface [69]. The points of intersection between the Ewald sphere and the reciprocal lattice rods can be observed as reflection spots of the order (hk), as denoted in figure 3.17(b). Since $\vec{k}_0$ defines the radius of the Ewald sphere, diffraction patterns that are recorded at increasing kinetic energies also reveal higher-order spots [183]. Analogous to section 3.2, the analysis of the diffraction spots' intensities allows to determine the crystal structure of a probed sample. This method, named as $I(E)$ or IV LEED, bases on an energy-depending intensity modulation of the reflection spots due to kinetic diffraction theory and multiple electron scattering effects. The spot intensity is determined by the structure factor of a sample, which considers the atomic scattering factors $f_j(\vec{k})$ of the respective atoms at the location $\vec{r}_j$. This leads to a modulating intensity course along the lattice rods displayed as constants in figure 4.5(a), which results in differently intense diffraction spots, as intersections of the lattice rods and the Ewald sphere, at varying kinetic energies. Additionally, the

spot intensities are amplified or attenuated due to multiple scattering effects. $I(E)$ or IV curves can be yielded by recording the intensities I of particular reflection spots in dependency on the corresponding primary energy E. Thus, a precise structure model of the probed sample can be obtained by the iterative simulation of IV curves similar to the XPD analysis introduced above. [183]
However, also a study on the spot shape and geometry of LEED patterns can enable the identification of the long-range order of a sample or the estimation of the crystal structure and the lattice constants [69, 183].

Chapter 4

Experimental Setup

In this chapter, the experimental setup will be introduced that was used for the sample preparation and the measurements. All preparation and analysis steps were conducted *in situ* under ultra-high vacuum (UHV) conditions to preserve the prepared surfaces' maximum purity. Due to the high surface sensitivity of the methods carried out here, it is inevitable to avoid as much contamination of the investigated surfaces as possible. Roughly speaking, since it takes only 1×10^{-10} s under atmospheric conditions to cover 1 % of a sample's surface with residual gas atoms, this time is extended to 100 s under UHV conditions at a pressure of 1×10^{-10} mbar [70]. The UHV chamber, which was used meets these requirements and will be presented in the following section 4.1. Additionally, the synchrotron radiation source DELTA will be introduced in section 4.2, that was used for performing photoemission experiments.

4.1 Ultra-High Vacuum Chamber

The UHV chamber utilized in this work to carry out all preparation and measurement procedures represents the endstation of beamline 11 (BL11) at DELTA. The chamber is made of so-called μ-metal, which means permalloy, whose high magnetic permeability allows to shield the inside of the chamber against interfering magnetic fields, like the earth's magnetic field. Especially for angle preserving diffraction experiments with low-energy charged particles, it is crucial to avoid the disturbance of those external influences. Ultra-high vacuum typically starts at a pressure of $p < 1 \times 10^{-8}$ mbar. The chamber mentioned here has a base pressure of $p = 5 \times 10^{-11}$ mbar which perfectly fulfills the requirements for contamination-free sample preparations and long-term measurements. The end vacuum is stepwise reached by firstly evacuating

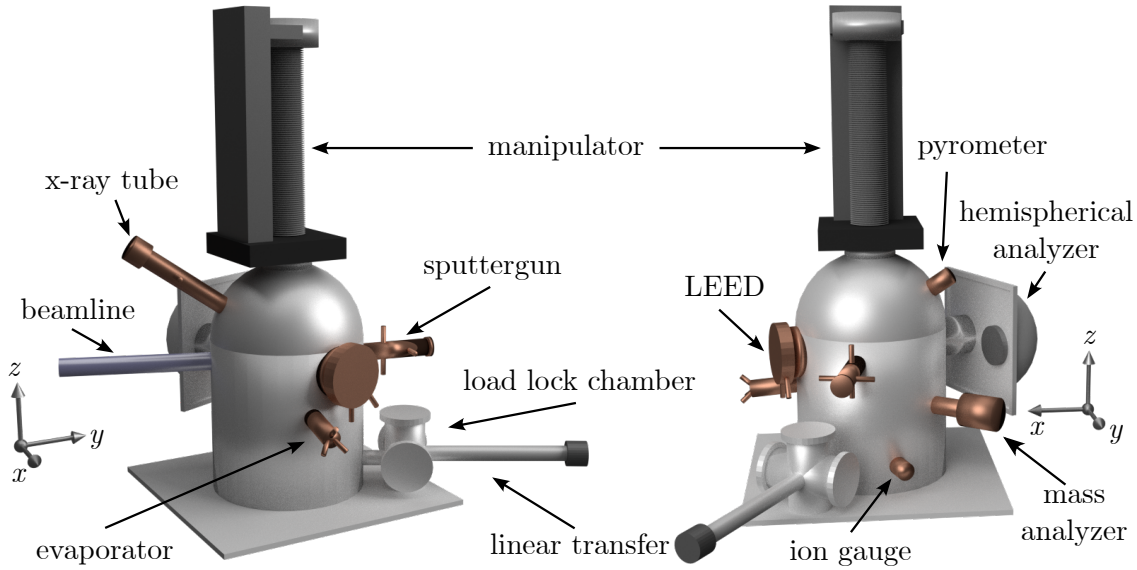

(a) left side view (b) right side view

Figure 4.1: Principle setup of the experimental UHV chamber with all attached analysis and preparation components, for example, the hemispherical energy analyzer and the manipulator. Unutilized flanges and windows are neglected in this illustration.

the chamber to a fore-vacuum (FV) at a pressure of $p_{\mathrm{FV}} = 1 \times 10^{-3}$ mbar by using scroll pumps. Subsequently, turbo-molecular pumps can initially help the chamber to reach a pressure of typically $p_{\mathrm{HV}} = 1 \times 10^{-7}$ mbar until a bakeout of the chamber becomes necessary. Since the inner surface of a chamber is generally covered with atmospheric gas molecules, like H_2O or CO_2, its temperature-depending desorption probability and molecular mobility can be increased by heating the chamber. The desorbed particles can now be evacuated within a few seconds [70]. In this case, a bakeout procedure for approximately 120 h at a temperature of $T_{\mathrm{bo}} = 160\,^{\circ}\mathrm{C}$ was conducted, considering all temperature-sensitive components. Moreover, the UHV chamber is equipped with further pumping systems, like a titanium sublimation pump (TSP) and a combined ion and non-evaporable getter pump (NEG). Also, monitoring devices, like a hot-filament ionization gauge and a quadrupole mass analyzer (*PrismaPro® QMG 250*, Pfeiffer Vacuum GmbH) are attached to the chamber in order to measure the pressure and determine the composition of the residual gas, respectively. Details about the functional principle of the vacuum technology mentioned should be neglected in this work and can be found in further literature

[69, 70]. A sketch of the UHV chamber is displayed in figure 4.1. In order to transfer a sample from outside the vacuum into the main chamber, the sample is first injected into the load lock chamber. After some hours of pumping, the sample can be moved into the main chamber using a linear transfer feedthrough without breaking the vacuum of the main chamber. The following sections will introduce all further preparation and analysis components, such as the manipulator, the sputtergun, the evaporator, and the hemispherical energy analyzer.

4.1.1 Sample Manipulation

As schematically illustrated in figure 4.2, a sample holder was used to comfortably handle the sample inside the vacuum during all preparation and analysis stages. The cylindrical Ag sample with a diameter of 9.9 mm and a thickness of 2.0 mm is inserted into the head of the sample holder and fixed by a thin tantalum ring. The sample holder has integrated heating which is placed under the sample in a small cavity inside the head. As shown in figure 4.2(b), the heating consists of a winded tungsten filament with a thickness of 0.15 mm, which is contacted to the contact

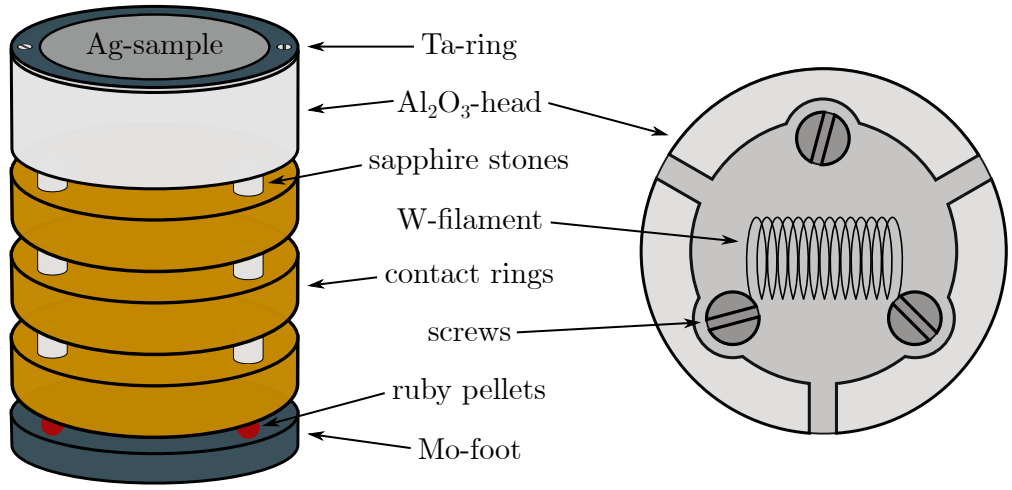

(a) side view (b) top view

Figure 4.2: Schematic sketch of the sample holder (a) in the side view with a sample inserted and (b) in the top view without a sample to show the heating filament.

rings by the screws. The basis of the sample holder, as well as its head, is made of isolating Al_2O_3, which allows the use of the heating in electron beam (EB) mode and in resistive (RES) mode. The sapphire stones and ruby pellets serve to isolate the contact rings from each other and the molybdenum foot of the sample holder, respectively. After transferring the sample in its holder from the load lock chamber to the main chamber, it is attached to the 5-axis manipulator by screwing on the Mo-foot.
Using the manipulator, the sample can be moved in x-, y-, and z-direction, as well as continuously rotated around the sample's normal in the azimuthal direction Φ and around the z-axis in the polar direction Θ. Both of these motorized rotations provide an angular resolution of 0.05°. Sliding contacts on the manipulator as counterparts to the contact rings of the sample holder realize a constant electrical contact during a continuous azimuthal rotation. Here, the third contact was used to ground the sample to avoid electrostatic charging from ion bombardment or photoemission experiments.

4.1.2 Sample Preparation

The UHV chamber is equipped with several components for sample preparation, as it is visualized in figure 4.1. Since the sample preparation procedure is described in detail in chapter 5, the focus here is on introducing the components used for this purpose.
In order to initially clean a sample from adsorbed residues after transferring it to the vacuum, an ion source (*IQE 12/38*, SPECS Surface Nano Analysis GmbH) is used, as it is shown in figure 4.3(a). Employing this so-called sputtergun, ions of noble gases such as argon are used to bombard the sample's surface at an angle of $\Theta = 60°$ with respect to the surface normal. Due to the momentum transfer of the Ar-ions with tunable kinetic energies of $0\,\mathrm{eV} < E_{\mathrm{kin}}(\mathrm{Ar}^+) \leq 5000\,\mathrm{eV}$ to adsorbed residues, atoms can be removed from the surface. Subsequent annealing of the sample is necessary to heal damaged areas of the surface. The temperature of the sample is measured by a pyrometer (*IMPAC® IGA 6/23 Advanced*, LumaSense Technologies GmbH) that is mounted outside the UHV chamber. These preparation cycles must be repeated several times until proof of sufficient surface quality is provided. The low-dimensional structures of germanium are grown epitaxially on the previously

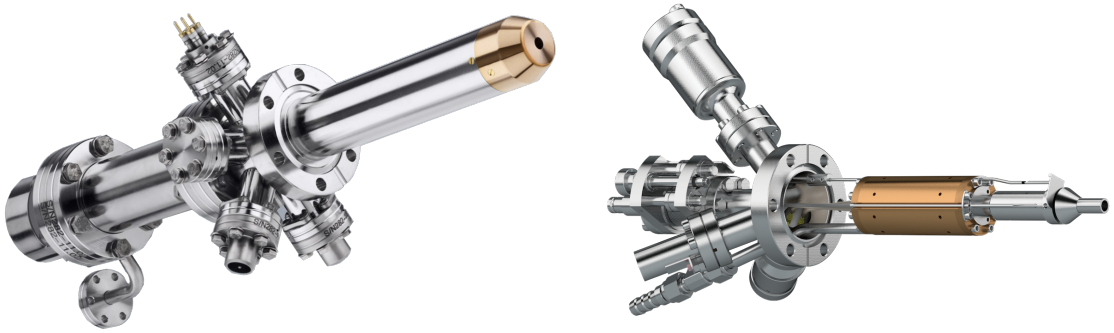

(a) Sputtergun [184]. (b) Evaporator [185].

Figure 4.3: Pictures of (a) the sputtergun and (b) the EB evaporator used in this work for preparation.

prepared Ag surface. Therefore, an electron beam evaporator (*EFM 3*, FOCUS GmbH), as depicted in figure 4.3(b), is used, which deposits thin films of a material onto a surface via physical vapor deposition (PVD). A tungsten crucible is filled with germanium pellets, as it is shown in figure 4.4, and inserted into the evaporator. By applying a high voltage U_{HV} between a filament and the crucible of $U_{\mathrm{HV}} = 2\,\mathrm{kV}$, the germanium is annealed to a temperature of approximately $T = 900\,^{\circ}\mathrm{C}$ until it sublimates. A collimator and a shutter at the tip of the evaporator allow for alignment of the vapor beam and control of the the deposition time, respectively. The evaporation power P_{em} is determined by the voltage U_{HV} and the emission current I_{em} between the filament and the crucible. An estimation of the deposition

Figure 4.4: Illustration of a tungsten crucible used here for the evaporation of germanium pellets. A quarter dollar (left) serves as a scale.

rate in dependency of the evaporation power P_{em} can be yielded from measurements with a quartz crystal microbalance (*QO 40A1*, PREVAC sp. z.o.o.) and its thickness monitor readout (*TM14*, PREVAC sp. z.o.o.) at an external test chamber. An oscillating quartz crystal with an initial frequency of $f_0 = 6\,\mathrm{MHz}$ is deposited with germanium which causes a change Δf in the oscillating frequency. From this Δf one can calculate the deposited mass Δm [186] and so the thickness of the deposited film. Additionally, the UHV-chamber offers an x-ray source (*XR 50*, SPECS Surface Nano Analysis GmbH) to check the chemical composition of prepared sample systems through XPS survey measurements.

4.1.3 LEED System

For performing diffraction measurements with low-energy electrons, a 4-grid LEED system (*ErLEED 150*, SPECS Surface Nano Analysis GmbH) is used, schematically illustrated in figure 4.5. As the theoretical background of LEED has already been discussed in section 3.3, here, an overview of the experimental principle is provided. Inside the electron gun, a thoria-coated iridium hairpin cathode emits electrons, which are accelerated and focused by several electro-optical elements. The electron beam leaves the gun with defined kinetic energy E_{kin}, which is freely tunable in the range of $0\,\mathrm{eV} \leq E_{\mathrm{kin}} \leq 3000\,\mathrm{eV}$, heading to the sample. The electrons, which got backscattered at the sample's surface, are guided through an additional μ-metal shield to pass through the grid system without being disturbed by magnetic fields. Four grids form the grid system to filter inelastically scattered electrons. The first and the fourth grid are on the same ground potential as the sample to shield the retrading field between grids two and three from the sample and the fluorescent screen. Additionally, the ground potential of the fourth grid reduces field penetration due to the potential difference of a few kilovolts between the fluorescent screen and the suppressor grid three [183]. The screen is on a high positive potential to accelerate the elastically scattered electrons onto it in order to achieve the maximum luminous effect. A camera that is placed behind the screen records the diffraction pattern. [69]

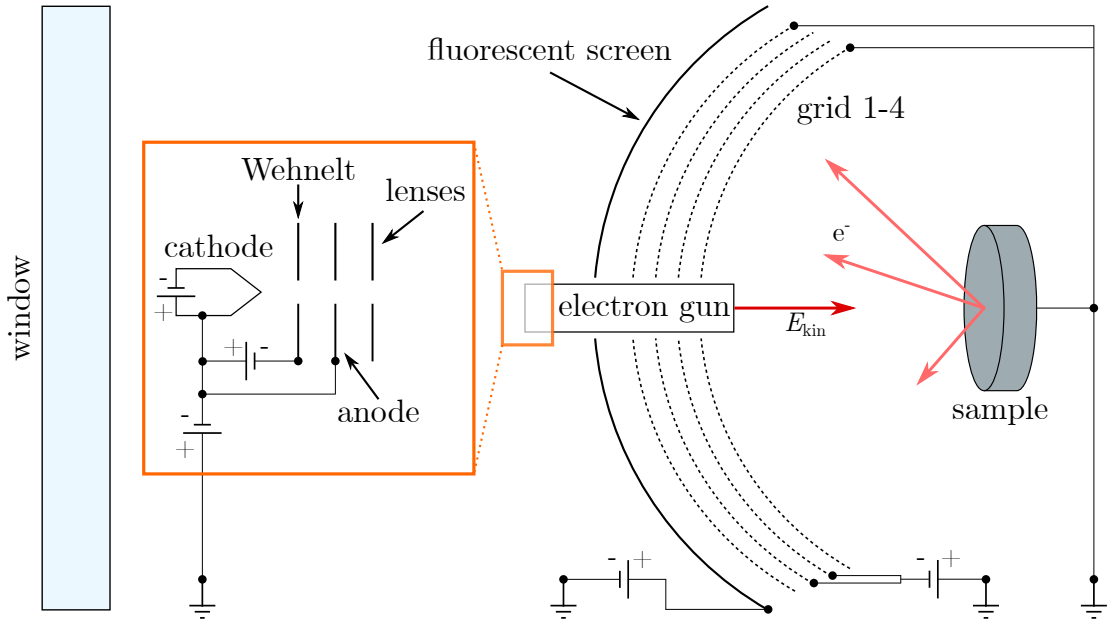

Figure 4.5: A principle sketch of a LEED system used here, consisting of an electron gun, a 4-grid system, and a fluorescent screen that can be observed through a window flange. Figure after [69].

4.1.4 Hemispherical Energy Analyser

All photoemission experiments performed at DELTA require a device that realizes the dispersive energy detection of photoelectrons. For this purpose, a hemispherical energy analyzer (*CLAM IV*, VG Microtech), as it is principally sketched in figure 4.6, is mounted to the UHV chamber with an angle of $\alpha = 55°$ regarding the synchrotron radiation beam. This theoretically determined *magic angle* of $\alpha_m = 54.7°$ between the x-ray source and analyzer minimizes the distortion of the measured counts of electrons through the polarization effects of the exciting radiation [187]. The analyzer (HEA) is linked to a one-dimensional so-called channeltron detector which consists of 9 channel electron multipliers (CEM). After the photoemission, the photoelectrons within an emission cone of the acceptance angle Θ_{HEA} of the HEA are collected by an electric field provided by the electrostatic lens system and focused towards the entrance slit of the analyzer. Immediately prior to this slit, the kinetic energy selection E_{kin} of the electrons is performed by letting them pass a retarding field. Entering the electric field between the hemispheres of the analyzer, the electrons with a kinetic energy equal to the pass energy E_{pass} follow a trajectory through

the entire sector of 165° on a mean radius of $R_0 = 150\,\text{mm}$ to the detector. Since electrons with kinetic energies of $E_{\text{kin}} \lessgtr E_{\text{pass}}$ are annihilated at the inner walls of the analyzer, only those with energies of $E_{\text{kin}} = E_{\text{pass}} \pm \Delta E$ are detected, while ΔE is defined by the energy resolution. [118, 120, 188]
Variable exit slits ($0.5\,\text{mm} \leq d \leq 5\,\text{mm}$) can additionally be used to increase the energy resolution before the photoelectrons are multiplied within the CEM and detected by a counting unit. The amplification of the CEM is realized by avalanching the formation of secondary electrons from the lead glass-coated walls of the CEM. An applied high voltage to the CEM of $1.8\,\text{kV} \leq U_{\text{CEM}} \leq 3.5\,\text{kV}$ makes each work as a continuous dynode which is capable of multiplying single electrons by factors of $10^6 - 10^8$. [189]

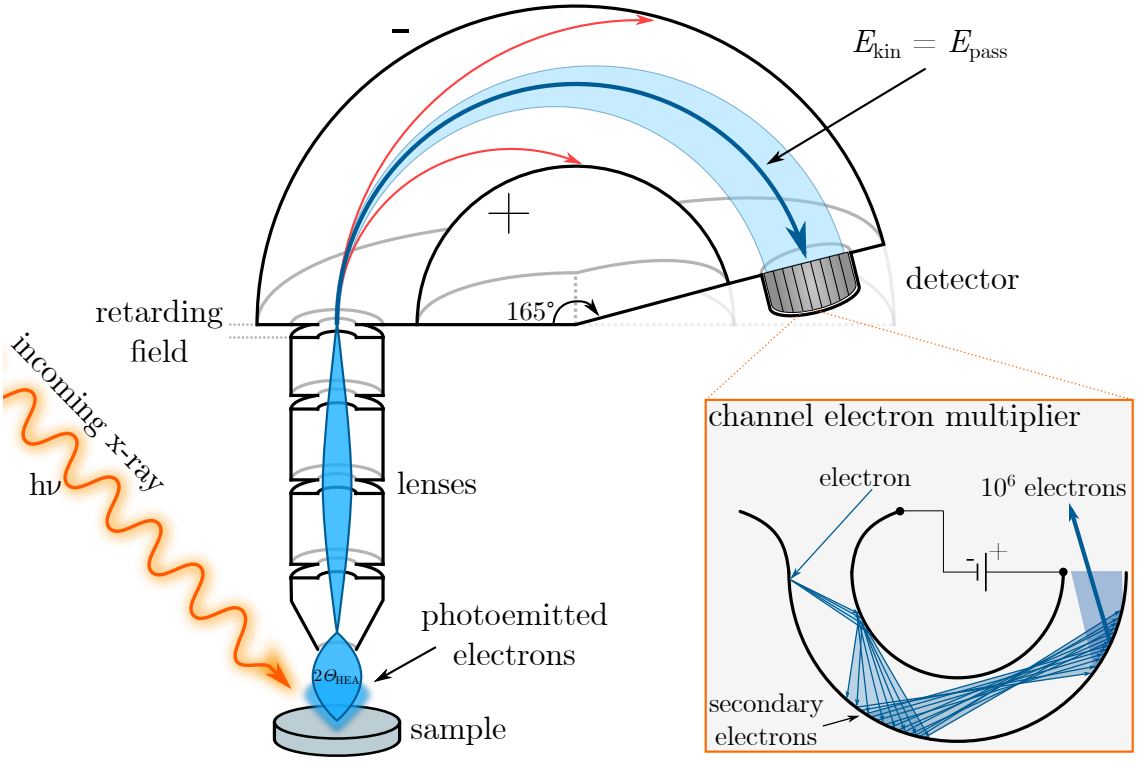

Figure 4.6: Principle sketch of an hemispherical energy analyzer as used here, consisting of a lens system, the energy analyzer sphere of 165°, and the detector. A close-up of the CEM demonstrates the process of electron amplification. Figure after [188].

4.2 Synchrotron Light Source DELTA

Since its discovery in 1947, synchrotron radiation has been preferred for x-ray scattering experiments because of its superior properties to conventional x-ray sources, such as x-ray tubes. For example, synchrotron radiation is of high intensity and brightness, provides a very broad and continuous spectral range, and shows a high degree of polarization. From the development of the first generation of synchrotron light sources, which was the parasitic use of radiation emitted from synchrotrons' bending magnets [190], the progress in producing synchrotron light of increasing brilliance even overtook Moore's law over the past years [2, 191]. With the use of second and third-generation synchrotron light sources from insertion devices, like wigglers and undulators, respectively, it is possible to achieve high-intensity radiation brighter than the sun by a factor of more than 10^{10} [190, 191]. But this is even far from the end of the road since fourth-generation synchrotron light sources as

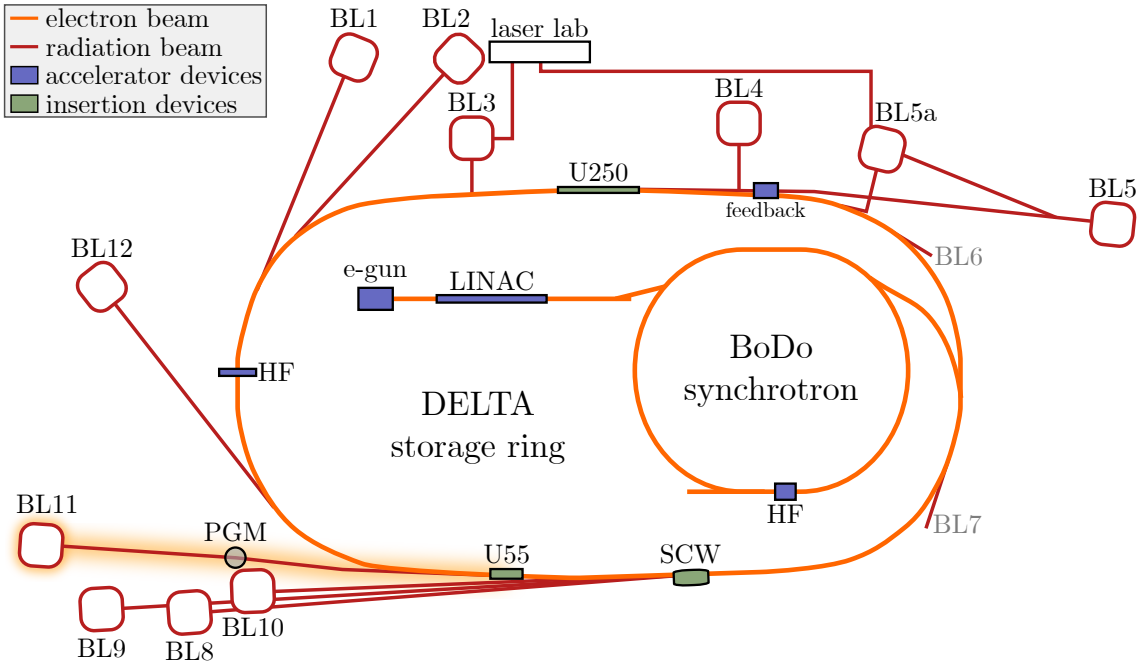

Figure 4.7: Schematic drawing of the current setup of the 1.5 GeV-electron storage ring DELTA, including main accelerator and insertion devices. The beamlines and their respective endstations are painted red, while BL11 is highlighted by a yellow glow. Figure after [192].

free-electron lasers (FEL) are predicted to provide fully coherent radiation with peak brightnesses that are 10^{14} times higher than those of the undulator [190].

The Center for Synchrotron Radiation in Dortmund (Germany) runs the electron storage ring DELTA (*german:* **D**ortmunder **El**ek**t**ronen Speicherring**a**nlage) and is one of more than 50 synchrotron light source facilities in the world [193]. The schematic drawing in figure 4.7 shows the electron storage ring DELTA with its pre-accelerators LINAC and the booster synchrotron BoDo. An electron gun emits an electron beam of $I = 1.8\,\mathrm{A}$ and accelerates the particles to a kinetic energy of $E_{\mathrm{kin}} = 50\,\mathrm{keV}$. The LINAC is a disk-loaded waveguide which uses electromagnetic waves for acceleration of electrons. The electron beam is injected into the synchrotron BoDo with a perimeter of 50 m, which increases the electron's energy from $E_{\mathrm{kin}}\big|_{\mathrm{LINAC}} = 70\,\mathrm{MeV}$ up to $E_{\mathrm{kin}}\big|_{\mathrm{BoDo}} = 1.5\,\mathrm{GeV}$ utilizing an 500 MHz-cavity. As soon as the final kinetic energy of $E_{\mathrm{kin}} = 1.5\,\mathrm{GeV}$ is reached, the beam is injected in electron bunches into the storage ring with an orbit length of 115 m. The electron beam with a maximum current of $I = 130\,\mathrm{mA}$ is stored with a lifetime of approximately $\tau > 25\,\mathrm{h}$. Since no top-up mode has been realized yet, an exponential decay of the electron beam due to scattering processes and intra-beam interactions has to be considered in long-term measurements. Currently, ten beamlines are capable to tap synchrotron radiation which is provided by bending magnets (BM), a superconducting wiggler (SCW), the undulator U250 and FEL, as well as the undulator U55.

4.2.1 Beamline 11

Beamline 11 (BL11) belongs to the soft x-ray beamlines at DELTA and provides synchrotron radiation for the UHV endstation, as introduced in section 4.1. An illustration of the beamline setup is shown in figure 4.8. Its radiation is produced by the U55, consisting of 47.5 poles of permanent magnets that are alternately arranged with a periode of 55 mm [194]. The alternating orientation of the magnetic field forces the electron beam on a transverse wiggling trajectory which stimulates the emission of synchrotron light in the direction of the electron beam due to the continuous acceleration of charged particles. The feature of an undulator is the small amplitude of the wiggling orbit, which leads to interference within the radiation beam. Destructive interference causes a discrete spectrum of the emitted radiation,

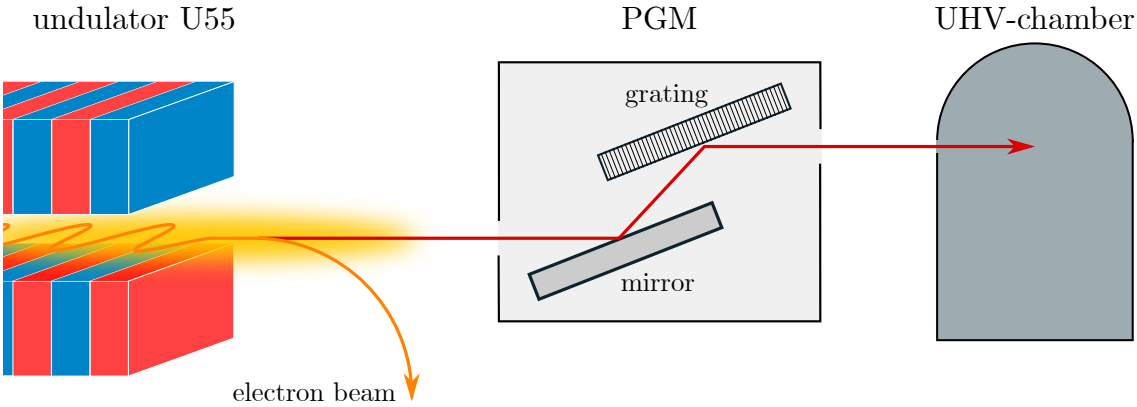

Figure 4.8: Principle sketch of beamline 11 at DELTA with the main insertion and optical devices to provide and adjust synchrotron radiation. The distance between U55 and the focus point inside the UHV chamber measures $l = 27\,\mathrm{m}$ [194].

whereas constructive interference even magnifies the intensity of the light at specific photon energies $h\nu$ of each harmonic n. The maximum intensity, which exceeds that of an x-ray tube by several orders of magnitude, is adjustable at any energy $h\nu$ by the strength of the magnetic field of the undulator. [190] As visualized in figure 4.8, the

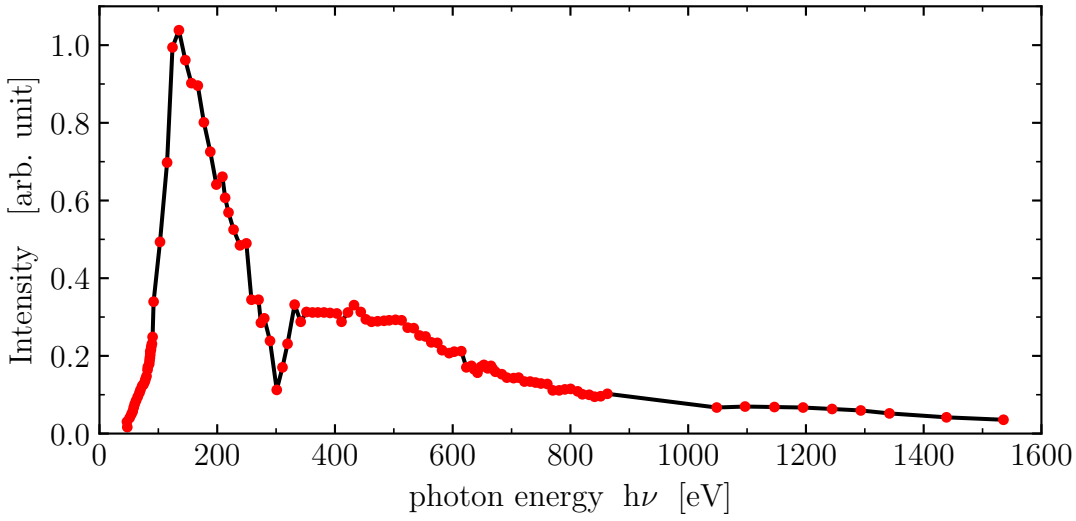

Figure 4.9: Performance of the radiation brilliance at BL11 in dependency on the photon energy $h\nu$. The maximum brilliance can be reached at an energy of approximately $h\nu = 140\,\mathrm{eV}$ with the first harmonic.

synchrotron radiation is then guided into a plane-grating monochromator (PGM). A relative alignment through translations and rotations of a plane grating and a plane mirror allows to band-pass the incoming synchrotron radiation for the desired photon energy. Subsequently, the light is focused and steered through an exit slit into the UHV chamber. The beamline covers a broad energy spectrum in the soft x-ray range, in which the energies of $50\,\mathrm{eV} \leq \mathrm{h}\nu \leq 1500\,\mathrm{eV}$ are freely tunable [194]. Figure 4.9 displays the x-ray's intensities at different energies $\mathrm{h}\nu$, where the maximum brilliance can be achieved at approximately $\mathrm{h}\nu = 140\,\mathrm{eV}$ with the first harmonic. In maximum energy resolution mode with $\frac{E}{\Delta E} = 30{,}000$ or in maximum photon flux mode with $N = 2 \times 10^{13}\,\mathrm{s}^{-1}(100\,\mathrm{mA})^{-1}$ the illuminated spot on the sample sizes $(70 \times 30)\,\mu\mathrm{m}^2$. [194]

Chapter 5

Sample Preparation

The following chapter presents the proceeding of the samples' preparation. First, the procedure to obtain a clean and reconstructed Ag(111) surface as a substrate is introduced. The synthesis of thin film germanium structures with the aim of forming 2D germanene and its precursors is discussed in the following section 5.2.

5.1 Reconstructed Ag(111)

Ag(111) was chosen as the carrier substrate for the synthesis of germanene. Therefore, a monocrystalline sample is used with a diameter of 9.9 mm, a thickness of 2.0 mm, and a purity of $> 99.999\,\%$. The surfaces of the Ag(111) samples are aligned with an accuracy of $< 0.1°$ with respect to its normal and polished to a maximum roughness of 0.03 µm. All substrates used here are provided by *MaTecK Material Technologie & Kristalle GmbH* and *Surface Preparation Laboratory B.V.*
In the purpose of a homogeneous and well-ordered growth of germanene, it is necessary to use a contamination-free and reconstructed surface of the substrate at an atomic scale. It is impossible to achieve this state under ambient conditions, as the surface is constantly exposed to the atmosphere, which causes impurities. For this reason, the sample preparation is conducted *in situ* in the UHV chamber, as illustrated in chapter 4.1. Before the sample is inserted into the head of the sample holder, as described in section 4.1.1, the surface is cleaned from macroscopic dust particles and suchlike with the help of dry nitrogen gas. After the transfer into the UHV chamber, an XPS survey spectrum was recorded under normal emission $\Theta = 0°$ and with a photon energy of $h\nu = 700\,eV$ in order to characterize the chemical composition of the Ag(111) sample. The corresponding spectra are displayed in figure 5.1(a).

One can identify the commonly known core level features of silver, such as the $3d$ signal located at a kinetic energy of $E_{\mathrm{kin}}(\mathrm{Ag}\,3d_{5/2}) = 333.3\,\mathrm{eV}$. However, also signals of contamination residues by oxygen, carbon and an unknown feature X can be detected, originating from atmospherical adsorption on the sample surface. These undesirable residues are removed during the surface preparation in order not to disturb the 2D material growth. The proceeding of several preparation cycles, as

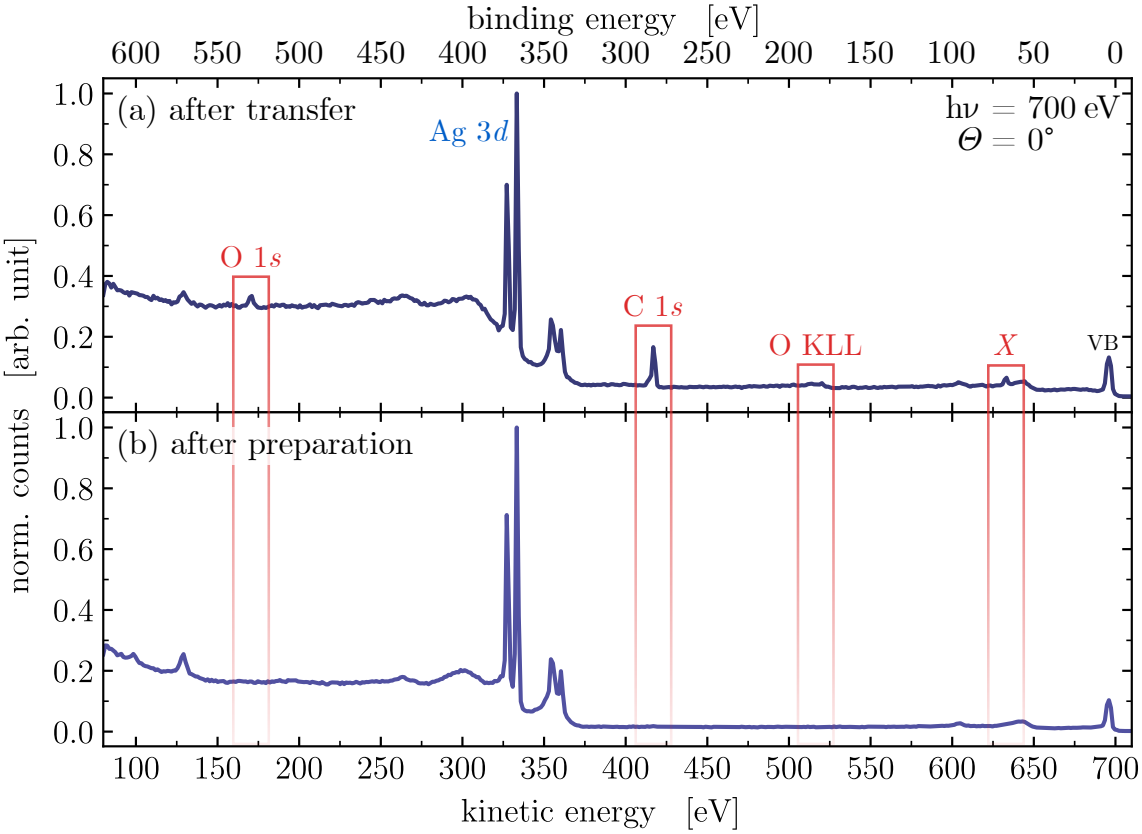

Figure 5.1: (a) XPS survey spectrum of an Ag(111) sample after the transfer into the vacuum with atmospheric impurities (red) and (b) after a sufficient number of preparation cycles without contamination residues. Both spectra are recorded at a photon energy of $h\nu = 700\,\mathrm{eV}$ and normal emission.

described in section 4.1.2, lead to a clean and reconstructed Ag(111) surface. Each cycle contains a grazing bombardment of the sample with Ar-ions at an angle of $\Theta = 60°$ and with kinetic energies of $600\,\mathrm{eV} \leq E_{\mathrm{kin}}(\mathrm{Ar}^+) \leq 700\,\mathrm{eV}$ for $t = 15\,\mathrm{min}$. During the so-called sputtering, the sample continuously rotates in Φ around its surface normal with a rotation speed of approximately $70\,°/\mathrm{min}$. Subsequently, the

sample is annealed to $T = 730\,\mathrm{K}$ for $t = 40\,\mathrm{min}$ by means of RES heating, followed by a careful cooldown procedure of around $t = 35\,\mathrm{min}$. After a sufficient number of preparation cycles, the survey spectra presented in figure 5.1(b) was recorded, in which all features of residues vanished. A wide-range XPS survey spectrum of a clean Ag(111) is displayed in figure 5.2, which was recorded with an Al-anode x-ray source providing K_α radiation of $\mathrm{h}\nu = 1486.6\,\mathrm{eV}$. Additionally, the binding energy E_{bin} of the spectra is added, which is referenced to the Fermi energy $E_{\mathrm{F}} = E_{\mathrm{bin}} + E_{\mathrm{kin}}$. The characteristic core level and auger lines of silver are marked by the corresponding labels, which can also be identified in figure 5.1 by their specific binding energy.
Besides the chemical purity of the surface, also its long-range order must be ensured for homogeneous and defect-free adsorbate growth. The surface order is checked by

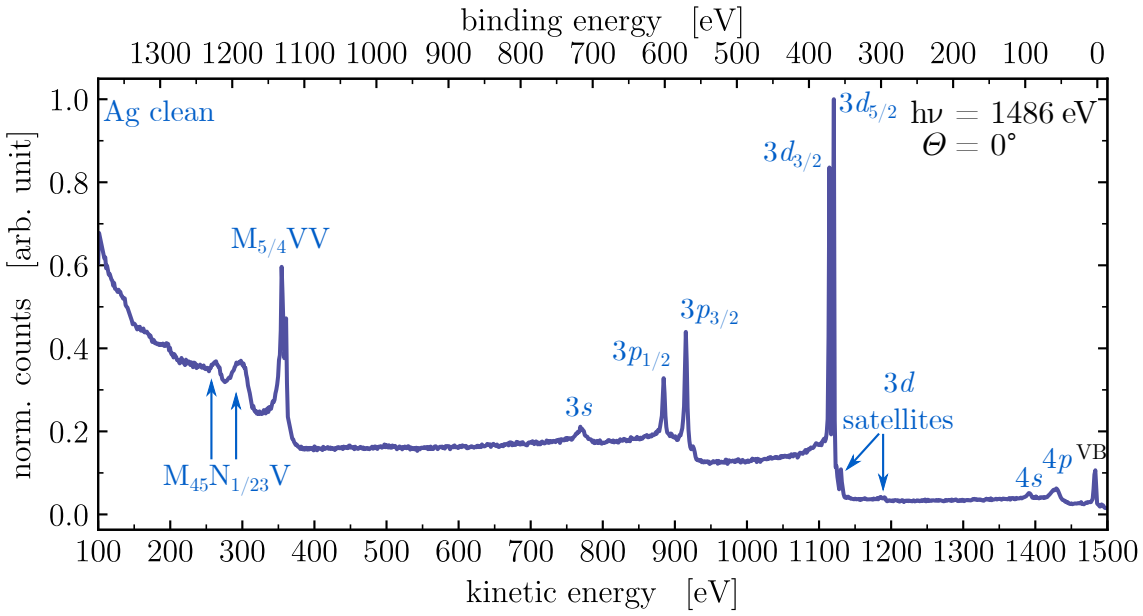

Figure 5.2: Wide-range XPS survey spectrum of a clean Ag(111) sample, measured with an Al-anode x-ray source with a photon energy of $\mathrm{h}\nu = 1486.6\,\mathrm{eV}$ and normal emission.

LEED measurements at different kinetic energies, which are depicted in figure 5.3. The displayed LEED pattern are obtained at kinetic energies of (a) $E_{\mathrm{kin}} = 46\,\mathrm{eV}$, (b) $E_{\mathrm{kin}} = 55\,\mathrm{eV}$, and (c) $E_{\mathrm{kin}} = 150\,\mathrm{eV}$. The crystal structure of Ag is a face-centered cubic (fcc) which appears as a hexagonal arrangement of diffraction spots for the (111) face. Figure 5.3(b) shows the (1×1) reconstruction of a well-ordered Ag(111) surface, indicated by the sharpness of the reflection spots, which clearly stand out

from the homogeneous background. These indication marks result from a long-range periodicity of the surface lattice [183]. Moreover, two groups of reflection spots with energy-modulated intensities can be noted in figure 5.3(a). Concerning the crystal structure of silver, including its stacking order of the crystal planes, these groups demonstrate the three-fold rotational symmetry of the Ag(111) crystal. As already mentioned in chapter 3.3, the size of the Ewald sphere defines the field of view of the reciprocal space and can be tuned by the kinetic energy E_{kin} of the electrons. Consequently, figure 5.3(c) also reveals higher-order reflection spots beyond the first BZ.

After the successful surface preparation of the Ag(111) substrate, the epitaxial growth of germanium structures is approached.

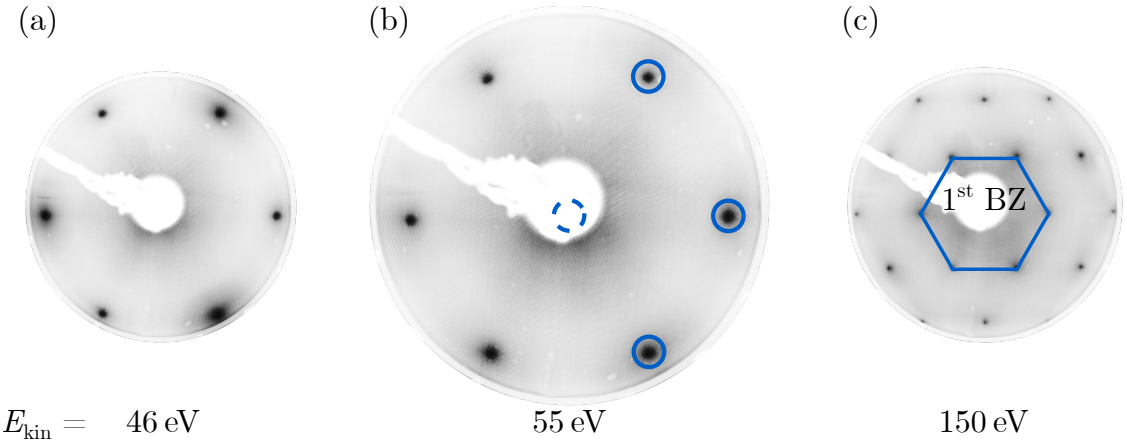

Figure 5.3: LEED of a clean and reconstructed Ag(111) sample at different kinetic energies of (a) $E_{\text{kin}} = 46\,\text{eV}$, (b) $E_{\text{kin}} = 55\,\text{eV}$, and (c) $E_{\text{kin}} = 150\,\text{eV}$. (b) The (1×1) reconstruction, and (c) the first Brillouin zone are highlighted with blue circles and lines, respectively.

5.2 Epitaxial Growth of Ge

The epitaxial growth of germanene phases on the Ag(111) substrate is realized by PVD procedure, as already discussed in section 4.1.2. The mentioned EB evaporator is filled with germanium pellets with a size of $< 1\,\text{mm}$ and a purity of 99.999 %. The alignment of the evaporator with respect to the sample can be achieved with the help of a linear hub and a port aligner, where the distance between the evaporator

and the sample measures 260 mm. During the evaporation process, the sample is constantly Φ-rotated and kept at a temperature of $T = 420\,\mathrm{K}$ to obtain homogeneous growth of the layers. After a warm-up time of $t = 20\,\mathrm{min}$ for the sample and the evaporator, the Ag(111) surface is deposited with germanium films of different layer thicknesses, which are tuned by the evaporation power of $P_{\mathrm{em}} = [20\,\mathrm{W}, 22\,\mathrm{W}]$ and the evaporation time of $10\,\mathrm{min} \leq t \leq 30\,\mathrm{min}$.
In order to determine the Ge layer thickness κ and surface coverage Λ, respectively, measurements of the evaporation rate at the corresponding evaporation powers P_{em} have been performed using a quartz crystal microbalance (QCM). The central part of the QCM is a quartz crystal, which oscillates at an eigenfrequency of $f_0 = 6\,\mathrm{MHz}$. When a material is deposited onto the quartz crystal's surface, a change in the frequency Δf is recognized with an accuracy of 0.01 Hz, which allows determining the deposited mass Δm of the material using the Sauerbrey equation [186]:

$$\Delta f = -\frac{{f_0}^2}{\rho_{\mathrm{QC}}\, N\, A} \cdot \Delta m \,. \tag{5.1}$$

Here ρ_{QC} is the density of quartz, $N = 1670\,\mathrm{kHz\,mm}$ is the frequency constant for an AT-cut quartz crystal used here [186], and A means the area of the deposited

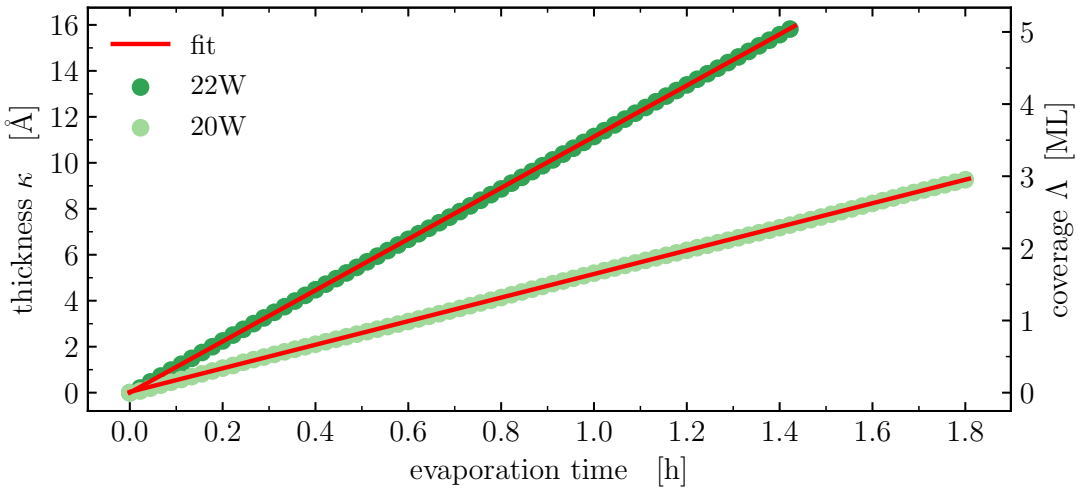

Figure 5.4: Evaporation rates of germanium, measured by QCM, at powers of $P_{\mathrm{em}} = 20\,\mathrm{W}$ and $P_{\mathrm{em}} = 22\,\mathrm{W}$, which were used here for the preparation of thin germanium films.

surface. The film thickness κ can now be obtained from $\kappa = \Delta m \cdot (A \cdot \rho_{\mathrm{mat}})^{-1}$ using the density of the deposition material ρ_{mat}. Since this definition of the layer thickness κ strongly depends on the respective crystal structure of the evaporated material, in this work, the definition of the surface coverage Λ in units of ML is preferred. $\Lambda = 1\,\mathrm{ML}$ is defined as an adsorbate layer with an atomic density equal to those of the Ag(111) substrate's plane [195], as $\rho_{\mathrm{surf}} = 1.384 \times 10^{15}\,\mathrm{cm}^{-2}$. Thus, one can directly receive the coverage of a deposited film from equation (5.1),

$$\Lambda = -\frac{\rho_{\mathrm{QC}}\, N}{{f_0}^2\, M_{\mathrm{mat}}\, \rho_{\mathrm{surf}}} \cdot \Delta f\,, \tag{5.2}$$

with M_{mat} as the atomic mass of the evaporated material.
Figure 5.4 illustrates the measurements of the evaporation rates at two different P_{em} used here for the preparation of the germanene phases. A well manageable and reproducible preparation of defined layer thicknesses can be concluded, which is owed to the steady linear increase of the deposited thickness, as indicated in figure 5.4. The corresponding evaporation rates result from the slopes of the respective linear regressions, which can be determined as $5.1\,\text{Å/h} \approx 1.6\,\mathrm{ML/h}$ for $P_{\mathrm{em}} = 20\,\mathrm{W}$ and $11.1\,\text{Å/h} \approx 3.6\,\mathrm{ML/h}$ for $P_{\mathrm{em}} = 22\,\mathrm{W}$.

In the following, the surface of the clean Ag(111) sample is covered by thin films of germanium. Hereby, the layer thickness was stepwise increased until a change

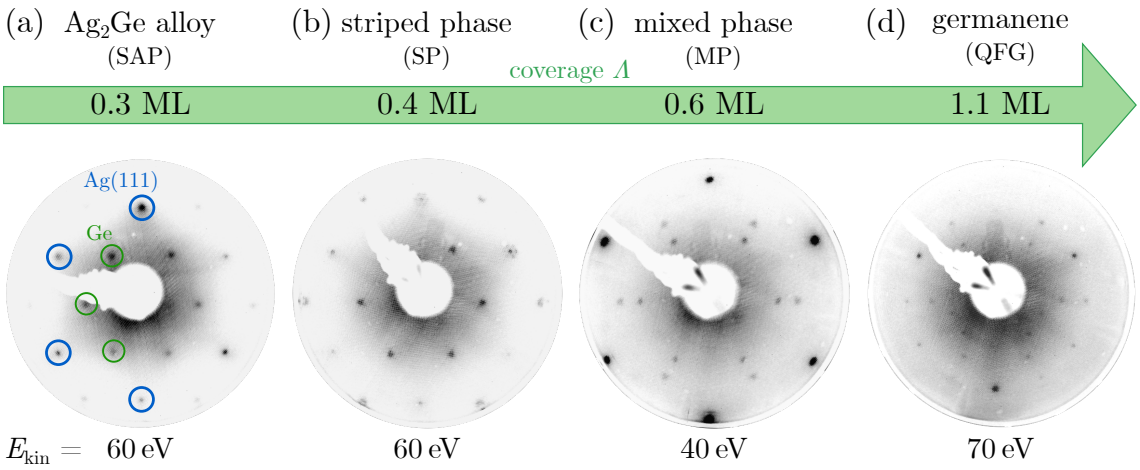

Figure 5.5: LEED patterns of germanium formation at different coverages Λ within the structural evolution of germanene on Ag(111). Figure reproduced from [196].

of the LEED pattern was observed. By this procedure, four distinguishable Ge phases at different coverages were found, as presented in figure 5.5. Since no periodic superstructure of a germanium formation could be identified for low coverages, the first germanium phase was determined at a coverage of $\Lambda = 1/3\,\mathrm{ML}$. This Ag_2Ge surface alloy phase (SAP) forms a $\left(\sqrt{3} \times \sqrt{3}\right)\mathrm{R30}^\circ$ reconstruction [56, 57], which can be recognized in figure 5.5(a). At a slightly increased coverage of $\Lambda = 0.4\,\mathrm{ML}$, a further phase is formed, called the striped phase (SP) [63], which is for example, indicated by appearing satellite spots around the Ag(111) substrate spots. The

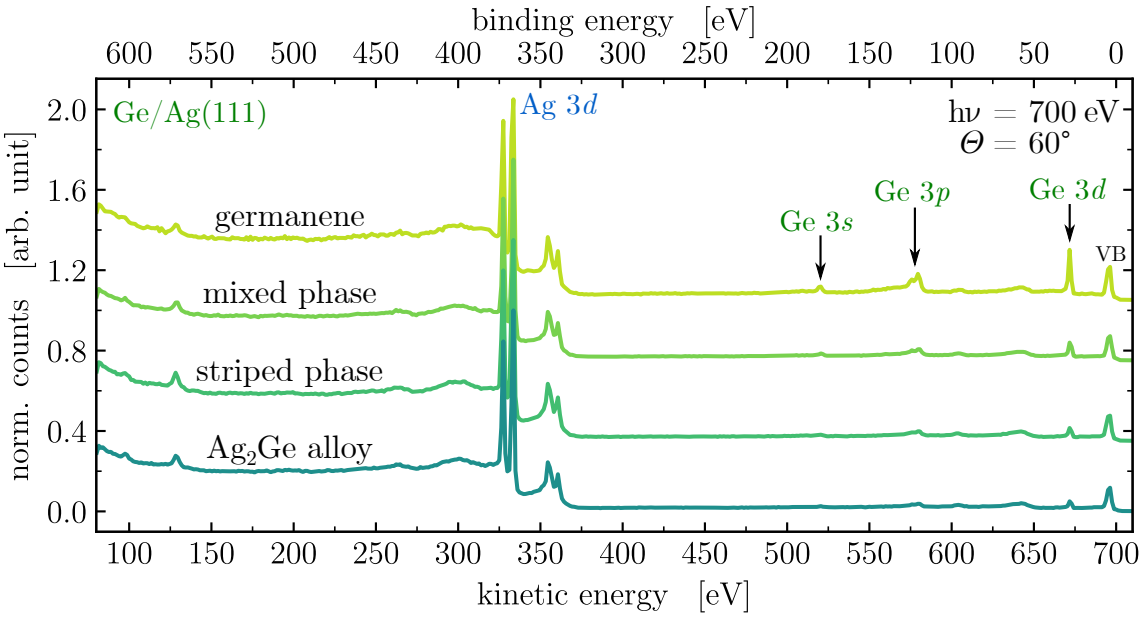

Figure 5.6: XPS survey spectra of all Ge phases formed within the structural evolution of germanene on Ag(111). The spectra are arranged according to their coverage Λ increasing from bottom to top. Figure reproduced from [196].

following evolution stage of germanene is represented by a mixed phase (MP), depicted in figure 5.5(c). Its LEED pattern displays a superposition of the $\left(\sqrt{3} \times \sqrt{3}\right)$ alloy reconstruction and the quasi-freestanding germanene phase (QFG), which is formed at a coverage of $\Lambda = 1.06\,\mathrm{ML}$ [63]. A more detailed analysis of the LEED patterns presented is provided in the respective sections of chapter 6.

Figure 5.6 illustrates the chemical analysis of the germanium phases found in terms of recorded XPS survey spectra. The spectra were recorded at a photon energy of $h\nu = 700\,\mathrm{eV}$ and under an emission angle of $\Theta = 60^\circ$ to achieve a high detection sensitivity for elements located at the surface. Compared to figures 5.1 and 5.2,

arising core level features can be noted, which are attributed to elastic XPS lines of germanium. Paying special attention to the Ge $3d$ signal at $E_{\mathrm{kin}}(\mathrm{Ge}\,3d) = 671.7\,\mathrm{eV}$ and $E_{\mathrm{bin}}(\mathrm{Ge}\,3d) = 28.9\,\mathrm{eV}$, respectively, an obvious increase of its intensity correlated to the germanium amount through all phases from bottom to top can be determined. Additionally, all phases can be characterized as free of contamination, which results from missing core level features of common residual elements, like O and C, at the expected energy positions $E_{\mathrm{bin}}(\mathrm{O}\,1s) = 528.6\,\mathrm{eV}$ and $E_{\mathrm{bin}}(\mathrm{C}\,1s) = 284.3\,\mathrm{eV}$, respectively.
In the following chapter 6, a detailed structural analysis of each germanium formation within the structural evolution towards germanene is presented.

Chapter 6

Results and Discussion

The following chapter presents the analysis results of the chemical and atomic structure of each germanium phase prepared within the structural evolution of germanene on Ag(111). Taking advantage of the powerful surface analysis tools, namely XPS and XPD, with high energy resolution, a particular focus was set on revealing the interface structure of each germanium phase formed. Its surface properties are first investigated starting from the successful preparation of a clean Ag(111) sample. As presented in section 5.2, various germanium phases of different coverages Λ were epitaxially grown on the Ag(111) surface. Each germanium phase is analyzed concerning its structure formed on the substrate and put into context of the structural evolution towards germanene as the final phase. A principal sketch of the sample system is visualized in figure 6.1. Eventually, one particular phase, the Ag_2Ge surface alloy phase, was chosen to be encapsulated by an isolating capping layer of Al_2O_3. Concerning applications as electronic device, the structural arrangement of the SAP before and after the capping is analyzed, and its results are presented in the final section 6.6.

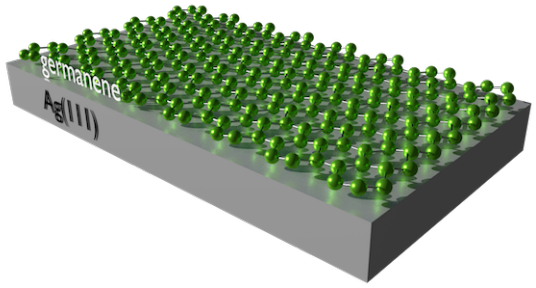

Figure 6.1: Principle illustration of a sample system consisting of germanene on Ag(111).

The principle part of the results presented below has already been published in the article *Tracing the structural evolution of quasi-freestanding germanene on Ag(111)* in Scientific Reports **12**, 7559 (2022) [196].

6.1 Reconstructed Ag(111)

The successfully prepared Ag(111) surface was already proven to be chemically clean and long-range ordered in a (1×1) reconstruction, as discussed in section 5.1. Digging deeper into the structural analysis of the Ag(111) surface, HighRes XPS spectra reveal more detailed and precise information about the surface. Figure 6.2 displays HighRes XPS spectra of the Ag $4d$ region, located at a binding energy of $E_{\mathrm{bin}}(\mathrm{Ag}\,4d_{5/2}) = 4.46\,\mathrm{eV}$, which was recorded at the minimum photon energy of BL11 $\mathrm{h}\nu = 52.5\,\mathrm{eV}$, under normal emission $\Theta = 0°$. *HighRes* XPS spectra owe their term to their high energy resolution, which is obtained in this work by a small step width of $\Delta E = 0.04\,\mathrm{eV}$ in combination with a low pass energy of $E_{\mathrm{pass}} = 5.85\,\mathrm{eV}$. Besides the $4d$ signal, further features within the VB structure can be recognized and associated with direct transitions from the d-bands [197]. The spectrum depicted in figure 6.2 additionally reveals a Shockley surface state at a binding energy of $E_{\mathrm{bin}} = 0.13\,\mathrm{eV}$ [57, 198]. Surface states originate from electron states created by breaking the translation symmetry at the surface, whose features in ARPES measurements can only be observed at nearly normal emission [199]. Moreover, these features only appear for well-ordered and chemically pure surfaces, so signatures of surface states serve conveniently as indicators for a well-prepared surface [198].

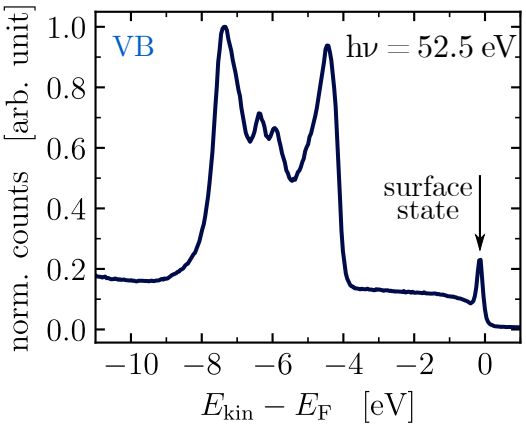

Figure 6.2: HighRes XPS spectrum of the VB region including the Ag $4d$ signal of the clean Ag(111) sample.

Figure 6.3 shows HighRes XPS spectra of the Ag $3d$ core level signal of the clean Ag(111) sample, which were measured under two different emission angles of $\Theta = 0°$ and $\Theta = 60°$. The photon energy for photoexcitation was chosen to be $\mathrm{h}\nu = 480\,\mathrm{eV}$, which meets the intersection of a sufficiently high photon flux of the beamline and cross-section of the respective core level, as well as adequate kinetic energy of the photoelectrons. The $3d$ core level signals were detected at kinetic energies of $E_{\mathrm{kin}}(\mathrm{Ag}\,3d_{5/2}) = 107.61\,\mathrm{eV}$ and $E_{\mathrm{kin}}(\mathrm{Ag}\,3d_{3/2}) = 101.61\,\mathrm{eV}$, which approximately

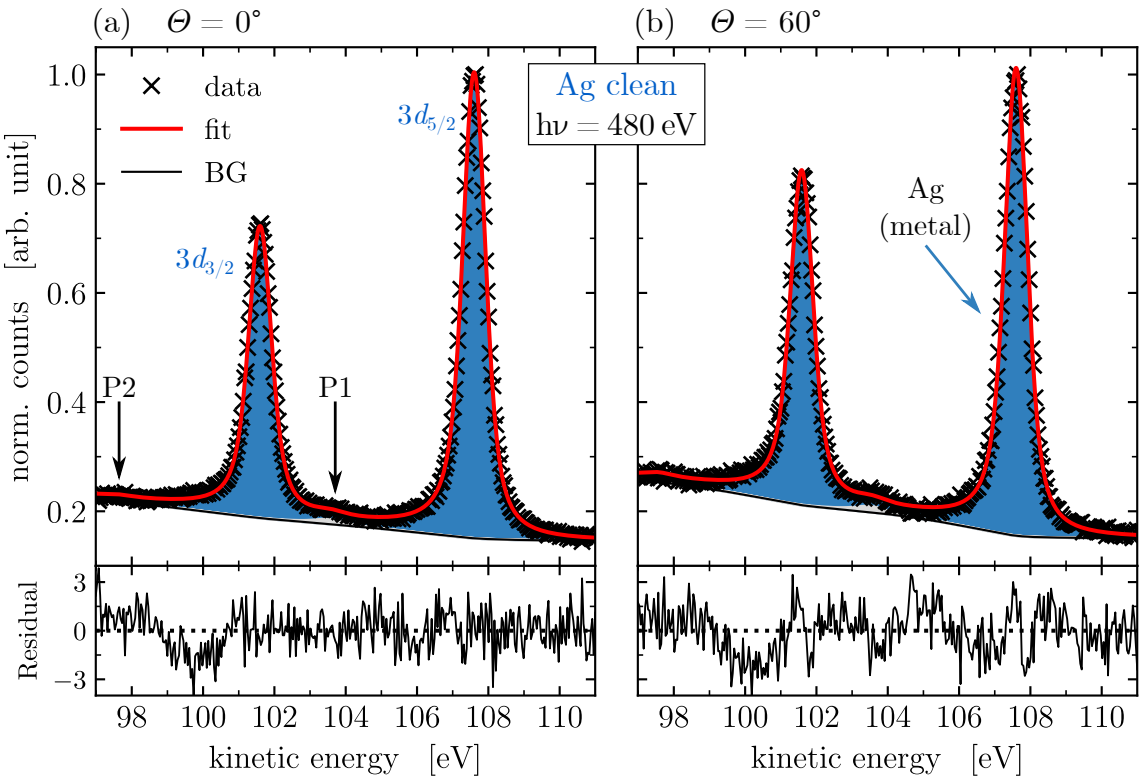

Figure 6.3: XPS HighRes spectra of the Ag 3*d* core level of the clean Ag(111) sample. The spectra were recorded at $h\nu = 480\,\text{eV}$, under emission angles of (a) $\Theta = 0°$ and (b) $\Theta = 60°$.

correspond to a theoretically proposed IMFP of $\lambda = 5.3\,\text{Å}$ [133]. Concerning figure 3.5 from section 3.1.4, the EED is roughly equal to the IMFP. It means that the major contribution of the signal[1] displayed in figure 6.3 originates from the first two layers of the Ag(111) surface, using a mean spacing of $d_z = 2.36\,\text{Å}$ [68]. The 3*d* signal of the clean Ag(111) sample is fitted with only one Voigt-like component, which can be attributed to common metallic Ag bonds, since no surface and bulk components were reported for silver samples. However, the metallic Ag component reveals a slightly asymmetric shape of $\alpha = 0.02$, which is exceptionally small for metals but is also known for noble metals due to its filled *d*-orbital and thus a poor density of states below the Fermi level [158]. The spin-orbit separation between the $3d_{3/2}$ and the $3d_{5/2}$ peak resulting from peak fitting measures $E_{\text{SOC}} = 6.00\,\text{eV}$, which is listed together with further fitting parameters in table 6.1. Additionally,

[1] The rough estimation of IMFP ≈ EED is only valid for XPS measurements at normal emission (see figure 3.5). For higher emission angle measurements, the EED is smaller than the IMFP.

Table 6.1: Fit parameters obtained from the XPS analysis of the Ag 3d HighRes spectra of clean Ag in figure 6.3. All parameters refer to the $3d_{5/2}$ peak.

Fig. 6.3	Θ [°]	comp.	E_{kin} [eV]	E_{SOC} [eV]	FWHM [eV]	α	A_{rel} [%]
(a)	0	Ag	107.61	6.00	0.78	0.02	98.7
		P1	103.56		1.13	0.00	0.9
		P2	97.55		1.12	0.00	0.4
(b)	60	Ag	107.61	6.00	0.78	0.02	98.1
		P1	103.56		1.13	0.00	1.1
		P2	97.55		1.12	0.00	0.8

features of surface plasmons P1 and P2 can be identified in the spectra detected at $E_{\mathrm{kin}}(P1) = 103.56\,\mathrm{eV}$ and $E_{\mathrm{kin}}(P2) = 97.55\,\mathrm{eV}$. A significant increase in their respective intensities from $\Theta = 0°$ to $\Theta = 60°$ measurements by 20 % and 100 %, respectively, can be determined, which is indicated by the change in the corresponding relative area A_{rel}. Thus, the plasmon features can consequently be assigned as surface plasmons [200]. The surface plasmons P1 and P2 represent quasiparticles of collective electron oscillations at the surface, which correspond to the Ag $3d_{3/2}$ and Ag $3d_{5/2}$ peak, respectively [201], with a relative energy shift of $\Delta E_{\mathrm{kin}} = 4.05\,\mathrm{eV}$ and $\Delta E_{\mathrm{kin}} = 4.06\,\mathrm{eV}$. Moreover, surface plasmons only arise from clean surfaces [142], which again emphasizes the thoroughly carried out surface preparation procedure.

In addition to the XPS analysis, XPD measurements of the clean Ag(111) surface were performed. The experimentally obtained XPD pattern of the Ag 3d core level is shown in figure 6.4. The pattern was recorded over a polar angle range of $2° \leq \Theta \leq 58°$, with a lower energy resolution than the regular HighRes of $E_{\mathrm{pass}} = 58.55\,\mathrm{eV}$ to keep the measuring time short. An excitation energy of $\mathrm{h}\nu = 440\,\mathrm{eV}$ was used, which results in a kinetic energy of the Ag emitter atoms of $E_{\mathrm{kin}}(\mathrm{Ag}\,3d_{5/2}) = 73.5\,\mathrm{eV}$. The corresponding simulation of an atom cluster containing $N = 637$ atoms was conducted using respective input parameters for *EDAC*, such as an inner potential of $V_0 = 10.0\,\mathrm{eV}$, an angular momentum cutoff of $l_{\mathrm{max}} = 12$, and the Debye temperature of silver $T_{\mathrm{D}} = 215\,\mathrm{K}$. Taking the IMFP into account, a scattering radius of $r_{\mathrm{scat}} = 7.0\,\text{Å}$ was chosen to execute the simulation to a maximum recursion order of 16.

The best matching XPD simulation is illustrated in figure 6.4(b), which results in an R-factor of $R = 0.15$ corresponding to the experimental pattern, shown in fig-

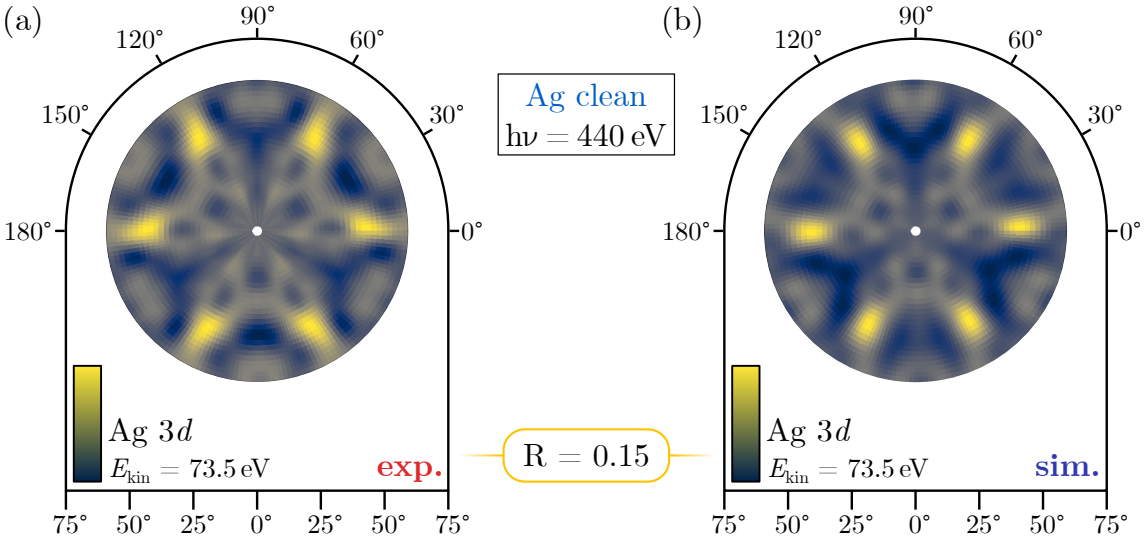

Figure 6.4: (a) Experimental and (b) simulated XPD pattern of the Ag $3d$ core level with $E_{kin}(\mathrm{Ag}\,3d_{5/2}) = 73.5\,\mathrm{eV}$ of the clean Ag(111) sample. The good agreement between (a) and (b) is indicated by an R-factor of $R = 0.15$.

ure 6.4(a). The obtained structural parameters for the Ag(111) associated structure yields the nearest neighbor distance of $d = 2.84\,\text{Å}$ corresponding to a lattice constant of $a_{\mathrm{Ag}} = 4.03\,\text{Å}$. The spacing was calculated as $d_z = 2.35\,\text{Å}$ with a surface relaxation of the two uppermost surface layers of 2 % each. The obtained results for the structure of a clean Ag(111) surface are in excellent agreement with literature values [68, 202], considering a respective deviation of 1 %, which is within the tolerance range of the XPD methods [173].

6.2 Ag_2Ge Surface Alloy

Gradual coverage of the cleaned Ag(111) surface with germanium in increasing layer thicknesses leads to a first forming Ge superstructure at a coverage of $\Lambda = 1/3\,\mathrm{ML}$. Various studies reported similar observations of this formation, called the Ag_2Ge surface alloy phase (SAP) [42, 43, 57–61, 64]. The corresponding LEED pattern measured at a kinetic energy of $E_{kin} = 62.5\,\mathrm{eV}$ is provided in figure 6.5(b). A simulation of the Ge superstructure obtained by *LEEDpat* is added to the right half of the pattern in the shape of blue and green circles for the Ag and the Ge contributions, respectively. The LEED pattern reveals a $(\sqrt{3} \times \sqrt{3})\mathrm{R}30°$ reconstruction in Wood

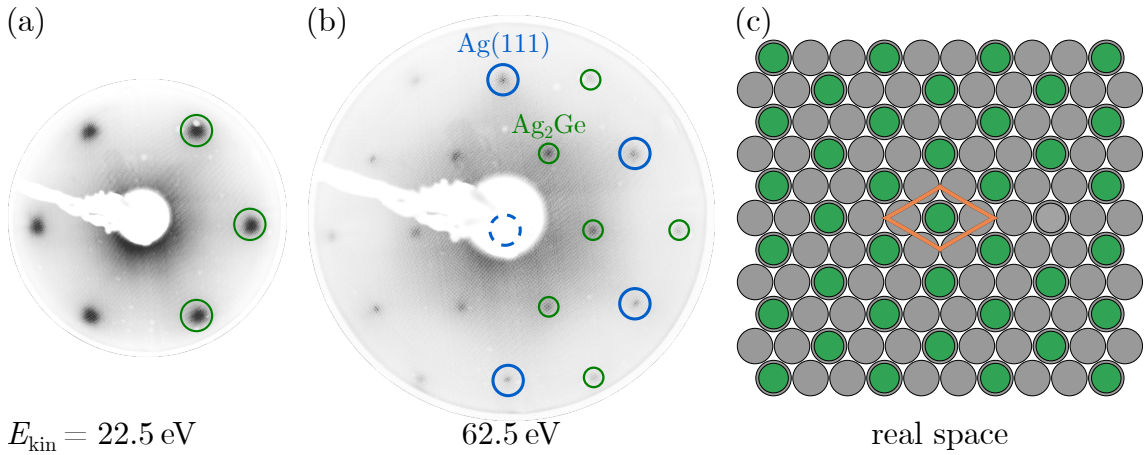

Figure 6.5: LEED patterns of the Ag_2Ge surface alloy phase at a coverage of $\Lambda = 1/3\,ML$. The patterns were recorded at (a) $E_{kin} = 22.5\,eV$ and (b) $E_{kin} = 62.5\,eV$. The corresponding real space illustration (c) was produced by *LEEDpat*.

notation, which is the most stable superstructure for low-dimensional layers on a (111) face [203]. The corresponding matrix expression is $\left(\begin{smallmatrix} 1 & 1 \\ -1 & 2 \end{smallmatrix}\right)$. Its real space periodicity is illustrated in figure 6.5(c), where the grey-filled circles represent the Ag atoms of the surface and the green-filled circles stand for the germanium base. The orange rhombus indicates the unit cell of the superstructure. Figure 6.5(a) depicts a LEED pattern of the SAP obtained at $E_{kin} = 22.5\,eV$, which displays a close-up of the 1. BZ of the Ge superstructure while concurrently demonstrating high-intensity spots and low background noise. The yielded well-defined diffraction pattern at low kinetic energies also indicates a long-range order of the $(\sqrt{3} \times \sqrt{3})R30°$ Ge reconstruction.

Figure 6.6 displays XPS HighRes spectra of the Ge 3*d* core level obtained for the Ag_2Ge phase. The photon energy was selected with $h\nu = 140\,eV$, which combines the maximum photoelectron yield owed to the corresponding cross-section of the Ge 3*d* orbital as discussed in figure 3.3 and the maximum brilliance of the synchrotron radiation of BL11 mentioned earlier in figure 4.9. The experimental XPS data of the Ge 3*d* signal were fitted by two components of a DS profile with an asymmetry parameter of $\alpha = 0.13$ each. The Ge $3d_{3/2}$ and $3d_{5/2}$ peaks are determined at kinetic energies of $E_{kin}(Ge\,3d_{3/2}) = 106.89\,eV$ and $E_{kin}(Ge\,3d_{5/2}) = 107.45\,eV$, which yields a spin-orbit separation for the Ge 3*d* signal of $E_{SOC} = 0.56\,eV$. The kinetic energy of the Ge 3*d* photoelectrons provides them an IMFP of $\lambda = 5.2\,Å$ [133], which

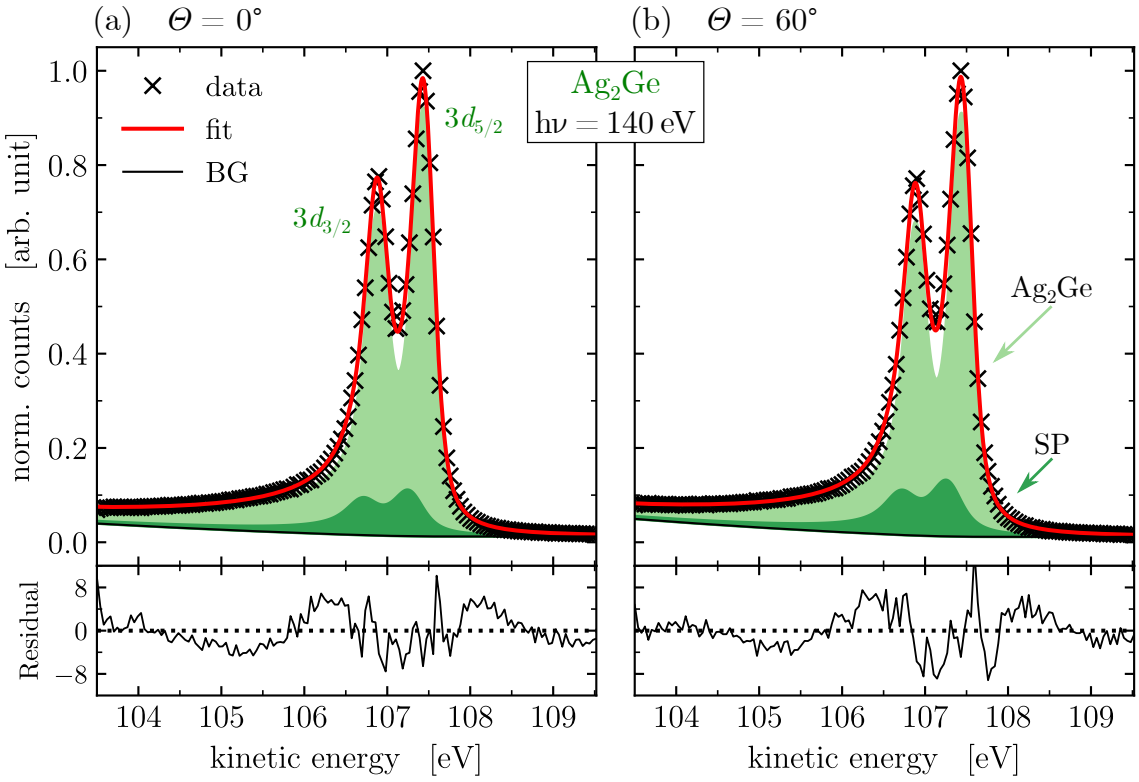

Figure 6.6: XPS HighRes spectra of the Ge 3*d* core level of the Ag_2Ge surface alloy at the coverage of $\Lambda = 1/3$ ML. The spectra were recorded at $h\nu = 140$ eV, under emission angles of (a) $\Theta = 0°$ and (b) $\Theta = 60°$.

classifies the measurements as very surface sensitive. All fit parameters are given in table 6.2. Since the Ge 3*d* HighRes spectra reveal the internal structure of the surface alloy formation, the spectra are dominated by the light green component, which can be assigned to an expected Ag_2Ge alloy component interacting with the Ag atoms of the surface. A second component is recovered chemically shifted by

Table 6.2: Fit parameters obtained from the XPS analysis of the Ge 3*d* HighRes spectra of the Ag_2Ge surface alloy in figure 6.6. All parameters refer to the $3d_{5/2}$ peak.

Fig. 6.6	Θ [°]	comp.	E_{kin} [eV]	E_{SOC} [eV]	FWHM [eV]	α	A_{rel} [%]
(a)	0	Ag_2Ge	107.45	0.56	0.33	0.13	86.7
		SP	107.28	0.56	0.50	0.13	13.3
(b)	60	Ag_2Ge	107.46	0.56	0.33	0.13	84.0
		SP	107.29	0.56	0.50	0.13	16.0

$E_{\text{chem}} = 0.17\,\text{eV}$ towards lower kinetic energies. The SP component was observed to increase for slightly higher coverages, so it can already be attributed to the following striped phase [57, 204]. At an emission angle of $\Theta = 60°$, shown in figure 6.6(b), the intensity increases significantly by 20 %, which indicates a near-surface arrangement compared to the atoms of the Ag_2Ge component. Moreover, a broader FWHM of the SP component than the Ag_2Ge component can be noted, which is in good agreement with the peak shapes of the SP observed. However, the low FWHM of the Ag_2Ge component of 0.33 eV and the significant asymmetry indicates a highly ordered atomic structure and metal-like VB structure [158], respectively. Thus, the structure model of a surface alloy consisting of embedded Ge atoms interacting with the first layer of the silver surface is assumed by the obtained results. Raman investigations of the surface alloy also revealed the metallic nature of the Ge formation which is in good accordance with the results presented here [59].

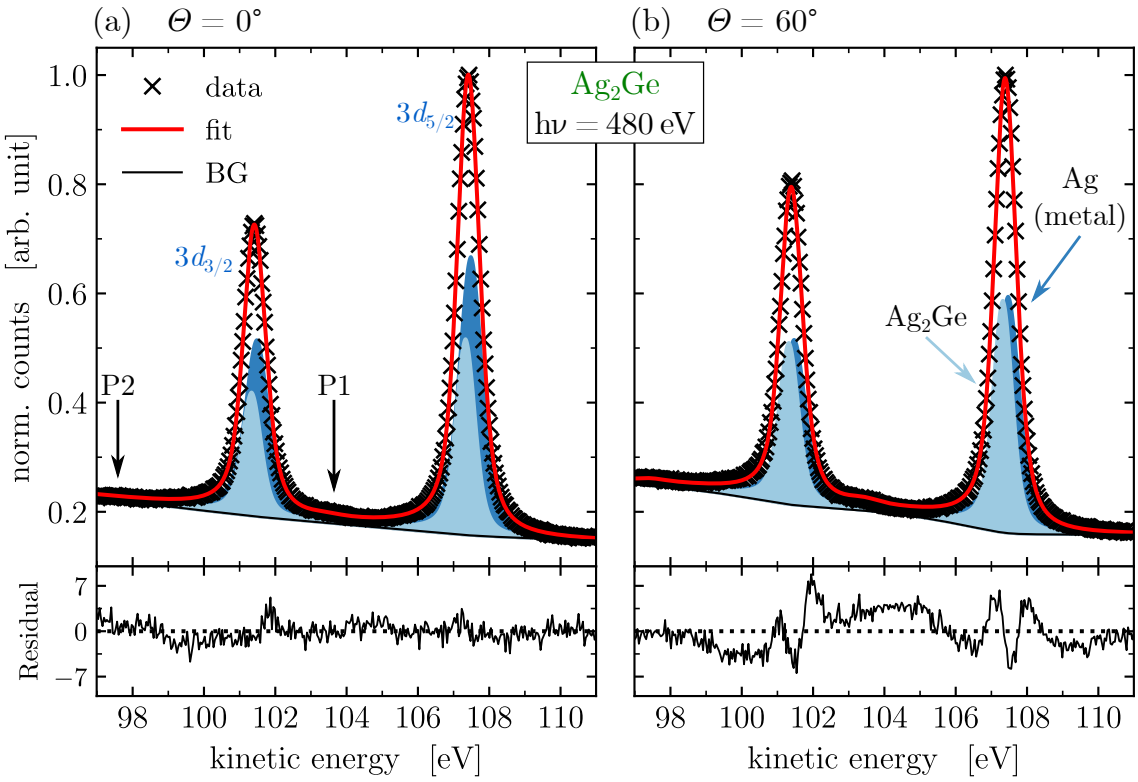

Figure 6.7: XPS HighRes spectra of the Ag 3*d* core level of the Ag_2Ge surface alloy at the coverage of $\Lambda = 1/3$ ML. The spectra were recorded at $h\nu = 480$ eV, under emission angles of (a) $\Theta = 0°$ and (b) $\Theta = 60°$.

Table 6.3: Fit parameters obtained from the XPS analysis of the Ag 3*d* HighRes spectra of the Ag_2Ge surface alloy in figure 6.7. All parameters refer to the $3d_{5/2}$ peak.

Fig. 6.7	Θ [°]	comp.	E_{kin} [eV]	E_{SOC} [eV]	FWHM [eV]	α	A_{rel} [%]
(a)	0	Ag	107.50	6.00	0.78	0.02	63.1
		Ag_2Ge	107.34	6.00	0.67	0.02	36.4
		P1	103.44		1.10	0.00	0.4
		P2	97.44		1.11	0.00	0.0
(b)	60	Ag	107.48	6.00	0.78	0.02	54.6
		Ag_2Ge	107.32	6.00	0.67	0.02	43.9
		P1	103.42		1.10	0.00	0.9
		P2	97.42		1.11	0.00	0.5

Figure 6.7 displays the spectra of the Ag 3*d* core level obtained for the Ag_2Ge surface alloy phase. Consequently, it represents the counterpart of contributing Ag atoms to the surface alloy, allowing a complete examination of the interface structure. Hence, the spectra reveal two chemically shifted components by $E_{chem} = 0.15\,eV$, which can be attributed to the metallic Ag bonds, as comparable to figure 6.3 and Ag_2Ge alloy bonds. These results support the proposed structure model of a highly ordered surface alloy phase since even remaining signals of surface plasmons were identified, mentioned in table 6.3, containing all fit parameters. The total intensity of the signal obtained for normal emission, depicted in figure 6.7(a), can be decomposed into 2/3 claimed by the metallic Ag component and 1/3 corresponding to the Ag_2Ge component. This result agrees very well with the structure model, considering the previously discussed EED of approximately 2 to 3 contributing crystal layers. Similarly to the ARXPS analysis for the Ge 3*d* core level in figure 6.6, the relative areas A_{rel} and intensities of the components, respectively, change for recorded spectra under high emission angles by +21 % for the Ag_2Ge and −30 % for the metallic Ag component. Also in this case, the ARXPS measurements illustrate the Ag_2Ge as the surface component and the metallic Ag as the bulk component.

In order to finally determine the formed structure of the surface alloy phase at a coverage of $\Lambda = 1/3\,ML$, XPD measurements of the Ge 3*d* core level were performed, presented in figure 6.8(a). The diffraction pattern was obtained at a photon energy of $h\nu = 140\,eV$ leading to a kinetic energy of the respective photoelectrons of $E_{kin} = 107.5\,eV$ and was recorded over a polar angle range of $2° \leq \Theta \leq 72°$. The

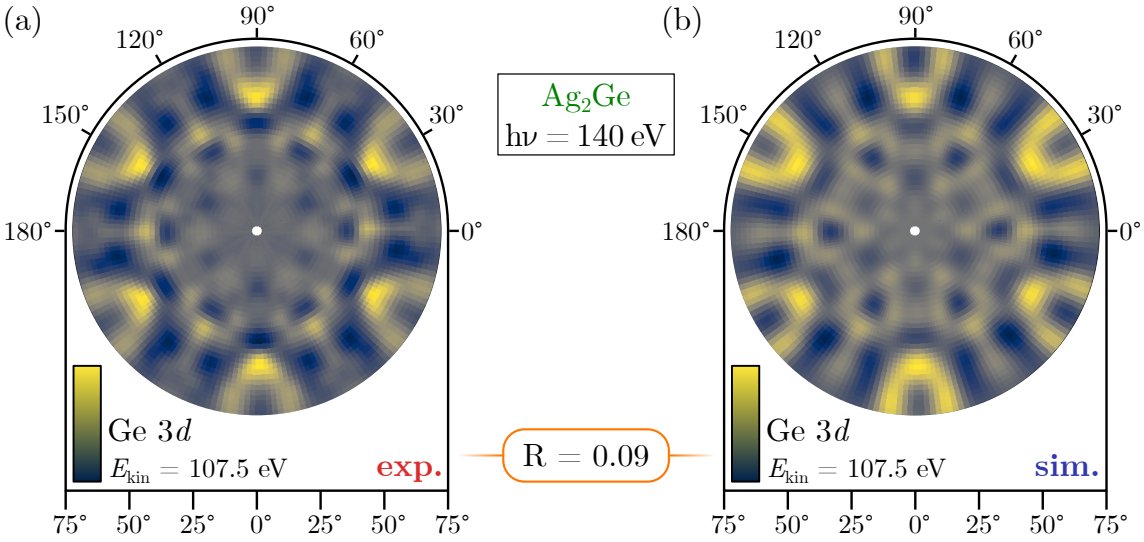

Figure 6.8: (a) Experimental and (b) simulated XPD pattern of the Ge $3d$ core level with $E_{\mathrm{kin}}(\mathrm{Ge}\,3d_{5/2}) = 107.5\,\mathrm{eV}$ of the Ag_2Ge surface alloy. An excellent agreement between (a) and (b) is indicated by the minimum R-factor of $R = 0.09$.

corresponding simulated XPD pattern is displayed in figure 6.8(b). In this case, an atomic cluster consisting of $N = 778$ atoms was simulated by *EDAC* up to an order of 16, using a scattering radius of $r_{\mathrm{scat}} = 8.5\,\text{Å}$. Further input parameters were chosen as an inner potential of $V_0 = 14.3\,\mathrm{eV}$ for germanium, an agular momentum cutoff of $l_{\mathrm{max}} = 12$, and the Debye temperature for germanium of $T_{\mathrm{D}} = 374\,\mathrm{K}$. Initially, a structural model of a surface alloy was assumed, which consists of Ge atoms em-

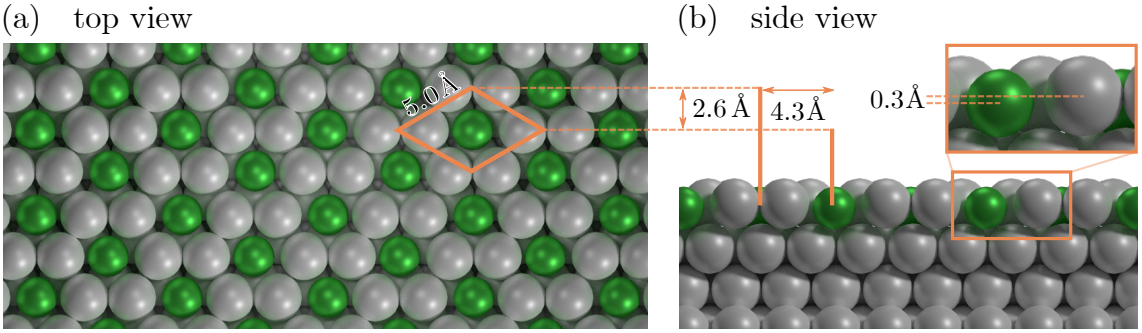

Figure 6.9: Best matching test structure for the Ag_2Ge surface alloy phase corresponding to the simulated XPD pattern in figure 6.8(b). The structure model satisfies the $(\sqrt{3} \times \sqrt{3})\mathrm{R}30°$ periodicity, as indicated by the unit cell highlighted in orange. Figure reproduced from [196].

bedded into the silver surface. The resulting formation satisfies the $(\sqrt{3} \times \sqrt{3})$R30° superstructure obtained by LEED and also meets similar structure proposes in literature [58, 59]. Eventually, the genetic algorithm delivered a specific structure model of the best matching test structure, which is depicted in figure 6.9. The corresponding calculated XPD pattern in figure 6.8(b) agrees excellently to the experimentally yielded pattern, which is demonstrated by the low R-factor of R = 0.09.

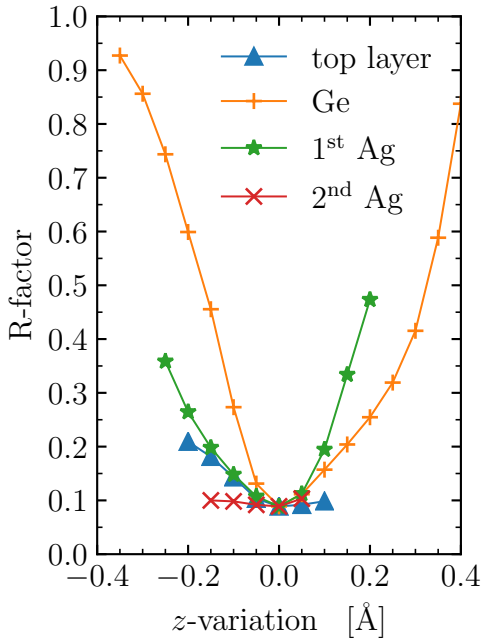

Figure 6.10: z-variation of certain atomic groups respective the best matching structure to prove its R-factor of R = 0.09 to be a minimum.

The minimum of the R-factor was additionally checked by applying small translations of particular atomic groups in z-direction, normal to the surface. Spacing variations of the entire uppermost (top) layer, only the embedded Ge atoms, as well as relaxations of the first and second pure Ag layer, were performed, and diffraction patterns of the obtained test structures were simulated. The resulting R-factors are displayed in figure 6.10. Here, the z-variation means a relative modification with respect to the best matching structure, which illustratively holds the minimum R-factor of R = 0.09. The final structure found for the Ag_2Ge surface alloy phase is illustrated in figure 6.9. The unit cell of the Ge superstructure is highlighted in orange in the top view of figure 6.9(a), which implies a lattice constant of $a_{\mathrm{SAP}} = 5.0\,\text{Å}$. The obtained value is also supported by DFT calculations performed in a similar study on the Ag_2Ge system [58]. Beyond that, an embedding depth of the Ge atoms of 0.3 Å was returned, as demonstrated in a close-up in figure 6.9(b). Even though this value differs from a level surface formation as proposed by the DFT study [58], it indicates the endeavor of the Ge atoms to arrange in an equidistant position with respect to the surrounding Ag atoms.

6.3 Striped Phase

Following the Ge coverage line in figure 5.5, the next formation appears at a coverage of $\Lambda = 0.4\,\mathrm{ML}$, called the striped phase (SP). This one is hard to distinguish from the Ag_2Ge SAP due to its only slightly higher coverage and is often mistaken for it [204]. The striped phase owes its name to a characteristic appearance in STM measurements. Parallel running stripes resulting from a modulation in the measured electron density can be observed [60, 63, 66] with a periodicity of $\sim 6\sqrt{3}$ [59, 204]. It is reported that the SP consists of a compressed SAP along the $[1\bar{1}0]$ direction [62] with a lattice mismatch of 12 % regarding the underlying Ag(111) substrate [63]. Due to a higher density of the SP than the Ag(111), the positions of the Ge atoms undulate between the fcc sites and hcp sites [62], resulting in a striped STM appearance, which is famously known from the $(22 \times \sqrt{3})$-herringbone reconstruction of the Au(111) surface [205].

Figure 6.11(a) and (b) show the characteristic LEED patterns obtained for the SP at different kinetic energies of $E_{\mathrm{kin}} = 22.5\,\mathrm{eV}$ and $E_{\mathrm{kin}} = 50\,\mathrm{eV}$, respectively. At a first glance, these patterns appear no different from the ones of the SAP, revealing a $(\sqrt{3} \times \sqrt{3})\mathrm{R}30°$ reconstruction, as displayed in figure 6.7. By taking a closer look at the substrate's spots and the $\sqrt{3}$-spots, some additional satellite features can

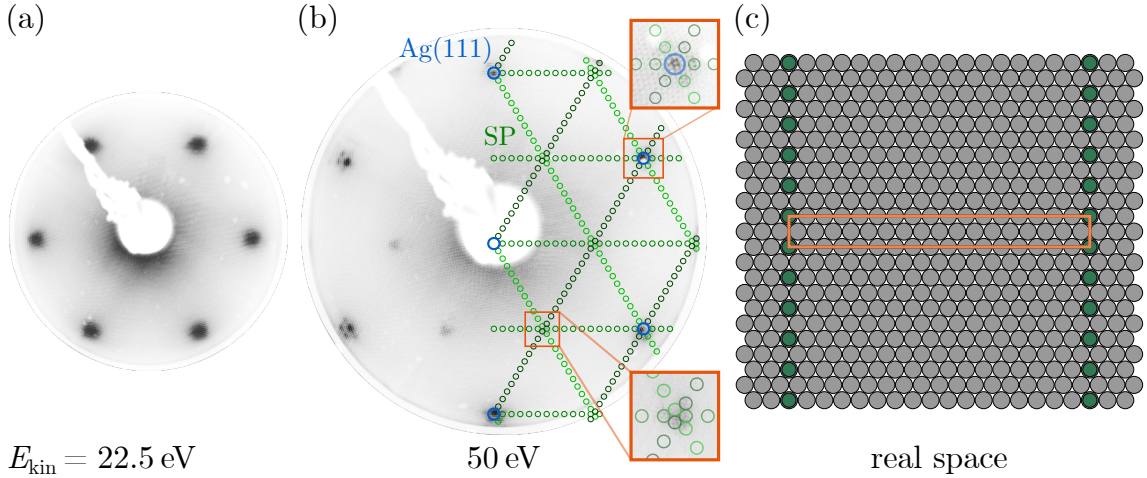

Figure 6.11: LEED patterns of the striped phase at a coverage of $\Lambda = 0.4\,\mathrm{ML}$. The patterns were recorded at (a) $E_{\mathrm{kin}} = 22.5\,\mathrm{eV}$ and (b) $E_{\mathrm{kin}} = 60\,\mathrm{eV}$. The periodicity of the superstructure is provided in the corresponding (c) real space illustration produced by *LEEDpat*.

be recognized, demonstrated by the close-ups in figure 6.11(b). Apparently, the periodicity changed to a larger unit cell of the Ge superstructure compared to the SAP structure, which fits perfectly into the mold with the reports of structural studies mentioned above. Even though many contradictory descriptions of the SP superstructure have confusingly been published [59, 61, 62], here, sufficient modeling of the periodicity returned a rectangular Rec($\sqrt{3}\times 17$) with three domains. Referring to the similar appearance in LEED patterns of the ($22\times\sqrt{3}$) reconstruction of Au(111) [205], the Rec($\sqrt{3}\times 17$) and $\begin{pmatrix} 17 & 0 \\ -1 & 2 \end{pmatrix}$, respectively, successfully serves as an explict characterization of the SP superstructure, as indicated by the *LEEDpat* simulation added to the pattern 6.11(b). The blue circles stand for the Ag(111) substrate, while the circles colored in three different shades of green correspond to the three domains of the SP. Since only the periodicity of the LEED pattern is concerned in the simulation, multiple scattering effects lead to a suppression of several reflection spots, which is why some spots of the simulated pattern cannot be recovered in the experimentally obtained LEED pattern. The corresponding real space visualization is provided in figure 6.11, where the dark green colored lattice sites indicate the periodicity of the superstructure. This structure model is also supported by a combined experimental and theoretical study by Zhang *et al.*, which additionally provides the atomic structure inside the unit cell [62].

Another proof of the conclusive distinction between SAP and SP can be yielded by the analysis of the electronic structure of the SP in the form of XPS HighRes presented in figures 6.12 and 6.13. The Ge 3*d* core level spectra representing the internal structure of the SP are depicted in figure 6.12, already revealing a different peak shape compared to the SAP in figure 6.6. In the SP case, the 3*d* signal consists of 3 DS-like components, namely SP1, SP2, and SP3. The corresponding fit parameters are listed in table 6.4. It can be noted that the SP component from figure 6.6 is split into three, though each has the same FWHM. The increased number of SP components can be explained by the reported tensile strain of the uppermost surface alloy layer, which causes shortened bond lengths [63]. This kind of modification of the Ge atoms' chemical environments leads to emerging components, each representing a particular group of Ge atoms. Concerning the atomic position regarding the Ag substrate, the fully commensurate superstructure of the SAP turned into an enlarged unit cell of the striped phase's superstructure containing Ge atoms in top, hollow, and bridge positions [62]. Moreover, a wavelike height modulation of the SP

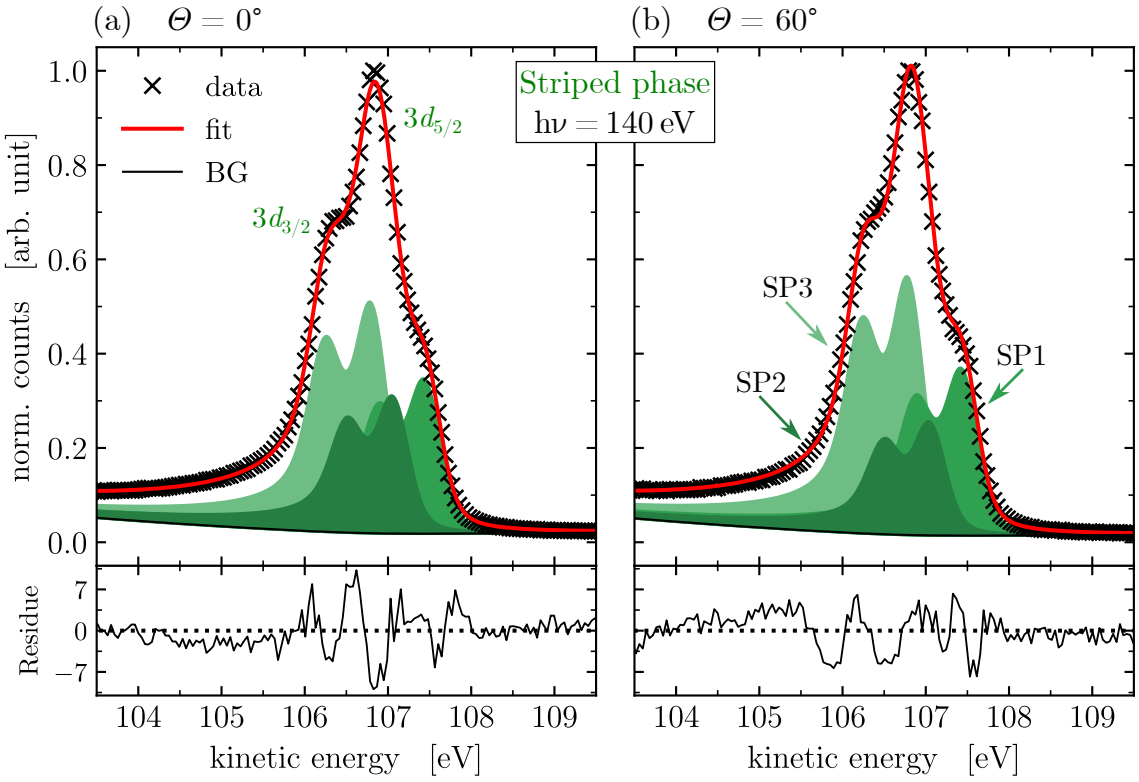

Figure 6.12: XPS HighRes spectra of the Ge 3*d* core level of the striped phase at a coverage of $\Lambda = 0.4\,\mathrm{ML}$. The spectra were recorded at $h\nu = 140\,\mathrm{eV}$, under emission angles of (a) $\Theta = 0°$ and (b) $\Theta = 60°$.

structure by $0.12\,\text{Å} - 0.2\,\text{Å}$ was identified, which likewise allows the assignment of three groups of atoms to different heights [62, 204]. Comparing the spectra 6.12(a) and (b) obtained for different polar angles, a notable increase and decrease of some

Table 6.4: Fit parameters obtained from the XPS analysis of the Ge 3*d* HighRes spectra of the striped phase in figure 6.12. All parameters refer to the $3d_{5/2}$ peak.

Fig. 6.12	Θ [°]	comp.	E_{kin} [eV]	E_{SOC} [eV]	FWHM [eV]	α	A_{rel} [%]
(a)	0	SP1	107.46	0.56	0.50	0.13	29.7
		SP2	107.08	0.56	0.50	0.13	26.3
		SP3	106.82	0.56	0.50	0.13	44.0
(b)	60	SP1	107.45	0.56	0.50	0.13	31.2
		SP2	107.07	0.56	0.50	0.13	21.2
		SP3	106.81	0.56	0.50	0.13	47.7

components' relative areas A_{rel} can be observed. An increase of 5 % and 8 % for the SP1 and SP3 component, respectively, with a concurrent decrease of 20 % of the SP2, allows to attribute the corresponding atomic groups SP1 and SP3 to the surface and SP2 to the interface. An asymmetry parameter of $\alpha > 0.1$ for all components within the alloy phases SAP and SP indicates a metallic character of the Ge formations. This behavior might be a result of a strong electronic influence of the metallic Ag substrate, which is additionally supported by the remarkable contribution of the SP2 interface component to the total signal of the Ge 3*d* core level.
A more detailed view of the interface structure is provided by examining the Ag 3*d* signal, which is depicted in figure 6.13. The corresponding fit parameters can be

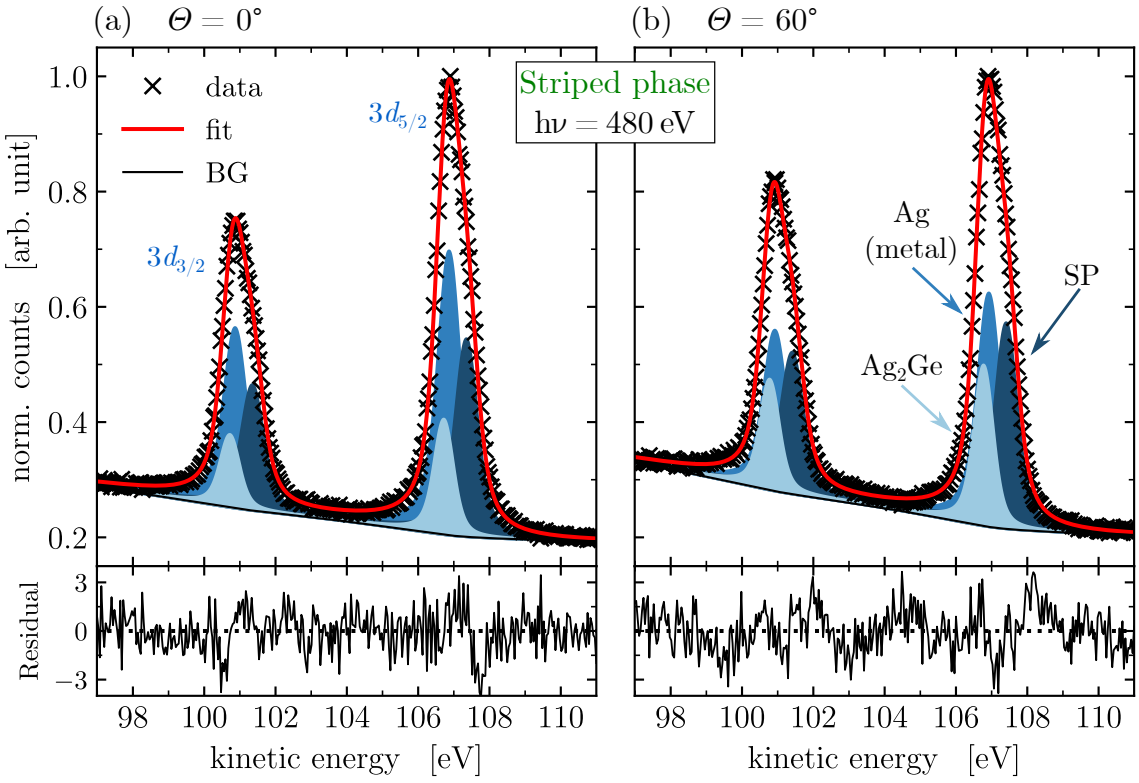

Figure 6.13: XPS HighRes spectra of the Ag 3*d* core level of the striped phase at a coverage of $\Lambda = 0.4$ ML. The spectra were recorded at $h\nu = 480$ eV, under emission angles of (a) $\Theta = 0°$ and (b) $\Theta = 60°$.

found in table 6.5. On the contrary to the Ag 3*d* HighRes spectra obtained for the Ag_2Ge surface alloy phase, here, a further Voigt-like component, called SP component, needs to be added to fit the experimental data. The SP component is chemically shifted by $E_{\mathrm{chem}} = 0.48$ eV towards higher kinetic energies regarding the

Table 6.5: Fit parameters obtained from the XPS analysis of the Ag 3*d* HighRes spectra of the striped phase in figure 6.13. All parameters refer to the $3d_{5/2}$ peak.

Fig. 6.13	Θ [°]	comp.	E_{kin} [eV]	E_{SOC} [eV]	FWHM [eV]	α	A_{rel} [%]
(a)	0	SP	107.36	6.00	0.76	0.02	33.7
		Ag	106.88	6.00	0.78	0.02	49.8
		Ag_2Ge	106.73	6.00	0.67	0.02	16.6
(b)	60	SP	107.41	6.00	0.76	0.02	35.3
		Ag	106.93	6.00	0.78	0.02	41.3
		Ag_2Ge	106.78	6.00	0.67	0.02	23.4

metallic Ag component and shows similar surface effects as the Ag_2Ge component as indicated by an intensity increase of 5 % from $\Theta = 0°$ to $\Theta = 60°$. While not only the Ge atoms are affected by the tensile strain of the alloy layer, also the Ag atoms within the alloy undergo a change of their chemical environments in the SP. This interpretation of the SP structure explains the arising SP component in the XPS HighRes spectra.

Although no XPD measurements have been performed for this phase, it can be concluded that the structure model of the SP proposed by Zhang *et al.* on the basis of SXRD measurements and DFT calculations [62] agrees with the results obtained here. Through a slightly increased coverage, the SAP turns into the SP by a compression of the uppermost alloy layer, which can be determined from the analysis presented here and experimental observations from comparable studies.

6.4 Mixed Phase

The next Ge phase in the series of the structural evolution of germanene is called the mixed phase (MP), which was most clearly observed at a coverage of $\Lambda = 0.6\,\mathrm{ML}$. Firstly observed by Lin *et al.*, this phase consists of a superposition of the SP and the QFG phase. STM imaging revealed large domain sheets of the respective SP and QFG phases bounded by step edges. [63] The obtained LEED patterns for the MP at different kinetic energies are shown in figure 6.14. The simulated reflection spots, added as circles to the experimental patterns, consider the Ag(111) substrate

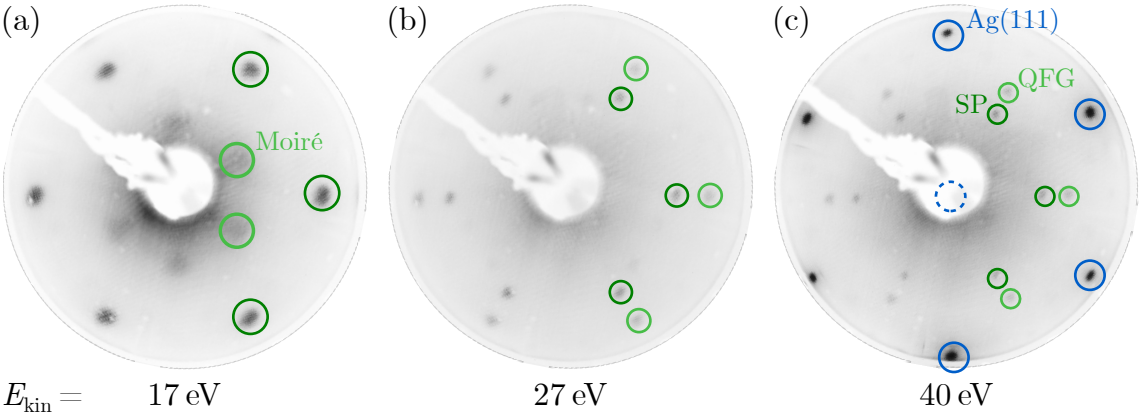

Figure 6.14: LEED patterns of the mixed phase obtained at a coverage of $\Lambda = 0.6\,\mathrm{ML}$. The patterns were recorded at (a) $E_{\mathrm{kin}} = 17\,\mathrm{eV}$, (b) $E_{\mathrm{kin}} = 27\,\mathrm{eV}$, and (c) $E_{\mathrm{kin}} = 40\,\mathrm{eV}$. Here, characteristic reflection spots of the SP and the QFG phase are highlighted in dark and light green, respectively.

spots (blue), the $\sqrt{3}$-spots of the SP (dark green), as well as the most dominant spots and a Moiré pattern of the QFG reconstruction (light green), which will be discussed in detail in section 6.5.

In order to quantitatively identify the corresponding reconstructions of SP and QFG, a method for determining the relative lattice constant of a superstructure with respect to the substrate is applied. Considering the Laue equation for constructive interference combined with the de Broglie wavelength for electron waves (3.31) leads to

$$s = \frac{\mathrm{h}\,R}{a\sqrt{2m_{\mathrm{e}}}} \cdot \frac{1}{\sqrt{E_{\mathrm{kin}}}}\,, \tag{6.1}$$

which describes the correlation to a distance s between reflection spots on the LEED screen with a radius R. Details about the derivation of expression (6.1) can be gathered from Lackinger *et al.* [206]. Thus, the relative distances between the reflection spots and the $(0,0)$-spot normalized to the screen's radius can be plotted against $1/\sqrt{E_{\mathrm{kin}}}$ of the respective kinetic energy. Using a linear regression, the relative lattice constant a_i/a_{Ag} can be extracted from the slope of the regression line. Figure 6.15 displays the analysis method discussed above of LEED patterns obtained for the MP in an energy range of $15\,\mathrm{eV} \leq E_{\mathrm{kin}} \leq 145\,\mathrm{eV}$. Relative lattice constants of $a_{\mathrm{SP}}/a_{\mathrm{Ag}} = 1.67 \pm 0.01$ for the SP and $a_{\mathrm{QFG}}/a_{\mathrm{Ag}} = 1.36 \pm 0.01$ for the QFG were yielded. Consequently, these phases can clearly be identified within the MP LEED pattern since an analogous analysis of LEED pattern obtained of the

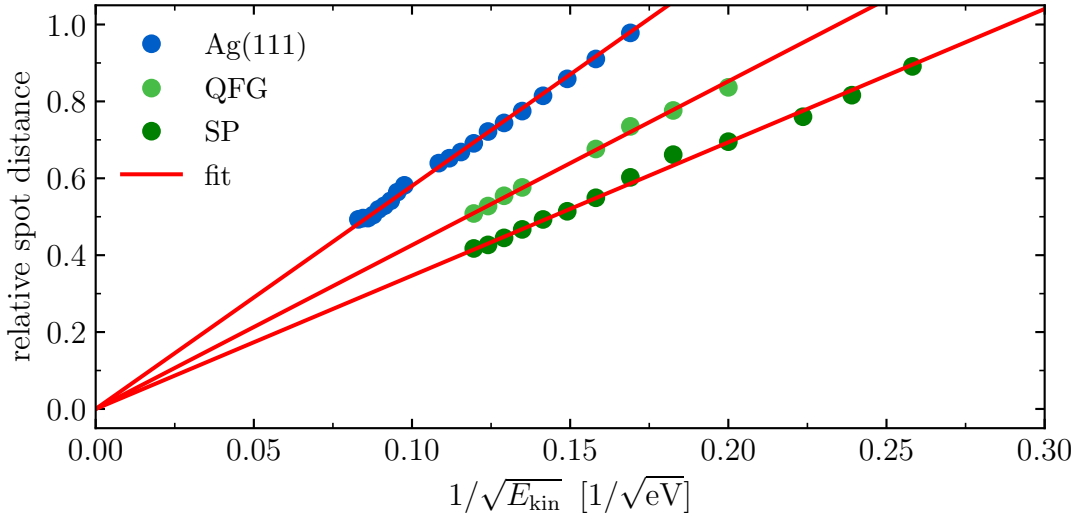

Figure 6.15: Linear regression of the plotted correlation (6.1) to extract the relative lattice constants of the SP and QFG phase from LEED patterns obtained for the MP.

respective isolated phases returned values of $a_{\mathrm{SP}}/a_{\mathrm{Ag}} = 1.70 \pm 0.01 \approx \sqrt{3}$ for the SP and $a_{\mathrm{QFG}}/a_{\mathrm{Ag}} = 1.36 \pm 0.01$ for QFG.

Figures 6.16 and 6.17 present the XPS HighRes spectra of the Ge $3d$ and the Ag $3d$ core level recorded for the mixed phase. As expected for a *mixed* phase, discussed in the LEED paragraph above, the Ge $3d$ core level spectra shown in figure 6.16 reveal two components chemically shifted by $E_{\mathrm{chem}} = 0.16\,\mathrm{eV}$, which can be assigned to the SP and the QFG phase. The relative areas A_{rel} of both components yield a ratio of nearly 1 at normal emission, which can be noticed from the fit parameters provided in table 6.6. It indicates an almost equal amount of contributions from the SP and the QFG phase inside the measuring field, as also observed by Lin *et al.* in STM images [63]. Having a closer look at the components' intensities measured at high emission in figure 6.16(b), a significant decrease and increase in the relative areas of the SP and the QFG component, respectively, can be noted. The SP component's intensity is reduced by 19 %, while the intensity of the QFG rises by 24 %, which mirrors the distribution of both coexisting phases. Due to the intensity increase of the QFG component at $\Theta = 60°$, the germanene phase seems to be closer to the surface than the striped phase. Recalling the structure model of the SAP proposed here and its tensile strain leading to the SP, the Ge atoms are supposed to be embedded in

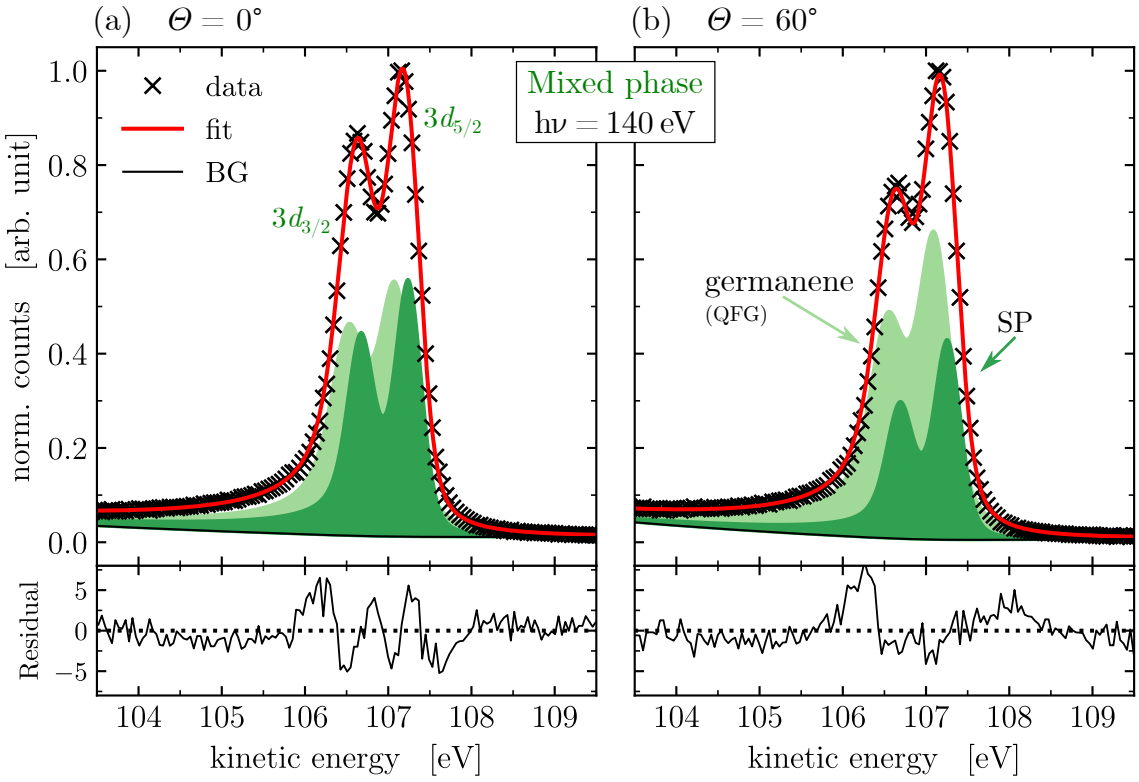

Figure 6.16: XPS HighRes spectra of the Ge 3*d* core level of the mixed phase at a coverage of $\Lambda = 0.6$ ML. The spectra were recorded at $h\nu = 140$ eV, under emission angles of (a) $\Theta = 0°$ and (b) $\Theta = 60°$.

the uppermost alloy layer, while the QFG grows on top of the Ag layer, as will be discussed in section 6.5. Thus, a stacking order of both phases can be reconstructed since contributions to both components originate from the respective emitters located either in the surface layer or on top. Moreover, the observed surface effects of both SP and QFG components in the Ge 3*d* signal match up very well with reports of the

Table 6.6: Fit parameters obtained from the XPS analysis of the Ge 3*d* HighRes spectra of the mixed phase in figure 6.16. All parameters refer to the $3d_{5/2}$ peak.

Fig. 6.16	Θ [°]	comp.	E_{kin} [eV]	E_{SOC} [eV]	FWHM [eV]	α	A_{rel} [%]
(a)	0	SP	107.26	0.57	0.40	0.08	43.7
		QFG	107.10	0.57	0.51	0.08	56.4
(b)	60	SP	107.27	0.57	0.40	0.08	33.1
		QFG	107.12	0.57	0.51	0.08	66.9

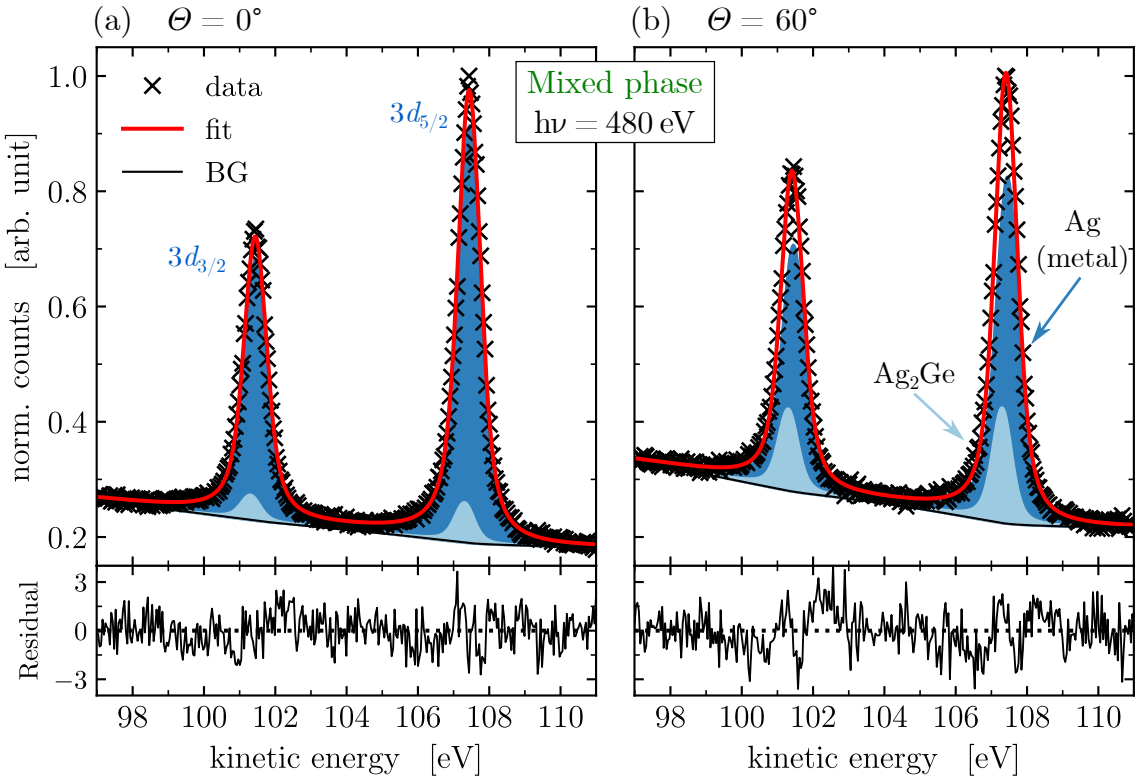

Figure 6.17: XPS HighRes spectra of the Ag 3*d* core level of the mixed phase at a coverage of $\Lambda = 0.6$ ML. The spectra were recorded at $h\nu = 480$ eV, under emission angles of (a) $\Theta = 0°$ and (b) $\Theta = 60°$.

QFG mainly growing from upper step edges [63].

Turning to figure 6.17, the Ag 3*d* core level signal of the MP germanium formation is depicted. The spectra exhibited conform quite much to the shape of the Ag 3*d* signal obtained for the SAP, displayed in figure 6.7. Not least because of the same chemical shift, the spectra reveal the same components as already identified in the

Table 6.7: Fit parameters obtained from the XPS analysis of the Ag 3*d* HighRes spectra of the mixed phase in figure 6.17. All parameters refer to the $3d_{5/2}$ peak.

Fig. 6.17	Θ [°]	comp.	E_{kin} [eV]	E_{SOC} [eV]	FWHM [eV]	α	A_{rel} [%]
(a)	0	Ag	107.46	6.00	0.78	0.02	92.7
		Ag_2Ge	107.31	6.00	0.67	0.02	7.3
(b)	60	Ag	107.46	6.00	0.78	0.02	78.6
		Ag_2Ge	107.31	6.00	0.67	0.02	21.4

case of the SAP. Here, the best fit was achieved with two Voigt-like components that are chemically shifted by $E_{\text{chem}} = 0.15\,\text{eV}$, each with the slight asymmetry of $\alpha = 0.02$ already known from section 6.1. Table 6.7 additionally illustrates the same fit parameters obtained for the MP as for the SAP, except the components' intensities and the surface plasmon features, which already vanished at the SP. Thus, the components can be attributed to an Ag_2Ge surface alloy component, as well as to the metallic Ag component of a chemically unchanged Ag(111) surface. The Ag_2Ge component shows a massive surface effect in terms of increasing its intensity by a factor of almost 2 for high emission detection, which clearly demonstrates that the Ag_2Ge bonds are located closer to the surface than the metallic Ag bonds. In this case, the area ratio between the Ag_2Ge and the Ag component is reduced compared to the SAP, which is likely due to an increase in the metallic Ag bonds formed. Since the MP consists of contributions from the Ag_2Ge phase and the germanene phase, this suggests that the silver surface forms metallic bonds within the germanene phase, which do not interact with the germanene layer. This proposal of a chemically freestanding germanene phase being formed on Ag(111) will be examined in detail in the following section.

6.5 Quasi-Freestanding Germanene

The structural phase of quasi-freestanding germanene (QFG) is formed on Ag(111) at a coverage of approximately $\Lambda = 1.1\,\text{ML}$, as already illustrated in figure 5.5. Since its emergence, 2D materials have thoroughly been examined in theoretical studies to figure out their structural properties, such as the lattice constant a or buckling δ. For this purpose, stand-alone layers of 2D materials were considered, which led to the proposed structure parameters for freestanding 2D materials introduced in section 2.2. Experimentally synthesized 2D materials may be called *freestanding* if their structural parameters are equal to the theoretically proposed structure.
In the case of germanene on Ag(111), previous experimental studies determined the lattice constant of germanene to be $a_{\text{exp}} = 3.9\,\text{Å}$ [63, 65], which slightly differs from the theoretical proposed values for freestanding germanene of $a_{\text{theo}} = (3.97 - 4.06)\,\text{Å}$ [13, 106]. In addition to further deviations between experimentally and theoretically yielded values of buckling parameters, which will be discussed later, the germanene

phase on Ag(111) is termed *quasi*-freestanding [63].
Figure 6.18 displays LEED patterns at different kinetic energies obtained for the QFG phase at a coverage of $\Lambda = 1.1\,\mathrm{ML}$. The LEED pattern with the strongest reflection spots can be observed at a kinetic energy of $E_{\mathrm{kin}} = 40\,\mathrm{eV}$. Here, the reflection spots of the Ag(111) substrate are marked by blue circles while green circles highlight the Ge spots. Taking the Ge superstructure marked by the blue and green arrows into account, Yuhara *et al.* denoted this structure as a "(1.35×1.35)"R30°, indicating the short-range order of the Ge formation [65]. The spot tracing method carried out in figure 6.15 for the QFG phase returned a relative lattice constant of $a_{\mathrm{QFG}}/a_{\mathrm{Ag}} = 1.36 \pm 0.01$ for the germanene regarding the substrate leading to a "(1.36×1.36)"R30° reconstruction after Yuhara's notation. However, if one con-

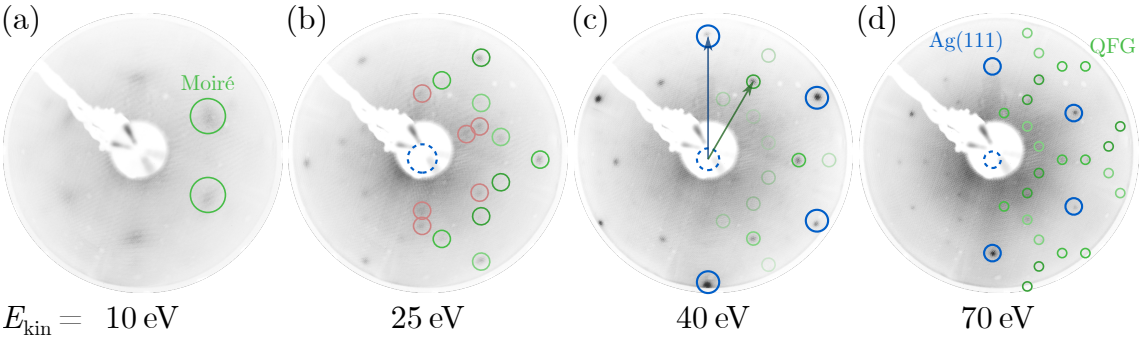

Figure 6.18: LEED patterns of the quasi-freestanding germanene phase obtained at a coverage of $\Lambda = 1.1\,\mathrm{ML}$. The patterns were recorded at (a) $E_{\mathrm{kin}} = 10\,\mathrm{eV}$, (b) $E_{\mathrm{kin}} = 25\,\mathrm{eV}$, (c) $E_{\mathrm{kin}} = 40\,\mathrm{eV}$, and $E_{\mathrm{kin}} = 70\,\mathrm{eV}$. The reflection spots in the right half of each pattern obeying the *LEEDpat* simulation are highlighted by green circles.

siders further reflection spots appearing at different kinetic energies, a more sufficient description of the superstructure is needed. In figure 6.18(d), a rectangular Rec $\{c(\sqrt{3} \times 7)\}$ with three domains was applied, as suggested by Oughaddou *et al.* [61, 64]. The reconstruction of the matrix $\left(\begin{smallmatrix} 3 & -1 \\ 1 & 2 \end{smallmatrix}\right)$ fully satisfies the periodicity of visible reflection spots when extinction of two spots before and after the substrate's spots of each domain due to multiple scattering processes is included [64]. Additionally, the Rec $\{c(\sqrt{3} \times 7)\}$ reconstruction also meets the "(1.36×1.36)"R30° reconstruction, as demonstrated by the green shading circles in figure 6.18(c) and some of the reflection spots depicted in the LEED pattern 6.18(b) obtained at $E_{\mathrm{kin}} = 25\,\mathrm{eV}$. However, the spots tagged by the red circles are not included in the rectangular

reconstruction. It can be concluded that a long-range periodicity, as indicated by appearing spots at low kinetic energies, is additionally involved in the diffraction pattern. Superstructures of a $(7\sqrt{7} \times 7\sqrt{7})$, a $(9\sqrt{3} \times 9\sqrt{3})$R30°, and a (12×12) were proposed as appropriate long-range structures [61, 65]. Figure 6.18(a), which was recorded at a kinetic energy of $E_{\mathrm{kin}} = 10\,\mathrm{eV}$ reveals weak features of diffraction spots not belonging to the mentioned reconstructions either. It can be assumed that the LEED patterns are superimposed by a Moiré structure [61], whose modulation was determined to be $\sim 9\,\text{Å}$ [63]. These Moiré signatures were already observed in LEED patterns at low kinetic energy of the MP, shown in figure 6.14(a).

In order to analyze the internal and interfacial structure of the QFG phase, HighRes XPS spectra of the Ge 3*d* and the Ag 3*d* core levels were measured, which are displayed in figures 6.19 and 6.20, respectively. The data of the Ge 3*d* signal were

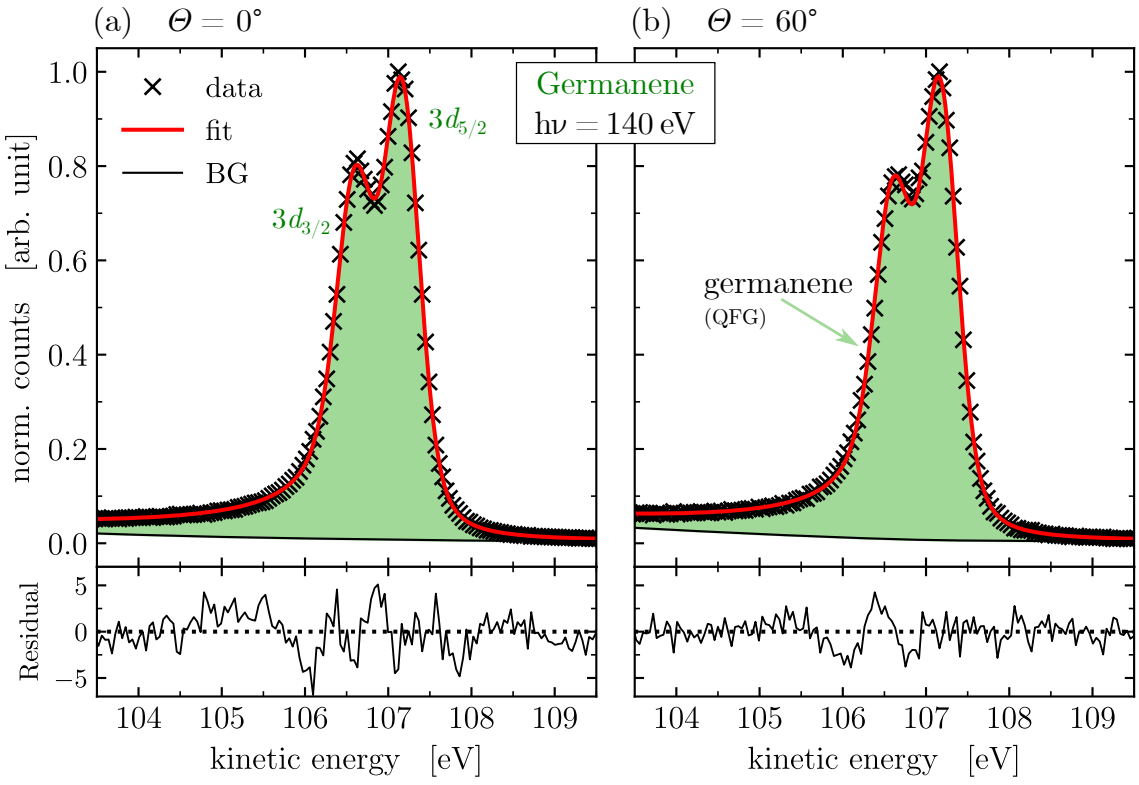

Figure 6.19: XPS HighRes spectra of the Ge 3*d* core level of the quasi-freestanding germanene phase at a coverage of $\Lambda = 1.1\,\mathrm{ML}$. The spectra were recorded at $\mathrm{h}\nu = 140\,\mathrm{eV}$, under emission angles of (a) $\Theta = 0°$ and (b) $\Theta = 60°$.

Table 6.8: Fit parameters obtained from the XPS analysis of the Ge 3*d* HighRes spectra of quasi-freestanding germanene in figure 6.19. All parameters refer to the $3d_{5/2}$ peak.

Fig. 6.19	Θ [°]	comp.	E_{kin} [eV]	E_{SOC} [eV]	FWHM [eV]	α	A_{rel} [%]
(a)	0	QFG	107.18	0.57	0.54	0.08	100.0
(b)	60	QFG	107.18	0.57	0.54	0.08	100.0

fitted by components of DS profiles, and a Tougaard background resulting in the best fit achieved using the fit parameters displayed in table 6.8. Obviously, only one single component was applied to the data, similarly known from XPS studies of freestanding graphene [207]. It can be concluded that the Ge atoms of QFG are all located in the same chemical environment within the honeycomb lattice. Consequently, this assumption weakens proposed structures of a high-buckled germanene phase [105] or a coexisting Ag_2Ge SAP below the QFG with strong interaction with the Ag substrate [43]. The applied QFG component features a broader FWHM compared to the components corresponding to the previous phases. As discussed in section 3.1.5, a broadening of the FWHM can result from a structural disorder of the probed sample system. Indeed, STM measurements revealed local disorders of the QFG structure caused by domain rotations and compressive strain. Nevertheless, a long-range order of the germanene was again observed, as additionally confirmed by the respective LEED pattern. [60, 63, 65, 66] This called *ordered disorder* [196] of the QFG on Ag(111) may be responsible for some broadening effects in the experimental data. A notable asymmetry of the XPS peaks is most commonly experienced for metallic materials [158], though the asymmetry parameter obtained for QFG is $\alpha = 0.08$. Since the considerable asymmetry values of the previously presented Ge 3*d* core level signals are caused by a discussed influence of the metallic Ag substrate, nothing of the sort is expected here. Furthermore, the asymmetry can indicate rather sp^2-hybridized bonds within the internal structure of the OFG, analogous to graphene [208], which commonly stands for a low-buckled formation [80].
In figure 6.20, the corresponding Ag 3*d* core level spectra of the QFG phase are displayed. These spectra representing the bonding structure at the interface also evince only one single component as the best resulting fit of the data. All further fit parameters are provided in table 6.9. The applied Shirley background increases to a higher level compared to the previous Ag spectra, which can especially be recognized

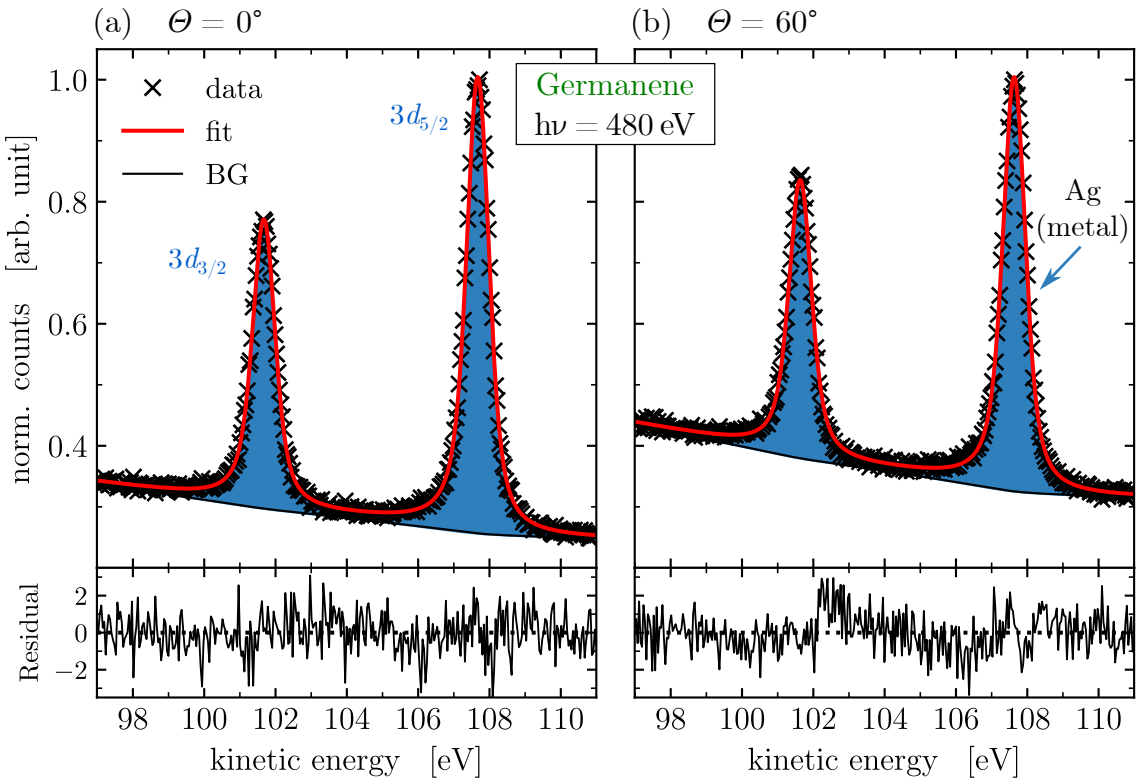

Figure 6.20: XPS HighRes spectra of the Ag 3*d* core level of the quasi-freestanding germanene phase at a coverage of $\Lambda = 1.1$ ML. The spectra were recorded at $h\nu = 480$ eV, under emission angles of (a) $\Theta = 0°$ and (b) $\Theta = 60°$.

in figure 6.20(b). Due to the high Ge coverage of the QFG phase, the energy loss of the photoelectrons through inelastic scattering within the Ge film rises, which leads to higher background. The metallic Ag component as a single contribution to the total signal indicates the metallic state of the Ag(111) surface covered by germanium. Also, a poor interaction at the interface between substrate and the adsorbate can

Table 6.9: Fit parameters obtained from the XPS analysis of the Ag 3*d* HighRes spectra of quasi-freestanding germanene in figure 6.20. All parameters refer to the $3d_{5/2}$ peak.

Fig. 6.20	Θ [°]	comp.	E_{kin} [eV]	E_{SOC} [eV]	FWHM [eV]	α	A_{rel} [%]
(a)	0	Ag	107.68	6.00	0.77	0.02	100.0
(b)	60	Ag	107.64	6.00	0.77	0.02	100.0

be assumed, which is concluded from a missing interface component in both Ge 3*d* and Ag 3*d* core level spectra. Besides the significant background in both spectra of figure 6.20, the peaks' shape is very similar to the peaks obtained for the clean Ag(111) sample displayed in figure 6.3, additionally supported by the obtained fit parameters for both phases.
From this and in combination with our findings of the internal structure of QFG, as discussed in figure 6.19, we can conclude on a chemically freestanding germanene phase on Ag(111) since no strong interaction or structural deformation at the Ge-Ag interface could be noted. Moreover, since the results of the internal and interfacial structure analysis of the XPS data obtained for QFG is in clear contrast to the analysis carried out for the previous MP phase, it can be stated that a new structural formation at $\Lambda = 1.1\,\mathrm{ML}$ is formed. These findings firmly challenge reports about the absence of a germanene formation on Ag(111) [60]. Further hints and supporting results of successfully synthesized quasi-freestanding germanene are provided in the following paragraph.

In order to determine the specific structural assembly of the finally formed quasi-freestanding germanene phase, we again performed XPD measurements and simulations of the Ge 3*d* core level, which are presented in figure 6.21. The experimentally

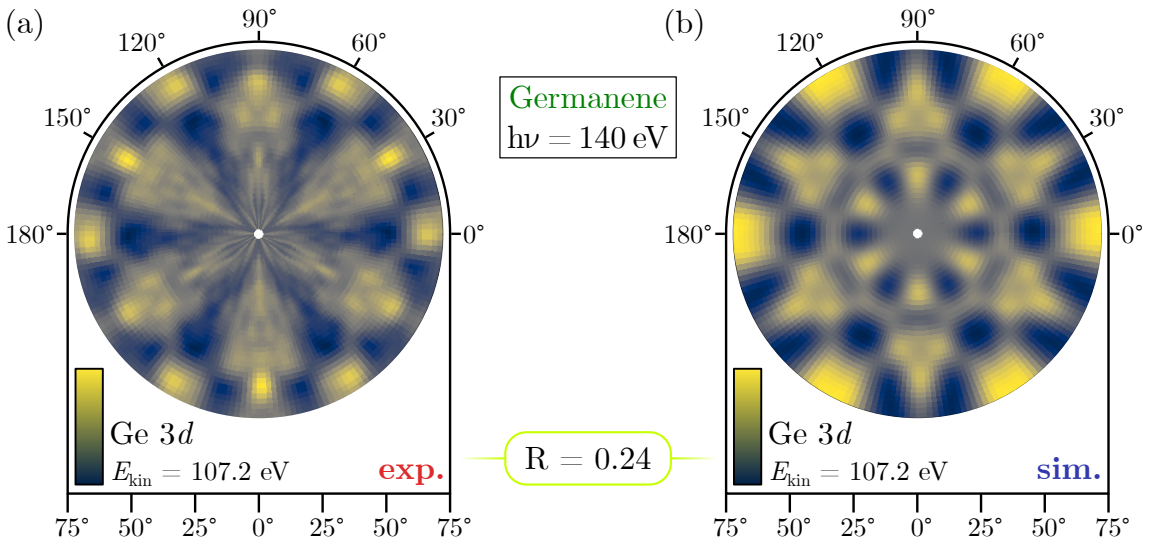

Figure 6.21: XPD analysis of the quasi-freestanding germanene phase. (a) Experimental and (b) simulated XPD-pattern for the Ge 3*d* emitter of QFG, with a kinetic energy of $E_{\mathrm{kin}} = 107.2\,\mathrm{eV}$, obtained at $\mathrm{h}\nu = 140\,\mathrm{eV}$. The best R-factor was returned with $\mathrm{R} = 0.24$.

obtained XPD pattern for the Ge 3*d* emitter with a kinetic energy of $E_{\mathrm{kin}} = 107.2\,\mathrm{eV}$, displayed in figure 6.21(a), was recorded at a photon energy of $h\nu = 140\,\mathrm{eV}$ and appeared in threefold rotational symmetry. The corresponding simulation, shown in figure 6.21(b), was performed analogously to the XPD analysis carried out for the Ag_2Ge SAP in section 6.2. Using the same input parameters, the genetic algorithm was initiated with a start structure of a low-buckling honeycomb lattice as proposed by Yuhara *et al.* [65]. The best matching diffraction pattern simulated was returned with an R-factor of R = 0.24 and is presented in figure 6.20(b). At first glance, the comparison of experimental and simulated XPD pattern show agreement in symmetry and main features of maxima and minima, especially in the surface-sensitive high-polar angle region. With a closer look, the feature structure of figure 6.20(a) seems blurred and less intense with respect to the simulation, which results in a comparatively poor R-factor. Considering the ratio of the peak-to-peak anisotropies

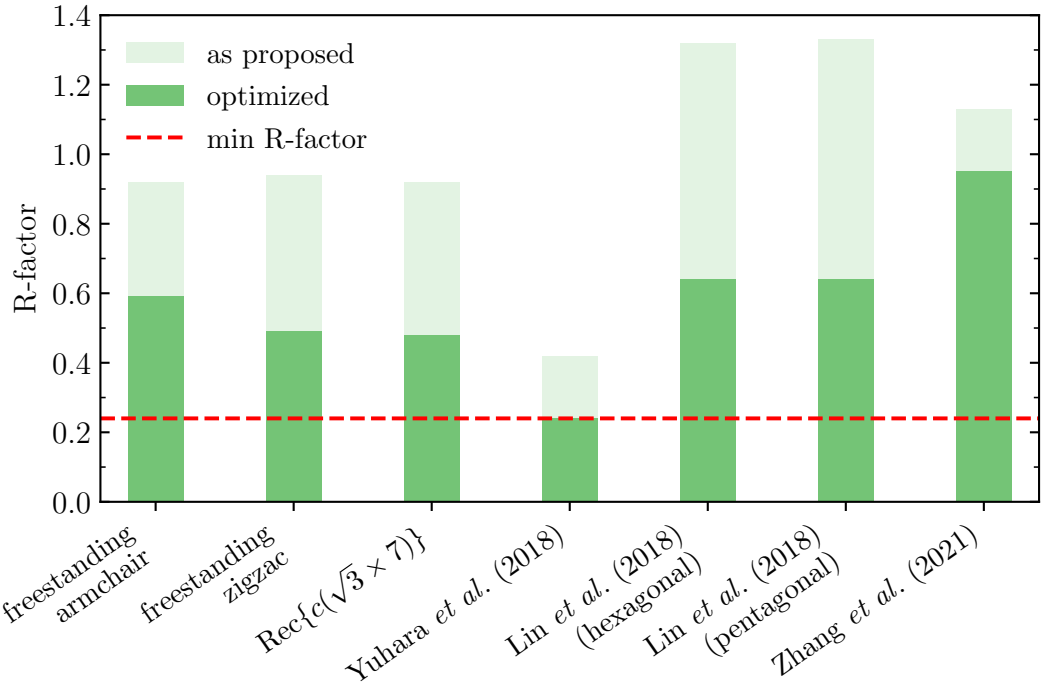

Figure 6.22: Overview of resulting R-factors corresponding to XPD simulations carried out for proposed test structures of germanene on Ag(111),before and after the optimization by the genetic algorithm. The tested structure models are based on theoretical structures for freestanding germanene and recent publications [13, 62–65]. Figure reproduced from [196].

of the experimental and the simulated pattern, the anisotropy range of the simulation is 6.7 times larger than that of the experiment. The already mentioned ordered disorder of the QFG may influence the experimental XPD pattern in the way of attenuating and blurring the diffraction features. Additionally, the unit cell of the proposed germanene superstructure is expected to be 5.35 nm that is close to the experimental limit of the XPD method.

However, several structure models gathered from the literature were used as test structures for the XPD simulation procedure. Figure 6.22 provides an overview of the resulting R-factors for all tested structure models in the literature. All structure models were evaluated by their corresponding R-factor after a simulation of the originally proposed structure (transparent green) and after the structural optimization by the genetic algorithm (green). The test structures also include the theoretical model of freestanding germanene orientated in zigzag and armchair direction with respect to the Ag(111) substrate, as well as a structure model satisfying the Rec $\{c\,(\sqrt{3}\times 7)\}$ reconstruction, as identified from LEED measurements in figure 6.18. It can unequiv-

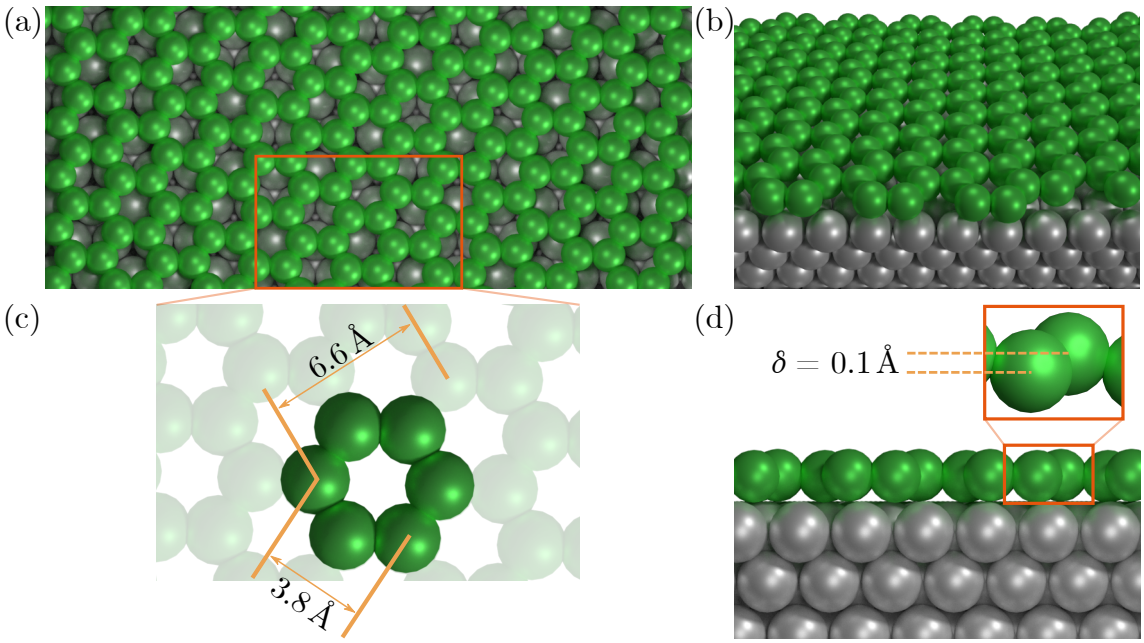

Figure 6.23: Structure model of quasi-freestanding germanene on Ag(111) in (a) top and (b) perspective view, obtained from the XPD simulation in figure 6.21(b). (c) A close-up of the stand-alone honeycomb lattice illustrates the yielded lattice constant a, periodic length l_{ac}, as well as (d) the buckling height δ in side view. Reproduced from [196].

ocally be determined that an optimized test structured as proposed by Yuhara *et al.* results by far in the best R-factor.
Figure 6.23 illustrates the structure model corresponding to the best simulated XPD pattern returned, which is depicted in figure 6.21(b). The structure, displayed in top and perspective view in figure 6.23(a) and (b), respectively, satisfies a $\left(7\sqrt{7} \times 7\sqrt{7}\right)$ R19.1° reconstruction, as proposed by Yuhara *et al.* The close-up of the honeycomb lattice in figure 6.23(c) visualizes the structural parameters returned as a lattice constant of $a = 3.8\,\text{Å}$, leading to the nearest neighbor distance of $d = 2.2\,\text{Å}$, and a periodic length of $l_{\text{ac}} = 3.8\,\text{Å}$. With a maximum deviation of 2.6 %, these values are in excellent agreement with similar investigations of germanene on Ag(111) [63, 65], and even with proposed structures on other substrates, such as Au(111) and MoS_2 [15, 209]. Figure 6.23(d) shows the Ge-Ag interface structure of QFG. The minimum spacing between adsorbate and substrate measures $d_z = 2.6\,\text{Å}$, which supports the observations from XPS regarding the weak interface interaction. Moreover, a very low buckling of $\delta = 0.1\,\text{Å}$ was obtained for the honeycomb structure. This value is six times smaller than the theoretical buckling height of freestanding germanene and even nine times smaller than DFT calculations of germanene on Ag(111) [13, 63]. On the contrary, this low buckling has been observed experimentally and is supported by the XPS results discussed above regarding the number and asymmetry of the applied components. In addition to the XPS results, the found structure finally rules out reports of the absence of a germanene formation [60] or a germanene growth on top of the Ag_2Ge alloy [43].
Based on the investigation of QFG carried out here, the germanene phase on Ag(111) can be determined to be *quasi*-freestanding because its structural parameters slightly differ from theoretical models of freestanding germanene. However, we found a chemically isolated honeycomb structure with a surprisingly low buckling height, which in turn is in very good accordance to a germanene phase which was epitaxially grown via segregation through Ag(111) [65].

6.6 Encapsulation with Al_2O_3

Bringing 2D materials to technological applications is a challenging task. Besides the mass production of homogenous, large-scaled 2D sheets free of contamina-

tion, also the operation of 2D material-based devices outside the vacuum exposed to atmospheric conditions may be a hurdle for applications. In the course of the development of the first Xene-based transistors, one approach to take advantage of 2D materials in electronic devices was to cap the sheet with an isolating layer of Al_2O_3, as is principally illustrated in figure 6.24. In the case of the first silicene FET, the silicene grown on Ag(111) was encapsulated by a capping layer of Al_2O_3 in order to turn it into a device [20]. The question remaining is how the encapsulation of the respective 2D sheet affects its structure. A handful of studies have already dealt with this particular issue [210–212]. In the case of germanene, it was found that an encapsulation can only be realized using VdW materials to retain the germanene's structure since the use of an Al_2O_3 capping layer results in no germanene formation [212]. However, this study refers to a sample system of encapsulated germanene obtained by segregation.

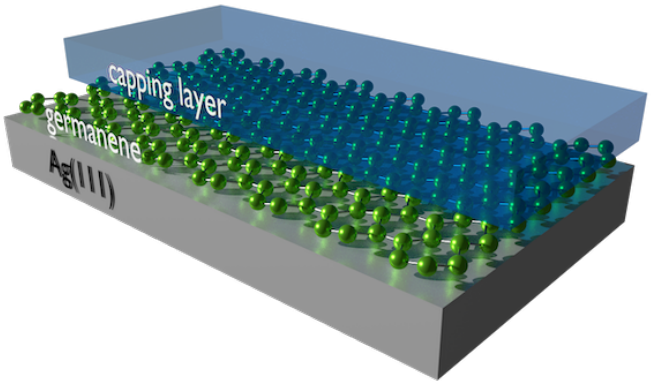

Figure 6.24: Principle illustration of a sample system of germanene on Ag(111) encapsulated by a Al_2O_3 capping layer.

After thoughtfully examining the 2D material germanene regarding its structural properties, which turned out to be freestanding on Ag(111) and therefore a promising candidate for application, here, an applied prospect is delivered to use 2D materials *ex situ*. In contrast to the study of Suzuki *et al.* mentioned above, in this work, a capping layer of Al_2O_3 deposited by means of PVD was used to encapsulate the Ag_2Ge surface alloy phase (SAP) formed on Ag(111). The SAP was proven to show Dirac cones in its band structure [42, 43], which is why it has a remarkable prospect of application for technological progress.

A sample system of Al_2O_3 /Ge/Ag(111) is principally visualized in figure 6.24. In this work, the SAP was used as a buried interlayer by PVD-coating the sample with a capping layer of Al_2O_3. Figure 6.25 illustrates the preparation process of the sample system by LEED pattern obtained at the respective preparation stage. Figure 6.25(a)

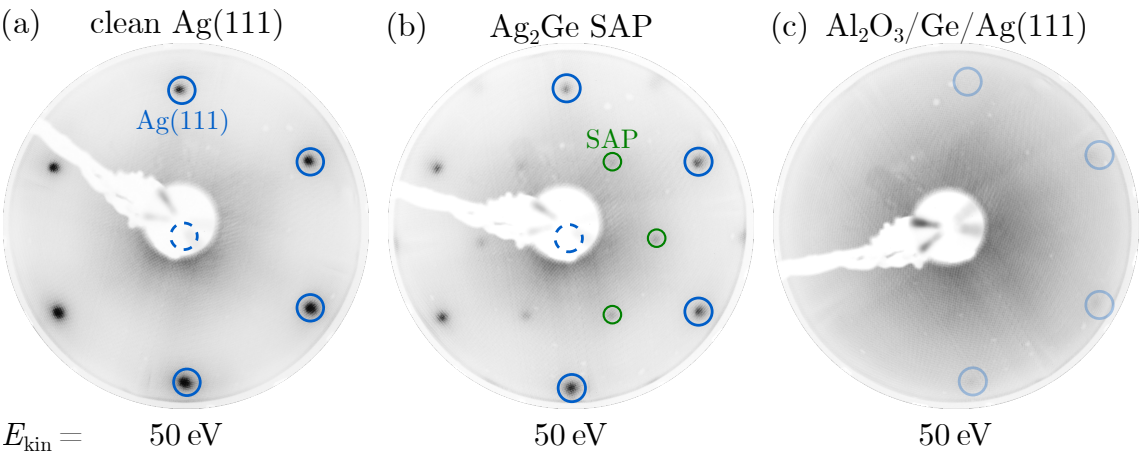

Figure 6.25: LEED patterns of (a) clean Ag(111), (b) the pure SAP, and (c) the SAP after the encapsulaion with Al_2O_3. All patterns were recorded at $E_{kin} = 50\,eV$ and characteristic diffraction spots were highlighted in the right half of each pattern by circles resulting from *LEEDpat* simulations.

shows the LEED pattern of a clean Ag(111) sample obtained at a kinetic energy of $E_{kin} = 50\,eV$, which was covered by a germanium film of a thickness of $\Lambda = 1/3\,ML$ afterward, forming the Ag_2Ge SAP, as displayed in figure 6.25(b). The blue and green circles mark the diffraction spots of the Ag(111) substrate and of the SAP, respectively, which satisfy the expected $(\sqrt{3} \times \sqrt{3})R30°$ reconstruction, discussed in section 6.2. After the deposition of the capping layer consisting of Al_2O_3, the previously observed diffraction spots vanish, as depicted in figure 6.25(c). Only at a closer look, features of the substrate's spots are faintly visible, as indicated by the blue circles. It allows one to conclude that an amorphous capping layer was successfully deposited on the sample's surface.

Further analysis with more chemical sensitivity of the capping layer deposited can be carried out on the basis of angle-resolved XPS survey spectra, recorded at $h\nu = 700\,eV$, which are presented in figure 6.26. As a reference, a survey spectrum of the SAP before the encapsulation is provided at the bottom of figure 6.26. The spectra obtained at a polar angle of $\Theta = 60°$ reveal the chemical composition of the sample systems with high surface sensitivity. At the top, the elastic photoelectron and Auger lines attributed to the Al_2O_3 film are annotated in red and purple, corresponding to the O and Al signals, respectively. Since the absence of residues is determined in the spectra, the deposited capping layer can be characterized as pure Al_2O_3 without impurities. The capping layer is estimated to have a thickness of approximately

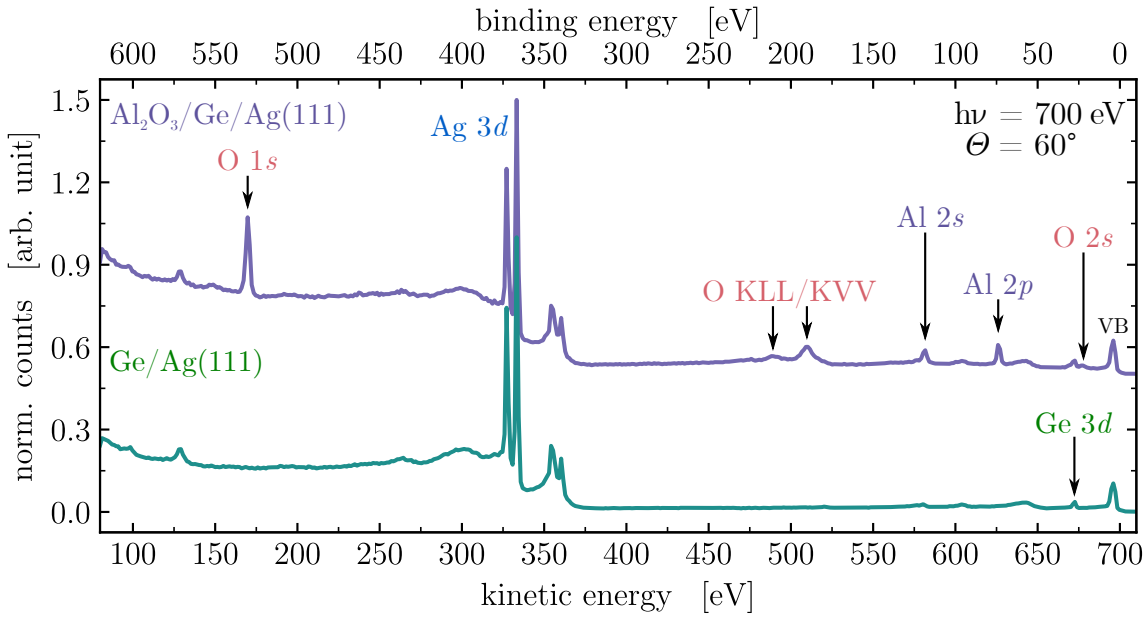

Figure 6.26: XPS survey spectrum after the encapsulation of the SAP sample system with a capping layer of Al_2O_3. The spectra were recorded at a photon energy of $h\nu = 700\,eV$ and under emission angles of (a) $\Theta = 60°$ and (b) $\Theta = 0°$. The characteristic XPS features of O and Al of Al_2O_3 are tagged by red and purple lables, respectively.

$\Lambda = 1\,ML$, which is sufficient for the structural analysis of the buried Ge interlayer but can be increased for further applications.

Table 6.10: Fit parameters obtained from the XPS analysis of the Ag $3d$ HighRes spectra of the capping layer in figure 6.27. All parameters refer to the $3d_{5/2}$ peak.

Fig. 6.27	Θ [°]	comp.	E_{kin} [eV]	E_{SOC} [eV]	FWHM [eV]	α	A_{rel} [%]
(a)	0	Ag	107.78	6.01	0.84	0.02	62.3
		Ag_2Ge	107.63	6.01	0.73	0.02	36.3
		P1	103.83		1.14	0.00	0.4
		P2	97.83		1.15	0.00	1.1
(b)	60	Ag	107.75	6.01	0.84	0.02	56.3
		Ag_2Ge	107.60	6.01	0.73	0.02	40.3
		P1	103.80		1.14	0.00	1.1
		P2	97.80		1.15	0.00	2.2

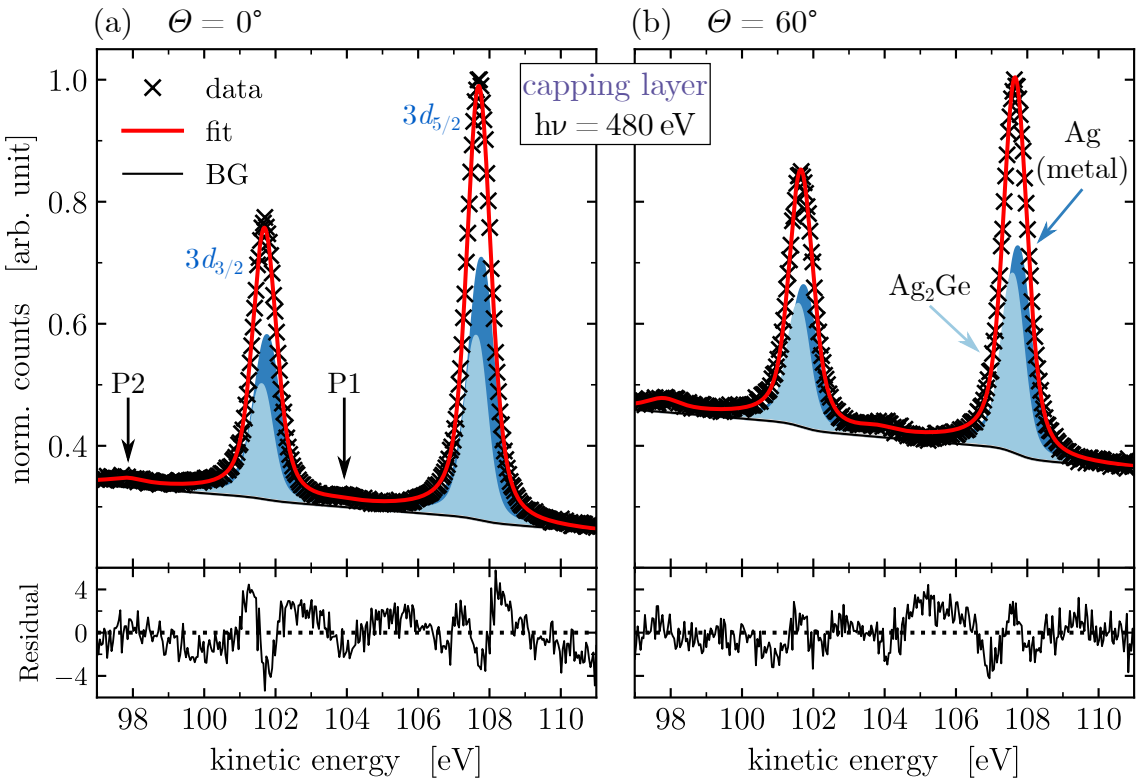

Figure 6.27: XPS HighRes spectra of the Ag 3*d* core level of the SAP at a coverage of $\Lambda = 1/3$ ML. The spectra were recorded at $h\nu = 480$ eV, under emission angles of (a) $\Theta = 0°$ and (b) $\Theta = 60°$.

More attention should be paid to HighRes XPS spectra of the Ge 3*d* , Ag 3*d* , as well as the Al 2*p* and the O 1*s* core levels to examine the internal and interfacial structure of the sample system. Starting from the Ag(111) substrate, figure 6.27 shows the XPS HighRes spectra of the Ag 3*d* core level. Comparing the signals' shape and the corresponding fit parameters displayed in table 6.10 to the ones of the SAP discussed in section 6.2, no significant changes can be noted. Besides the higher background level compared to figure 6.7 due to the added capping layer, the signal was again fitted by two components, and two surface plasmon features, whose fit parameters agree very well with the values of table 6.3 obtained for the SAP. A slight broadening of the metallic Ag and the Ag_2Ge component by 8 % and 9 %, respectively, regarding the SAP components, can be identified, which may also be caused by the applied unorder of the amorphous capping layer. Nevertheless, no change of the Ag-Ge interface structure, as indicated by the Ag 3*d* core level, which might have been induced by the encapsulation with Al_2O_3, is detected.

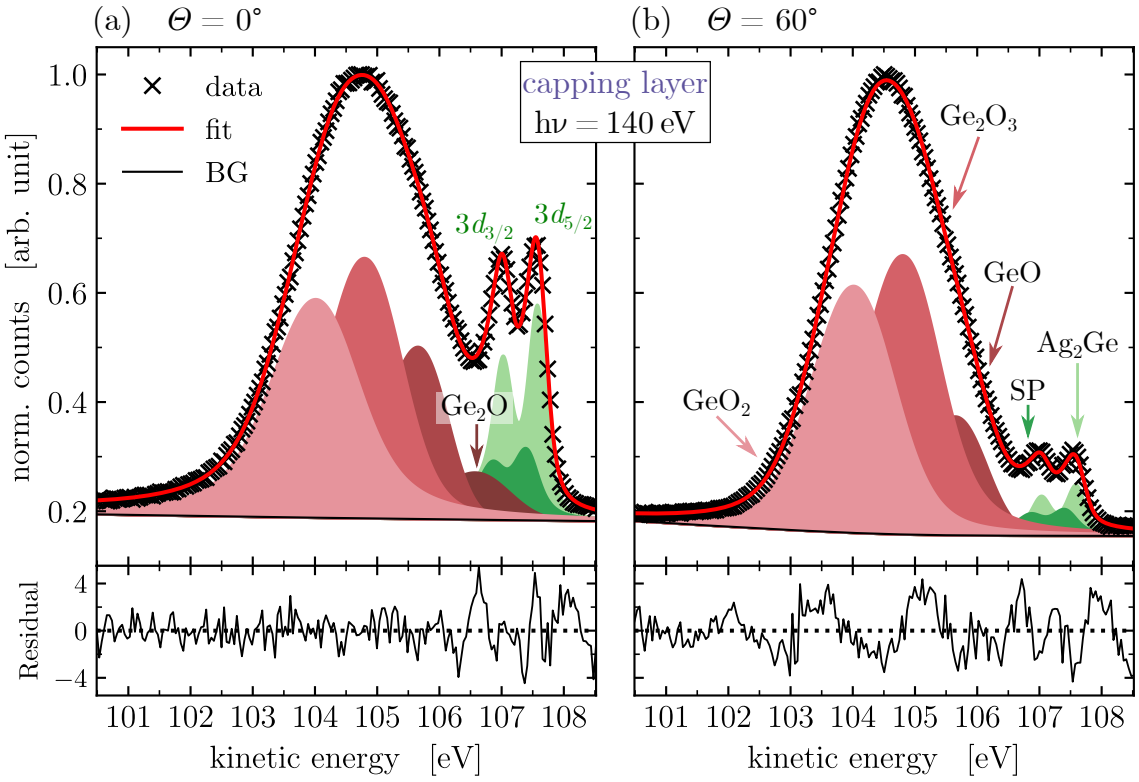

Figure 6.28: XPS HighRes spectra of the Ge 3*d* core level of the SAP at a coverage of $\Lambda = 1/3$ ML. The spectra were recorded at $h\nu = 140$ eV, under emission angles of (a) $\Theta = 0°$ and (b) $\Theta = 60°$.

Figure 6.28 depicts the HighRes core level spectra of the Ge 3*d* signal obtained for the encapsulated SAP. Even at a first qualitative glance, a significant change in the peak shape can be reported with respect to the Ge 3*d* spectra of the stand-alone SAP in figure 6.6. Since the spin-orbit split 3*d* peak of the germanium is still clearly visible, another massive peak arises, shifted towards lower kinetic energies. The additional peak's intensity increases relative to the Ge signal for detection under $\Theta = 60°$, so its emitters might be attributed to the capping layer, which is closer to the surface than the germanium contribution. The quantitative analysis of the spectra displayed in figure 6.28 recovered the expected composition of the SAP at the right part of each spectrum, as previously yielded in figure 6.6. Table 6.11 additionally provides the resulting fit parameters obtained for the analysis in figure 6.28. The Ag_2Ge and SP components can be recognized from figure 6.6 by the same energy shift and peak shape, only differing by a slightly higher FWHM, as already discussed for the Ag 3*d* signal.

Furthermore, the additional peak next to the internal Ge signal can be decomposed

Table 6.11: Fit parameters obtained from the XPS analysis of the Ge 3*d* HighRes spectra of the capping layer in figure 6.28. All parameters refer to the $3d_{5/2}$ peak.

Fig. 6.28	Θ [°]	comp.	E_{kin} [eV]	E_{SOC} [eV]	FWHM [eV]	α	A_{rel} [%]
(a)	0	Ag_2Ge	107.60	0.56	0.38	0.13	15.5
		SP	107.42	0.56	0.53	0.13	7.1
		Ge_2O	106.76	0.56	1.10	0.0	4.4
		GeO	105.82	0.56	0.91	0.0	14.2
		Ge_2O_3	104.99	0.56	1.24	0.0	28.3
		GeO_2	104.21	0.56	1.51	0.0	30.7
(b)	60	Ag_2Ge	107.61	0.56	0.38	0.13	4.6
		SP	107.43	0.56	0.53	0.13	3.3
		Ge_2O	106.77	0.56	1.11	0.0	1.1
		GeO	105.83	0.56	0.96	0.0	12.5
		Ge_2O_3	105.00	0.56	1.26	0.0	41.2
		GeO_2	104.22	0.56	1.39	0.0	37.3

into four oxygen compounds representing the four oxidation stages of germanium [213]. The components are chemically shifted by $E_{\text{chem}} = 0.84\,\text{eV}$, 1.78 eV, 2.61 eV, and 3.39 eV, which is in excellent agreement with the values reported in literature. These components can be attributed to the chemical compounds Ge_2O, GeO, Ge_2O_3, and GeO_2, respectively, corresponding to the oxidation states 1+ to 4+ [213]. As already mentioned above, the total of all oxidation compounds increases for higher polar angles by 19 %, which supports the assumption that the oxygen bonds are located at the Ge-Al_2O_3 interface. Thus, the XPS analysis of the Ge 3*d* core level signal revealed the oxidation of the Ge layer by encapsulation with Al_2O_3.

Additionally, the internal structure of the Al_2O_3 capping layer can be examined by analyzing the Al 2*p* and O 1*s* core level spectra, which are presented in figure 6.29. The Al 2*p* signal was measured with a photon energy of $h\nu = 140\,\text{eV}$ and the O 1*s* core level with $h\nu = 600\,\text{eV}$, while both spectra were recorded at normal emission. The corresponding fit parameters are listed in table 6.12, which are in very good agreement with XPS studies of Al_2O_3 [214]. The best fit of the Al 2*p* signal was achieved by applying one single Voigt-like component to the data, assigned to the Al_2O_3 compound, with a spin-orbit separation of $E_{\text{SOC}} = 0.40\,\text{eV}$ [215]. Consequently, the O 1*s* core level also revealed an Al_2O_3 component and a OH compound chemically shifted by $E_{\text{chem}} = 0.73\,\text{eV}$ towards lower kinetic energies [214]. Additionally, a

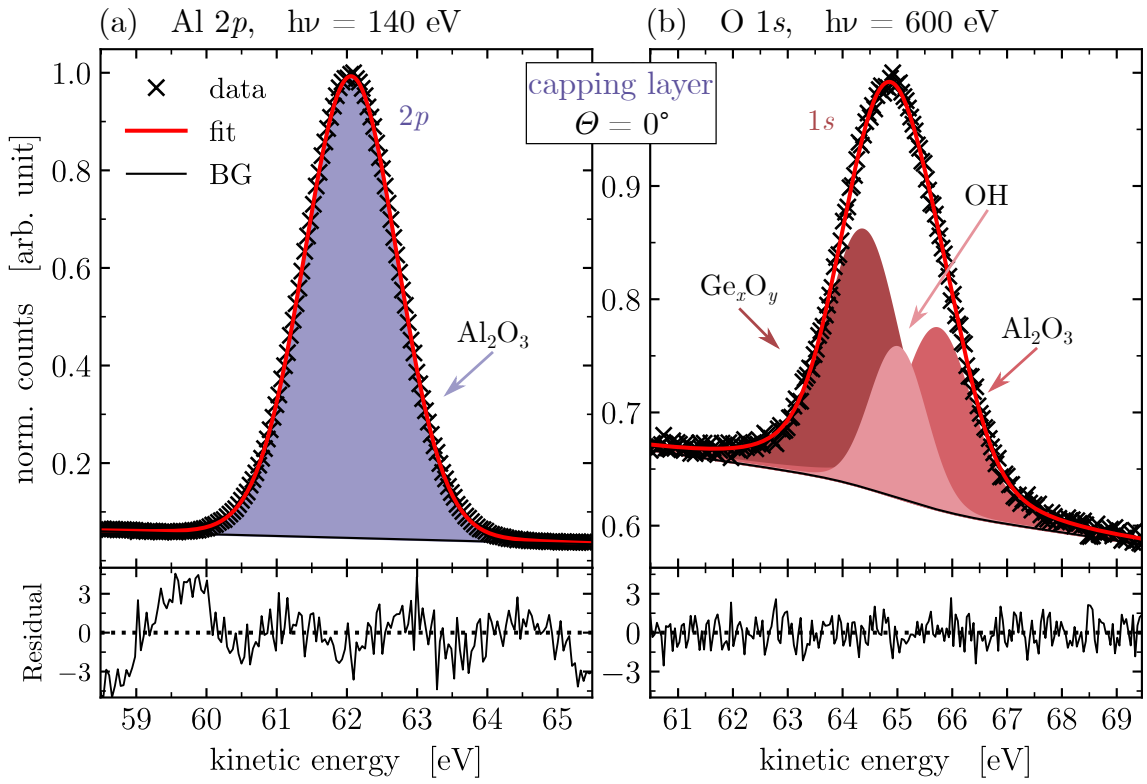

Figure 6.29: XPS HighRes spectra of the (a) Al 2p and (b) O 1s core levels of the Al_2O_3 capping layer encapsulating the. The spectra were recorded under normal emission at (a) hν = 140 eV and (b) hν = 600 eV.

third component can be observed, which might be attributed to the Ge_xO_y oxide compounds, as assumed from the Ge 3d signal. The bonds of the oxide compounds are accumulated in one component due to their similar chemical structure and the associated weak discriminability in the O 1s core level signal. A similar peak composition of this signal was observed for a carbide compound in Al_2O_3 [214],

Table 6.12: Fit parameters obtained from the XPS analysis of the Al 2p and O 1s HighRes spectra of the capping layer in figure 6.29.

Fig. 6.29	signal	comp.	E_{kin} [eV]	E_{SOC} [eV]	FWHM [eV]	α	A_{rel} [%]
(a)	Al 2p	Al_2O_3	62.19	0.40	1.50	0.0	100.0
(b)	O 1s	Al_2O_3	65.74		1.51	0.0	32.0
		OH	65.01		1.19	0.0	18.9
		Ge_xO_y	64.38		1.60	0.0	49.1

the position of which can also be transferred to a Ge bond due to a comparable electronegativity. The Ge_xO_y component is shifted by $E_{chem} = 1.36\,eV$ towards lower kinetic energies and takes the major contribution of the O $1s$ signal's intensity. It confirms the observation made in figure 6.28 of a strong oxidation affinity of the Ge atoms upon the encapsulation with Al_2O_3.

As the oxidation of the SAP induced by the Al_2O_3 capping layer was figured out, a focus is now on the structural analysis of the buried Ge interlayer after the encapsulation. For this purpose, XPD measurements of the Ge $3d$ core level of the encapsulated SAP have been performed. Due to the limited availability of beamtime, only a polar angle range of $40° \leq \Theta \leq 70°$ was recorded. The XPD

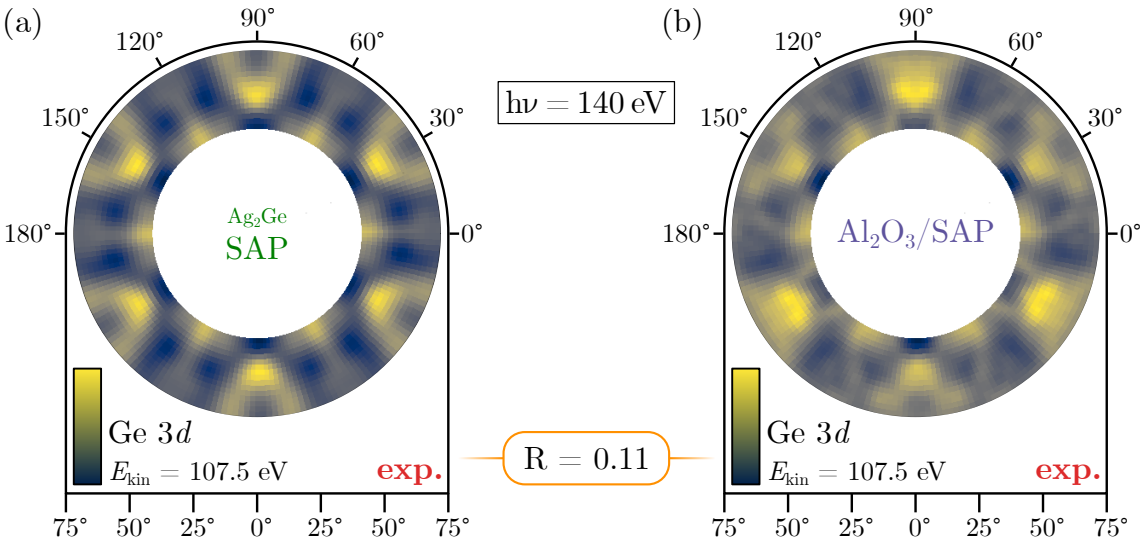

Figure 6.30: Qualitative XPD analysis of the Ag_2Ge SAP phase as a buried interlayer encapsulated with a capping layer of Al_2O_3. (a) The experimental XPD pattern of the stand-alone SAP and (b) the experimental pattern of the encapsulated SAP were obtained at $h\nu = 140\,eV$ resulting in a kinetic energy of $E_{kin} = 107.5\,eV$ for the Ge $3d$ emitters. The congruence of both pattern corresponds to an R-factor of R = 0.11.

simulation of sample systems with amorphous layers involved, such as the Al_2O_3 layer, is challenging because periodic boundary conditions of the probed sample system are essential for the XPD methods, and thus, the calculated XPD pattern may be falsified. For this reason, the analysis was limited to a qualitative one. XPD patterns of the Ge $3d$ were recorded on the stand-alone SAP before the encapsulation with Al_2O_3 and after the encapsulation. The respective patterns are presented in

figure 6.30(a) for the pure SAP and figure 6.30(b) for the SAP with the capping layer of Al_2O_3 deposited. The R-factor of both patterns formed results in R = 0.11, which indicates a remarkably high agreement. Despite the deposition of the capping layer, main intensity features and structures are retained, which are clearly visible in the course of the azimuthal axes $\Phi = 30°$, 60°, and 90°, for instance. Furthermore, less distinctive maxima and minima can be noted, which is owed to a lower anisotropy than obtained for the SAP in figure 6.30(a). The amorphous capping layer causes inelastic scattering of the photoelectron waves originating from the ordered SAP structure, which results in a blurred and distorted appearance of the XPD pattern, as can be observed in figure 6.30(b).

Based on the XPD analysis, the structural change of the Ag_2Ge SAP structure induced by the encapsulation with Al_2O_3 can be evaluated as minimal and neglectable. In the face of the considerable oxidation of the Ge interlayer determined here and the likely associated change of the electronic properties of the SAP, at least the structure of the surface alloy phase is retained even as a buried interlayer upon the encapsulation with the Al_2O_3 capping layer. These results can serve as a prospect for further studies on the encapsulation of germanene phases by means of PVD-coating since a significant disturbance of the structural formation of germanene by an Al_2O_3 capping layer was reported using the segregation method [212].

Chapter 7

Conclusion

This work presented a detailed analysis of the structural phases formed within the structural evolution towards germanene formation on Ag(111). All found phases were structurally characterized using LEED measurements and high-resolution XPS and XPD experiments with synchrotron radiation provided by the DELTA synchrotron radiation source. In order to provide a perspective on the application of emerging 2D materials, a proof-of-concept method was conducted to preserve an *in situ* prepared germanene phase for use under ambient conditions. Structural analysis of an Al_2O_3-encapsulated Ag_2Ge surface alloy could be performed to gain knowledge about the structure development of the germanene phase due to the influence of the capping layer.

As an initial step, the surface of the Ag(111) crystal was prepared to serve as a sufficient carrier substrate for the germanene phases. The (1×1) reconstruction of the surface, as well as the absence of contaminating residues, was shown by LEED and XPS survey measurements, respectively. A more detailed analysis carried out by XPS HighRes spectra of the VB and the Ag $3d$ core level pointed out the atomically ordered and cleaned surface.
The structural evolution of germanene was examined by the stepwise increase of the Ge coverage Λ by means of PVD and the simultaneous observation of the structural phases formed. Using this method, four different formations were determined with respect to their superstructure, as observed by LEED measurements.
The first phase, called the Ag_2Ge surface alloy phase (SAP), was observed at a coverage of $\Lambda = 1/3\,\mathrm{ML}$ to form a $\left(\sqrt{3} \times \sqrt{3}\right)\mathrm{R30}^\circ$ reconstruction. The XPD analysis performed here revealed its alloy structure consisting of Ge atoms embedded in the uppermost Ag layer by exchanging Ag and Ge atoms within the surface plane [60].

Increasing the surface coverage slightly to $\Lambda = 0.4\,\mathrm{ML}$, the striped phase (SP) was recognized, which is named after its stripes-like appearance in STM images due to a periodic modulation of the electron density along the $[1\bar{1}0]$ direction [62]. The modulation results from a compressive strain of the surface alloy layer [63] leading to an incommensurate and corrugated Ag_2Ge alloy formation [62]. The LEED analysis presented here determined a Rec($\sqrt{3} \times 17$) with three domains, whereas the incommensurability and corrugation of the SP structure was proven with the help of HighRes XPS measurements.
A mixed phase (MP) was recovered at a Ge coverage of $\Lambda = 0.6\,\mathrm{ML}$. This intermediate phase means a domain-like superposition of the coexisting alloy and germanene phase, which could clearly be identified by their respective signatures in LEED and HighRes XPS measurements. Moreover, STM investigation of the MP show sharp domain edges between the alloy and germanene phase instead of stacked structures as commonly proposed for germanene formations [43].
The finally formed phase on Ag(111) at $\Lambda = 1.1\,\mathrm{ML}$ is called quasi-freestanding germanene (QFG) because of its conforming but yet differing structural parameters regarding theoretical proposes of freestanding germanene [63]. The LEED patterns exhibit a germanene superstructure describable by a Rec $\left\{c\left(\sqrt{3} \times 7\right)\right\}$ reconstruction with three domains, which is additionally superimposed by a Moiré and another long-range structure. The intriguing results of the XPS analysis carried out here revealed a chemically freestanding germanene phase, which is only VdW bound to the Ag(111) substrate. This observation is supported by the corresponding XPD examination of the germanene phase coming to the same conclusion of an incommensurate but chemically freestanding germanene phase with respect to the substrate. Moreover, a low-buckling of $\delta = 0.1\,\text{Å}$ for the QFG phase was figured out, fitting into the mold of the metal-like shape of the individual Ge $3d$ core level spectra. The results obtained in this work offer a promising perspective for quasi-freestanding germanene grown on Ag(111). Due to its weak bonding to the substrate, it provides the related possibility of detaching the germanene sheet and to take advantage of its proposed metallic character instead of the theoretically expected semiconducting behavior.
Finally, the proof-of-principle to encapsulate a germanene phase with Al_2O_3 while preserving its structure succeeded. Although the Ge atoms within the SAP tend to oxidize immediately after the encapsulation, its originally formed structure remains unchanged under the capping layer of Al_2O_3 , as shown by XPD measurements.

At this point, the key question of this work, how the process of structure formation towards germanene on Ag(111) comes about, was answered exhaustively and successfully.

The prospect of 2D materials for technological application is auspicious, not least because of relentless research into their properties with encouraging results. Above all, the critical discussion of controversial structural models proposed is highly topical and contemporary for the progress in the field of 2D materials. Once the synthesis and material properties are determined, further steps towards applications of Xenes and heterostructures can be faced. In this way, developing solutions for the *ex situ* operation of 2D materials is essential. Since the encapsulation method presented here turned out encouraging, it is vital to study further germanene phases. Consequently, the structural development during the encapsulation of weak substrate-bound quasi-freestanding germanene needs to be focused on, combined with an examination of its electronic properties, such as the corresponding band structure.
In addition to the vast research area of studying mono and poly-elemental Xenes of group IVA and beyond, including functionalization and heterostructures, low-dimensional materials, such as one-dimensional nano-ribbons should find quick mentioning here. Reports of the first realization of germanium nano-ribbons on Ag(110) [216] foreshadow an expandable potential to fabricate low-dimensional materials-based devices. First results on the structural evolution towards the formation of germanium nano-ribbons on Ag(110) are already provided in, Kesper *et al.*, Applied Nanoscience **12**, 2151 (2022) [217].
Moreover, different substrates could open an exciting path for investigating the formation of two- and low-dimensional Xenes shortly after.

Chapter

Bibliography

[1] I. M. Ross, *The invention of the transistor*, Proceedings of the IEEE **86**, 7 (1998).

[2] G. E. Moore, *Cramming more components onto integrated circuits*, Electronics **38**, 114 (1965).

[3] T. N. Theis and H.-S. P. Wong, *The End of Moore's Law: A New Beginning for Information Technology*, Computing in Science & Engineering **19**, 41 (2017).

[4] S. B. Desai, S. R. Madhvapathy, A. B. Sachid, J. P. Llinas, Q. Wang, G. H. Ahn, G. Pitner, M. J. Kim, J. Bokor, C. Hu, H.-S. P. Wong, and A. Javey, *MoS_2 transistors with 1-nanometer gate lengths*, Science **354**, 99 (2016).

[5] D. Akinwande, C. Huyghebaert, C.-H. Wang, M. I. Serna, S. Goossens, L.-J. Li, H. S. P. Wong, and F. H. L. Koppens, *Graphene and two-dimensional materials for silicon technology*, Nature **573**, 507 (2019).

[6] K. S. Novoselov, A. K. Geim, S. V. Morozov, D. Jiang, Y. Zhang, S. V. Dubonos, I. V. Grigorieva, and A. A. Firsov, *Electric Field Effect in Atomically Thin Carbon Films*, Science **306**, 666 (2004).

[7] P. R. Wallace, *The Band Theory of Graphite*, Physical Review **71**, 622 (1947).

[8] G. Fiori, F. Bonaccorso, G. Iannaccone, T. Palacios, D. Neumaier, A. Seabaugh, S. K. Banerjee, and L. Colombo, *Electronics based on two-dimensional materials*, Nature Nanotechnology **9**, 768 (2014).

[9] A. K. Geim and K. S. Novoselov, *The rise of graphene*, Nature Materials **6**, 183 (2007).

[10] K. S. Novoselov, A. K. Geim, S. V. Morozov, D. Jiang, M. I. Katsnelson, I. V. Grigorieva, S. V. Dubonos, and A. A. Firsov, *Two-dimensional gas of massless Dirac fermions in graphene*, Nature **438**, 197 (2005).

[11] Y.-M. Lin, C. Dimitrakopoulos, K. A. Jenkins, D. B. Farmer, H.-Y. Chiu, A. Grill, and P. Avouris, *100-GHz Transistors from Wafer-Scale Epitaxial Graphene*, Science **327**, 662 (2010).

[12] K. Takeda and K. Shiraishi, *Theoretical possibility of stage corrugation in Si and Ge analogs of graphite*, Physical Review B **50**, 14916 (1994).

[13] S. Cahangirov, M. Topsakal, E. Aktürk, H. Şahin, and S. Ciraci, *Two- and One-Dimensional Honeycomb Structures of Silicon and Germanium*, Physical Review Letters **102**, 236804 (2009).

[14] P. Vogt, P. De Padova, C. Quaresima, J. Avila, E. Frantzeskakis, M. C. Asensio, A. Resta, B. Ealet, and G. Le Lay, *Silicene: Compelling Experimental Evidence for Graphenelike Two-Dimensional Silicon*, Physical Review Letters **108**, 155501 (2012).

[15] M. E. Dávila, L. Xian, S. Cahangirov, A. Rubio, and G. L. Lay, *Germanene: a novel two-dimensional germanium allotrope akin to graphene and silicene*, New Journal of Physics **16**, 095002 (2014).

[16] A. Molle, J. Goldberger, M. Houssa, Y. Xu, S.-C. Zhang, and D. Akinwande, *Buckled two-dimensional Xene sheets*, Nature Materials **16**, 163 (2017).

[17] C. Liu, H. Chen, S. Wang, Q. Liu, Y.-G. Jiang, D. W. Zhang, M. Liu, and P. Zhou, *Two-dimensional materials for next-generation computing technologies*, Nature Nanotechnology **15**, 545 (2020).

[18] Y. Liu, X. Duan, H.-J. Shin, S. Park, Y. Huang, and X. Duan, *Promises and prospects of two-dimensional transistors*, Nature **591**, 43 (2021).

[19] K. S. Novoselov, V. I. Falko, L. Colombo, P. R. Gellert, M. G. Schwab, and K. Kim, *A roadmap for graphene*, Nature **490**, 192 (2012).

[20] L. Tao, E. Cinquanta, D. Chiappe, C. Grazianetti, M. Fanciulli, M. Dubey, A. Molle, and D. Akinwande, *Silicene field-effect transistors operating at room temperature*, Nature Nanotechnology **10**, 227 (2015).

[21] B. N. Madhushankar, A. Kaverzin, T. Giousis, G. Potsi, D. Gournis, P. Rudolf, G. R. Blake, C. H. van der Wal, and B. J. van Wees, *Electronic properties of germanane field-effect transistors*, 2D Materials **4**, 021009 (2017).

[22] Y. Katayama, R. Yamauchi, Y. Yasutake, S. Fukatsu, and K. Ueno, *Ambipolar transistor action of germanane electric double layer transistor*, Applied Physics Letters **115**, 122101 (2019).

[23] S. Saxena, R. P. Chaudhary, and S. Shukla, *Stanene: Atomically Thick Free-standing Layer of 2D Hexagonal Tin*, Scientific Reports **6**, 31073 (2016).

[24] J. Yuhara, B. He, N. Matsunami, M. Nakatake, and G. Le Lay, *Graphene's Latest Cousin: Plumbene Epitaxial Growth on a "Nano WaterCube"*, Advanced Materials **31**, 1901017 (2019).

[25] V. Kochat, A. Samanta, Y. Zhang, S. Bhowmick, P. Manimunda, S. A. S. Asif, A. S. Stender, R. Vajtai, A. K. Singh, C. S. Tiwary, and P. M. Ajayan, *Atomically thin gallium layers from solid-melt exfoliation*, Science Advances **4**, e1701373.

[26] L. Li, Y. Yu, G. J. Ye, Q. Ge, X. Ou, H. Wu, D. Feng, X. H. Chen, and Y. Zhang, *Black phosphorus field-effect transistors*, Nature Nanotechnology **9**, 372 (2014).

[27] Z. Cheng, T. Zhao, and H. Zeng, *2D Material-Based Photodetectors for Infrared Imaging*, Small Science **2**, 2100051 (2022).

[28] Z.-L. Lei and B. Guo, *2D Material-Based Optical Biosensor: Status and Prospect*, Advanced Science **9**, 2102924 (2022).

[29] S. Wang, S. Zhao, X. Guo, and G. Wang, *2D Material-Based Heterostructures for Rechargeable Batteries*, Advanced Energy Materials **12**, 2100864 (2022).

[30] S. Venkateshalu and A. N. Grace, *MXenes - A new class of 2D layered materials: Synthesis, properties, applications as supercapacitor electrode and beyond*, Applied Materials Today **18**, 100509 (2020).

[31] A. Zia, Z.-P. Cai, A. B. Naveed, J.-S. Chen, and K.-X. Wang, *MXene, Silicene and Germanene: Preparation and Energy Storage Applications*, Materials Today Energy 101144 (2022).

[32] L. Jia, J. Wu, Y. Zhang, Y. Qu, B. Jia, Z. Chen, and D. J. Moss, *Fabrication Technologies for the On-Chip Integration of 2D Materials*, Small Methods **6**, 2101435 (2022).

[33] K. M. Wyss, D. X. Luong, and J. M. Tour, *Large-Scale Syntheses of 2D Materials: Flash Joule Heating and Other Methods*, Advanced Materials **34**, 2106970 (2022).

[34] T. Vincent, J. Liang, S. Singh, E. G. Castanon, X. Zhang, A. McCreary, D. Jariwala, O. Kazakova, and Z. Y. Al Balushi, *Opportunities in electrically tunable 2D materials beyond graphene: Recent progress and future outlook*, Applied Physics Reviews **8**, 041320 (2021).

[35] L. Li, S.-z. Lu, J. Pan, Z. Qin, Y.-q. Wang, Y. Wang, G.-y. Cao, S. Du, and H.-J. Gao, *Buckled Germanene Formation on Pt(111)*, Advanced Materials **26**, 4820 (2014).

[36] L. Chen, C.-C. Liu, B. Feng, X. He, P. Cheng, Z. Ding, S. Meng, Y. Yao, and K. Wu, *Evidence for Dirac Fermions in a Honeycomb Lattice Based on Silicon*, Physical Review Letters **109**, 056804 (2012).

[37] P. De Padova, P. Vogt, A. Resta, J. Avila, I. Razado-Colambo, C. Quaresima, C. Ottaviani, B. Olivieri, T. Bruhn, T. Hirahara, T. Shirai, S. Hasegawa, M. Carmen Asensio, and G. Le Lay, *Evidence of Dirac fermions in multilayer silicene*, Applied Physics Letters **102**, 163106 (2013).

[38] Z.-X. Guo, S. Furuya, J.-i. Iwata, and A. Oshiyama, *Absence and presence of Dirac electrons in silicene on substrates*, Physical Review B **87**, 235435 (2013).

[39] R. Quhe, Y. Yuan, J. Zheng, Y. Wang, Z. Ni, J. Shi, D. Yu, J. Yang, and J. Lu, *Does the Dirac Cone Exist in Silicene on Metal Substrates?*, Scientific Reports **4**, 5476 (2014).

[40] S. K. Mahatha, P. Moras, V. Bellini, P. M. Sheverdyaeva, C. Struzzi, L. Petaccia, and C. Carbone, *Silicene on Ag(111): A honeycomb lattice without Dirac bands*, Physical Review B **89**, 201416 (2014).

[41] Y. Wang, J. Li, J. Xiong, Y. Pan, M. Ye, Y. Guo, H. Zhang, R. Quhe, and J. Lu, *Does the Dirac cone of germanene exist on metal substrates?*, Physical Chemistry Chemical Physics **18**, 19451 (2016).

[42] J. Zhuang, C. Liu, Z. Zhou, G. Casillas, H. Feng, X. Xu, J. Wang, W. Hao, X. Wang, S. X. Dou, Z. Hu, and Y. Du, *Dirac signature in germanene on semiconducting substrate*, Advanced Science **5**, 1800207 (2018).

[43] J. Deng, G. Ablat, Y. Yang, X. Fu, Q. Wu, P. Li, L. Zhang, A. Safaei, L. Zhang, and Z. Qin, *Two-dimensional germanium islands with Dirac signature on Ag2Ge surface alloy*, Journal of Physics: Condensed Matter **33**, 225001 (2021).

[44] X.-S. Ye, Z.-G. Shao, H. Zhao, L. Yang, and C.-L. Wang, *Intrinsic carrier mobility of germanene is larger than graphene's: first-principle calculations*, RSC Advances **4**, 21216 (2014).

[45] Z. Ni, Q. Liu, K. Tang, J. Zheng, J. Zhou, R. Qin, Z. Gao, D. Yu, and J. Lu, *Tunable Bandgap in Silicene and Germanene*, Nano Letters **12**, 113 (2012).

[46] N. Gao, H. Liu, S. Zhou, Y. Bai, and J. Zhao, *Interaction between Post-Graphene Group-IV Honeycomb Monolayers and Metal Substrates: Implication for Synthesis and Structure Control*, The Journal of Physical Chemistry C **121**, 5123 (2017).

[47] A. J. Mannix, B. Kiraly, M. C. Hersam, and N. P. Guisinger, *Synthesis and chemistry of elemental 2D materials*, Nature Reviews Chemistry **1**, 0014 (2017).

[48] Z. Dai, L. Liu, and Z. Zhang, *Strain Engineering of 2D Materials: Issues and Opportunities at the Interface*, Advanced Materials **31**, 1805417 (2019).

[49] Y. Wu, L. Wang, H. Li, Q. Dong, and S. Liu, *Strain of 2D materials via substrate engineering*, Chinese Chemical Letters **33**, 153 (2022).

[50] M. X. Chen, Z. Zhong, and M. Weinert, *Designing substrates for silicene and germanene: First-principles calculations*, Physical Review B **94**, 075409 (2016).

[51] A. Acun, L. Zhang, P. Bampoulis, M. Farmanbar, A. van Houselt, A. N. Rudenko, M. Lingenfelder, G. Brocks, B. Poelsema, M. I. Katsnelson, and H. J. W. Zandvliet, *Germanene: the germanium analogue of graphene*, Journal of Physics: Condensed Matter **27**, 443002 (2015).

[52] A. Nijamudheen, R. Bhattacharjee, S. Choudhury, and A. Datta, *Electronic and Chemical Properties of Germanene: The Crucial Role of Buckling*, The Journal of Physical Chemistry C **119**, 3802 (2015).

[53] C.-C. Liu, W. Feng, and Y. Yao, *Quantum Spin Hall Effect in Silicene and Two-Dimensional Germanium*, Physical Review Letters **107**, 076802 (2011).

[54] R. Stephan, M. Derivaz, M.-C. Hanf, D. Dentel, N. Massara, A. Mehdaoui, P. Sonnet, and C. Pirri, *Tip-Induced Switch of Germanene Atomic Structure*, The Journal of Physical Chemistry Letters **8**, 4587 (2017).

[55] G. Iannaccone, F. Bonaccorso, L. Colombo, and G. Fiori, *Quantum engineering of transistors based on 2D materials heterostructures*, Nature Nanotechnology **13**, 183 (2018).

[56] H. Oughaddou, B. Aufray, and J. Gay, *Ge/Ag (111): surface alloy of a semiconductor on a metal*, Surface Review and Letters **6**, 929 (1999).

[57] H. Oughaddou, S. Sawaya, J. Goniakowski, B. Aufray, G. Le Lay, J. M. Gay, G. Tréglia, J. P. Bibérian, N. Barrett, C. Guillot, A. Mayne, and G. Dujardin, *Ge/Ag(111) semiconductor-on-metal growth: Formation of an Ag_2Ge surface alloy*, Physical Review B **62**, 16653 (2000).

[58] E. Golias, E. Xenogiannopoulou, D. Tsoutsou, P. Tsipas, S. A. Giamini, and A. Dimoulas, *Surface electronic bands of submonolayer Ge on Ag(111)*, Physical Review B **88**, 075403 (2013).

[59] Y. Liu, J. Zhuang, C. Liu, J. Wang, X. Xu, Z. Li, J. Zhong, and Y. Du, *Role of Atomic Interaction in Electronic Hybridization in Two-Dimensional Ag_2Ge Nanosheets*, The Journal of Physical Chemistry C **121**, 16754 (2017).

[60] K. Zhang, R. Bernard, Y. Borensztein, H. Cruguel, and G. Prévot, *Growth of germanium-silver surface alloys followed by in situ scanning tunneling microscopy: Absence of germanene formation*, Physical Review B **102**, 125418 (2020).

[61] M. Rahman, T. Nakagawa, and S. Mizuno, *Germanene: Experimental study for graphene like two dimensional germanium*, Evergreen **1**, 25 (2014).

[62] K. Zhang, D. Sciacca, A. Coati, R. Bernard, Y. Borensztein, P. Diener, B. Grandidier, I. Lefebvre, M. Derivaz, C. Pirri, and G. Prévot, *Resolving the structure of the striped Ge layer on Ag(111): Ag_2Ge surface alloy with alternate fcc and hcp domains*, Physical Review B **104**, 155403 (2021).

[63] C.-H. Lin, A. Huang, W. W. Pai, W.-C. Chen, T.-Y. Chen, T.-R. Chang, R. Yukawa, C.-M. Cheng, C.-Y. Mou, I. Matsuda, T.-C. Chiang, H.-T. Jeng, and S.-J. Tang, *Single-layer dual germanene phases on Ag(111)*, Physical Review Materials **2**, 024003 (2018).

[64] H. Oughaddou, A. Mayne, B. Aufray, J. P. Bibérian, G. Le Lay, B. Ealet, G. Dujardin, and A. Kara, *Germanium Adsorption on Ag(111): An AES-LEED and STM Study*, Journal of Nanoscience and Nanotechnology **7**, 3189 (2007).

[65] J. Yuhara, H. Shimazu, K. Ito, A. Ohta, M. Araidai, M. Kurosawa, M. Nakatake, and G. Le Lay, *Germanene Epitaxial Growth by Segregation through Ag(111) Thin Films on Ge(111)*, ACS Nano **12**, 11632 (2018).

[66] T.-Y. Chen, D. Mikolas, S. Chiniwar, A. Huang, C.-H. Lin, C.-M. Cheng, C.-Y. Mou, H.-T. Jeng, W. W. Pai, and S.-J. Tang, *Germanene structure enhancement by adjacent insoluble domains of lead*, Physical Review Research **3**, 033138 (2021).

[67] S. Mizuno, A. Ohta, T. Suzuki, H. Kageshima, J. Yuhara, and H. Hibino, *Correlation between structures and vibration properties of germanene grown by Ge segregation*, Applied Physics Express **14**, 125501 (2021).

[68] N. W. Ashcroft and N. D. Mermin, *Solid state physics*, Holt, Rinehart and Winston, New York, London, 4 ed. (1976).

[69] K. Oura, V. Lifshits, A. Saranin, A. Zotov, and M. Katayama, *Surface science: an introduction*, Springer Berlin, Heidelberg, New York, 1 ed. (2003).

[70] M. Henzler and W. Göpel, *Oberflächenphysik des Festkörpers*, Vieweg+Teubner Verlag Wiesbaden, Stuttgart, 2 ed. (1991).

[71] R. Peierls, *Bemerkungen über Umwandlungstemperaturen*, Helvetica Physica Acta **7**, 81 (1934).

[72] L. D. Landau, *Zur Theorie der phasenumwandlungen II*, Physikalische Zeitschrift der Sowjetunion **11**, 26 (1937).

[73] S. Chakravarty and C. Dasgupta, *Absence of crystalline order in two dimensions*, Physical Review B **22**, 369 (1980).

[74] N. D. Mermin, *Crystalline Order in Two Dimensions*, Physical Review **176**, 250 (1968).

[75] B. J. Alder and T. E. Wainwright, *Phase Transition in Elastic Disks*, Physical Review **127**, 359 (1962).

[76] F. Iacopi, J. Boeckl, and C. Jagadish, *Preface*, in *2D Materials*, *Semiconductors and Semimetals*, vol. 95, edited by F. Iacopi, J. J. Boeckl, and C. Jagadish, Elsevier, xi–xviii (2016).

[77] G. Yang, L. Li, W. B. Lee, and M. C. Ng, *Structure of graphene and its disorders: a review*, Science and Technology of Advanced Materials **19**, 613 (2018).

[78] S. Balendhran, S. Walia, H. Nili, S. Sriram, and M. Bhaskaran, *Elemental Analogues of Graphene: Silicene, Germanene, Stanene, and Phosphorene*, Small **11**, 640 (2015).

[79] C. Grazianetti, E. Cinquanta, and A. Molle, *Two-dimensional silicon: the advent of silicene*, 2D Materials **3**, 012001 (2016).

[80] A. Molle, C. Grazianetti, L. Tao, D. Taneja, M. H. Alam, and D. Akinwande, *Silicene, silicene derivatives, and their device applications*, Chemical Society Reviews **47**, 6370 (2018).

[81] Z. Huang, H. Liu, R. Hu, H. Qiao, H. Wang, Y. Liu, X. Qi, and H. Zhang, *Structures, properties and application of 2D monoelemental materials (Xenes) as graphene analogues under defect engineering*, Nano Today **35**, 100906 (2020).

[82] A. J. Mannix, X.-F. Zhou, B. Kiraly, J. D. Wood, D. Alducin, B. D. Myers, X. Liu, B. L. Fisher, U. Santiago, J. R. Guest, M. J. Yacaman, A. Ponce, A. R. Oganov, M. C. Hersam, and N. P. Guisinger, *Synthesis of borophenes: Anisotropic, two-dimensional boron polymorphs*, Science **350**, 1513 (2015).

[83] M. Fortin-Deschênes, O. Waller, T. O. Menteş, A. Locatelli, S. Mukherjee, F. Genuzio, P. L. Levesque, A. Hébert, R. Martel, and O. Moutanabbir, *Synthesis of Antimonene on Germanium*, Nano Letters **17**, 4970 (2017).

[84] Y. Wang, G. Qiu, R. Wang, S. Huang, Q. Wang, Y. Liu, Y. Du, W. A. Goddard, M. J. Kim, X. Xu, P. D. Ye, and W. Wu, *Field-effect transistors made from solution-grown two-dimensional tellurene*, Nature Electronics **1**, 228 (2018).

[85] X. Zhang, Y. Liu, and Q. Huang, *Stable halogen 2D materials: the case of iodine and astatine*, Journal of Physics: Condensed Matter **32**, 335301 (2020).

[86] M. A. B. Hamid, K. T. Chan, C. H. Raymond Ooi, H. Zainuddin, N. Mohd Shah, and N. N. Shahrol Nidzam, *Structural stability and electronic properties of graphene/germanene heterobilayer*, Results in Physics **28**, 104545 (2021).

[87] Q. Pang, H. Xin, D. li Gao, J. Zhao, R. peng Chai, and Y. ling Song, *Strain effect on the electronic and optical properties of Germanene/MoS_2 heterobilayer*, Materials Today Communications **26**, 101845 (2021).

[88] M. Naguib, V. N. Mochalin, M. W. Barsoum, and Y. Gogotsi, *25th Anniversary Article: MXenes: A New Family of Two-Dimensional Materials*, Advanced Materials **26**, 992 (2014).

[89] A. K. Geim, *Graphene: Status and Prospects*, Science **324**, 1530 (2009).

[90] S. V. Morozov, K. S. Novoselov, M. I. Katsnelson, F. Schedin, D. C. Elias, J. A. Jaszczak, and A. K. Geim, *Giant Intrinsic Carrier Mobilities in Graphene and Its Bilayer*, Physical Review Letters **100**, 016602 (2008).

[91] K. S. Kim, Y. Zhao, H. Jang, S. Y. Lee, J. M. Kim, K. S. Kim, J.-H. Ahn, P. Kim, J.-Y. Choi, and B. H. Hong, *Large-scale pattern growth of graphene films for stretchable transparent electrodes*, Nature **457**, 706 (2009).

[92] A. A. Balandin, S. Ghosh, W. Bao, I. Calizo, D. Teweldebrhan, F. Miao, and C. N. Lau, *Superior Thermal Conductivity of Single-Layer Graphene*, Nano Letters **8**, 902 (2008).

[93] R. Franz and G. Wiedemann, *Ueber die Wärme-Leitungsfähigkeit der Metalle*, Annalen der Physik **165**, 497 (1853).

[94] S. Reich, J. Maultzsch, C. Thomsen, and P. Ordejón, *Tight-binding description of graphene*, Physical Review B **66**, 035412 (2002).

[95] S. Das Sarma, S. Adam, E. H. Hwang, and E. Rossi, *Electronic transport in two-dimensional graphene*, Reviews of Modern Physics **83**, 407 (2011).

[96] T. Wehling, A. Black-Schaffer, and A. Balatsky, *Dirac materials*, Advances in Physics **63**, 1 (2014).

[97] K. S. Novoselov, Z. Jiang, Y. Zhang, S. V. Morozov, H. L. Stormer, U. Zeitler, J. C. Maan, G. S. Boebinger, P. Kim, and A. K. Geim, *Room-Temperature Quantum Hall Effect in Graphene*, Science **315**, 1379 (2007).

[98] J. E. Moore, *The birth of topological insulators*, Nature **464**, 194 (2010).

[99] M. Ezawa, *Monolayer Topological Insulators: Silicene, Germanene, and Stanene*, Journal of the Physical Society of Japan **84**, 121003 (2015).

[100] J. Avila, P. D. Padova, S. Cho, I. Colambo, S. Lorcy, C. Quaresima, P. Vogt, A. Resta, G. L. Lay, and M. C. Asensio, *Presence of gapped silicene-derived band in the prototypical (3 × 3) silicene phase on silver (111) surfaces*, Journal of Physics: Condensed Matter **25**, 262001 (2013).

[101] N. Briggs, S. Subramanian, Z. Lin, X. Li, X. Zhang, K. Zhang, K. Xiao, D. Geohegan, R. Wallace, L.-Q. Chen, M. Terrones, A. Ebrahimi, S. Das, J. Redwing, C. Hinkle, K. Momeni, A. van Duin, V. Crespi, S. Kar, and J. A. Robinson, *A roadmap for electronic grade 2D materials*, 2D Materials **6**, 022001 (2019).

[102] N. R. Glavin, R. Rao, V. Varshney, E. Bianco, A. Apte, A. Roy, E. Ringe, and P. M. Ajayan, *Emerging Applications of Elemental 2D Materials*, Advanced Materials **32**, 1904302 (2020).

[103] S. Cahangirov, H. Sahin, G. Le Lay, and A. Rubio, *Introduction to the Physics of Silicene and other 2D Materials*, Springer Cham, Heidelberg, 1 ed. (2017).

[104] L. C. Lew Yan Voon, E. Sandberg, R. S. Aga, and A. A. Farajian, *Hydrogen compounds of group-IV nanosheets*, Applied Physics Letters **97**, 163114 (2010).

[105] E. Scalise, *Vibrational Properties of Silicene and Germanene*, Springer International Publishing, Cham, 61–93 (2014).

[106] R.-w. Zhang, W.-x. Ji, C.-w. Zhang, S.-s. Li, P. Li, and P.-j. Wang, *New family of room temperature quantum spin Hall insulators in two-dimensional germanene films*, Journal of Materials Chemistry C **4**, 2088 (2016).

[107] Y. Xu, B. Yan, H.-J. Zhang, J. Wang, G. Xu, P. Tang, W. Duan, and S.-C. Zhang, *Large-Gap Quantum Spin Hall Insulators in Tin Films*, Physical Review Letters **111**, 136804 (2013).

[108] X.-L. Yu, L. Huang, and J. Wu, *From a normal insulator to a topological insulator in plumbene*, Physical Review B **95**, 125113 (2017).

[109] D. K. Das, J. Sarkar, and S. Singh, *Effect of sample size, temperature and strain velocity on mechanical properties of plumbene by tensile loading along longitudinal direction: A molecular dynamics study*, Computational Materials Science **151**, 196 (2018).

[110] A. G. Shard, *Detection limits in XPS for more than 6000 binary systems using Al and Mg K X-rays*, Surface and Interface Analysis **46**, 175 (2014).

[111] J. Osterwalder, *Electron Based Methods: 3.2.2 Photoelectron Spectroscopy and Diffraction*, 151–214 (2013).

[112] A.-E. Becquerel, *Recherches sur les effets de la radiation chimique de la lumiere solaire au moyen des courants electriques*, Comptes rendus de l'Académie des sciences **9**, 1 (1839).

[113] H. Hertz, *Ueber einen Einfluss des ultravioletten Lichtes auf die electrische Entladung*, Annalen der Physik **267**, 983 (1887).

[114] W. Hallwachs, *Ueber den Einfluss des Lichtes auf electrostatisch geladene Körper*, Annalen der Physik **269**, 301 (1888).

[115] P. Lenard, *Ueber die lichtelektrische Wirkung*, Annalen der Physik **313**, 149 (1902).

[116] A. Einstein, *Über einen die Erzeugung und Verwandlung des Lichtes betreffenden heuristischen Gesichtspunkt*, Annalen der Physik **322**, 132 (1905).

[117] R. A. Millikan, *A Direct Photoelectric Determination of Planck's "h"*, Physical Review **7**, 355 (1916).

[118] S. Hüfner, *Photoelectron spectroscopy: principles and applications*, Springer Berlin, Heidelberg, New York, 3 ed. (2003).

[119] W. Demtröder, *Experimentalphysik 4*, Springer Spektrum Berlin, Heidelberg, Heidelberg, 4 ed. (2014).

[120] S. Suga, A. Sekiyama, and C. Tusche, *Photoelectron Spectroscopy: Bulk and Surface Electronic Structures*, Springer Cham, Cham, 2 ed. (2021).

[121] W. Schattke, *PHOTOEMISSION WITHIN AND BEYOND THE ONE-STEP MODEL*, Progress in Surface Science **54**, 211 (1997).

[122] J. Pendry, *Theory of photoemission*, Surface Science **57**, 679 (1976).

[123] L. Hedin, J. Michiels, and J. Inglesfield, *Transition from the adiabatic to the sudden limit in core-electron photoemission*, Physical Review B **58**, 15565 (1998).

[124] F. De Groot and A. Kotani, *Core level spectroscopy of solids*, CRC press, Boca Raton, 1 ed. (2008).

[125] P. Auger, *Sur l'effet photoélectrique composé*, Journal de Physique et le Radium **6**, 205 (1925).

[126] L. Meitner, *Über dieβ-Strahl-Spektra und ihren Zusammenhang mit der γ-Strahlung*, Zeitschrift für Physik **11**, 35 (1922).

[127] J. F. W. Herschel, *No. I. - On a Case of Superficial Colour presented by a homogeneous liquid internally colourless*, Philosophical Transactions of the Royal Society of London **135**, 143 (1845).

[128] G. G. Stokes, *XXX. On the change of refrangibility of light*, Philosophical Transactions of the Royal Society of London **142**, 463 (1852).

[129] M. O. Krause, *Atomic radiative and radiationless yields for K and L shells*, Journal of Physical and Chemical Reference Data **8**, 307 (1979).

[130] J. Yeh and I. Lindau, *Atomic subshell photoionization cross sections and asymmetry parameters:* $1 \leq Z \leq 103$, Atomic Data and Nuclear Data Tables **32**, 1 (1985).

[131] H. Ibach, *Electron Spectroscopy for Surface Analysis*, Springer Berlin, Heidelberg, 1 ed. (1977).

[132] M. P. Seah and W. A. Dench, *Quantitative electron spectroscopy of surfaces: A standard data base for electron inelastic mean free paths in solids*, Surface and Interface Analysis **1**, 2 (1979).

[133] H. Shinotsuka, S. Tanuma, C. Powell, and D. Penn, *Calculations of electron inelastic mean free paths. X. Data for 41 elemental solids over the 50 eV to 200 keV range with the relativistic full Penn algorithm*, Surface and Interface Analysis **47**, 871 (2015).

[134] A. Jablonski and C. Powell, *Relationships between electron inelastic mean free paths, effective attenuation lengths, and mean escape depths*, Journal of Electron Spectroscopy and Related Phenomena **100**, 137 (1999).

[135] D. Son, S. Cho, J. Nam, H. Lee, and M. Kim, *X-ray-Based Spectroscopic Techniques for Characterization of Polymer Nanocomposite Materials at a Molecular Level*, Polymers **12** (2020).

[136] P. Van der Heide, *X-ray photoelectron spectroscopy: an introduction to principles and practices*, John Wiley & Sons, Ltd, Hoboken, New Jersey, 10 ed. (2012).

[137] P. Streubel, R. Hesse, L. Makhova, J. Schindelka, and R. Denecke, *A Practicable Method for Thickness Estimation of Ultrathin Layers from XPS Data with UNIFIT 2011*, Tech. rep., Wilhelm-Ostwald-Institut für Physikalische und Theoretische Chemie, Universität Leipzig, Leipzig (2011).

[138] *NIST X-ray Photoelectron Spectroscopy Database, NIST Standard Reference Database Number 20, National Institute of Standards and Technology, Gaithersburg MD, 20899*, https://doi.org/10.18434/T4T88K (2000), retrieved: 2022-09-28.

[139] R. Hesse, *Unifit for Windows: Spectrum Processing, Analysis and Presentation Software for XPS, XAS, AES and RAMAN Spectroscopy*, Unifit Scientific Software GmbH, Leipzig, Germany (2022).

[140] W. Demtröder, *Experimentalphysik 3*, Springer Spektrum Berlin, Heidelberg, Heidelberg, 5 ed. (2016).

[141] K. Siegbahn, *Electron spectroscopy for atoms, molecules, and condensed matter*, Reviews of Modern Physics **54**, 709 (1982).

[142] J. F. Watts and J. Wolstenholme, *An Introduction to Surface Analysis by XPS and AES*, John Wiley & Sons, Ltd, Hoboken, New Jersey, 2 ed. (2019).

[143] U. Gelius, E. Basilier, S. Svensson, T. Bergmark, and K. Siegbahn, *A high resolution ESCA instrument with X-ray monochromator for gases and solids*, Journal of Electron Spectroscopy and Related Phenomena **2**, 405 (1973).

[144] U. Gelius, P. F. Hedén, J. Hedman, B. J. Lindberg, R. Manne, R. Nordberg, C. Nordling, and K. Siegbahn, *Molecular Spectroscopy by Means of ESCA III.Carboncompounds*, Physica Scripta **2**, 70 (1970).

[145] M. Rocca, T. S. Rahman, and L. Vattuone, *Springer Handbook of Surface Science*, Springer Cham, Cham, 1 ed. (2020).

[146] J. Moore, C. Stanitski, and P. Jurs, *Principles of chemistry: the molecular science*, Brooks/Cole, Cengage Learning, Belmont, CA (2009).

[147] W. Egelhoff, *Core-level binding-energy shifts at surfaces and in solids*, Surface Science Reports **6**, 253 (1987).

[148] D. A. Shirley, *High-Resolution X-Ray Photoemission Spectrum of the Valence Bands of Gold*, Physical Review B **5**, 4709 (1972).

[149] R. Hesse, M. Weiß, R. Szargan, P. Streubel, and R. Denecke, *Comparative study of the modelling of the spectral background of photoelectron spectra with the Shirley and improved Tougaard methods*, Journal of Electron Spectroscopy and Related Phenomena **186**, 44 (2013).

[150] S. Tougaard and B. Jørgensen, *Absolute background determination in XPS*, Surface and Interface Analysis **7**, 17 (1985).

[151] R. Hesse, M. Weiß, R. Szargan, P. Streubel, and R. Denecke, *Improved peak-fit procedure for XPS measurements of inhomogeneous samples - Development of the advanced Tougaard background method*, Journal of Electron Spectroscopy and Related Phenomena **205**, 29 (2015).

[152] M. Schmid, H.-P. Steinrück, and J. M. Gottfried, *A new asymmetric Pseudo-Voigt function for more efficient fitting of XPS lines*, Surface and Interface Analysis **47**, 1080 (2015).

[153] R. Hesse, P. Streubel, and R. Szargan, *Product or sum: comparative tests of Voigt, and product or sum of Gaussian and Lorentzian functions in the fitting of synthetic Voigt-based X-ray photoelectron spectra*, Surface and Interface Analysis **39**, 381 (2007).

[154] G. H. Major, N. Fairley, P. M. A. Sherwood, M. R. Linford, J. Terry, V. Fernandez, and K. Artyushkova, *Practical guide for curve fitting in x-ray photoelectron spectroscopy*, Journal of Vacuum Science & Technology A **38**, 061203 (2020).

[155] J. Liu, H. Zhang, Y. Li, and Z. Liu, *Disorder in Aqueous Solutions and Peak Broadening in X-ray Photoelectron Spectroscopy*, The Journal of Physical Chemistry B **122**, 10600 (2018), pMID: 30359023.

[156] S. Dreiner, *Untersuchung von Ober- und Grenzflächen mittels niederenergetischer Photoelektronenbeugung*, Ph.D. thesis, TU Dortmund University, Dortmund, Germany (2002).

[157] B. Armstrong, *Spectrum line profiles: The Voigt function*, Journal of Quantitative Spectroscopy and Radiative Transfer **7**, 61 (1967).

[158] S. Hüfner and G. K. Wertheim, *Core-line asymmetries in the x-ray-photoemission spectra of metals*, Physical Review B **11**, 678 (1975).

[159] S. Doniach and M. Sunjic, *Many-electron singularity in X-ray photoemission and X-ray line spectra from metals*, Journal of Physics C: Solid State Physics **3**, 285 (1970).

[160] X. Cui, C. Wang, A. Argondizzo, S. Garrett-Roe, B. Gumhalter, and H. Petek, *Transient excitons at metal surfaces*, Nature Physics **10**, 505 (2014).

[161] G. Greczynski and L. Hultman, *X-ray photoelectron spectroscopy: Towards reliable binding energy referencing*, Progress in Materials Science **107**, 100591 (2020).

[162] B. V. Crist, *XPS in industry - Problems with binding energies in journals and binding energy databases*, Journal of Electron Spectroscopy and Related Phenomena **231**, 75 (2019).

[163] R. Hesse, T. Chassé, P. Streubel, and R. Szargan, *Error estimation in peak-shape analysis of XPS core-level spectra using UNIFIT 2003: how significant are the results of peak fits?*, Surface and Interface Analysis **36**, 1373 (2004).

[164] B. Singh, R. Hesse, and M. R. Linford, *Good practices for XPS (and other types of) peak fitting*, Vacuum Technology & Coating **12**, 25 (2015).

[165] R. Andrae, T. Schulze-Hartung, and P. Melchior, *Dos and don'ts of reduced chi-squared* (2010).

[166] D. W. Marquardt, *An Algorithm for Least-Squares Estimation of Nonlinear Parameters*, Journal of the Society for Industrial and Applied Mathematics **11**, 431 (1963).

[167] S. Tougaard, *Practical guide to the use of backgrounds in quantitative XPS*, Journal of Vacuum Science & Technology A **39**, 011201 (2021).

[168] K. Siegbahn, U. Gelius, H. Siegbahn, and E. Olson, *Angular Distribution of Electrons in ESCA Spectra from a Single Crystal*, Physica Scripta **1**, 272 (1970).

[169] C. Fadley and S. Bergström, *Angular distribution of photoelectrons from a metal single crystal*, Physics Letters A **35**, 375 (1971).

[170] S. Kono, C. S. Fadley, N. F. T. Hall, and Z. Hussain, *Azimuthal Anisotropy in Deep Core-Level X-Ray Photoemission from an Adsorbed Atom: Oxygen on Copper(001)*, Physical Review Letters **41**, 117 (1978).

[171] M. Scheffler, K. Kambe, and F. Forstmann, *Angle resolved photoemission from adsorbates: Theoretical considerations of polarization effects and symmetry*, Solid State Communications **25**, 93 (1978).

[172] C. S. Fadley, *Diffraction and holography with photoelectrons and Auger electrons: some new directions*, Surface Science Reports **19**, 231 (1993).

[173] C. Westphal, *The study of the local atomic structure by means of X-ray photoelectron diffraction*, Surface Science Reports **50**, 1 (2003).

[174] D. P. Woodruff and A. M. Bradshaw, *Adsorbate structure determination on surfaces using photoelectron diffraction*, Reports on Progress in Physics **57**, 1029 (1994).

[175] F. J. García de Abajo, M. A. Van Hove, and C. S. Fadley, *Multiple scattering of electrons in solids and molecules: A cluster-model approach*, Physical Review B **63**, 075404 (2001).

[176] M.-L. Xu, J. J. Barton, and M. A. Van Hove, *Electron scattering by atomic chains: Multiple-scattering effects*, Physical Review B **39**, 8275 (1989).

[177] J. B. Pendry, *Reliability factors for LEED calculations*, Journal of Physics C: Solid State Physics **13**, 937 (1980).

[178] J. C. Slater, *Wave Functions in a Periodic Potential*, Physical Review **51**, 846 (1937).

[179] C. J. Powell and A. Jablonski, *Evaluation of electron inelastic mean free paths for selected elements and compounds†*, Surface and Interface Analysis **29**, 108 (2000).

[180] R. Döll and M. Van Hove, *Global optimization in LEED structure determination using genetic algorithms*, Surface Science **355**, L393 (1996).

[181] M. L. Viana, R. D. Muiño, E. A. Soares, M. A. V. Hove, and V. E. de Carvalho, *Global search in photoelectron diffraction structure determination using genetic algorithms*, Journal of Physics: Condensed Matter **19**, 446002 (2007).

[182] T. Lühr, *Messung und Simulation von XPD Mustern der Si(110)/SiO_2-Grenzschicht*, Diploma thesis, TU Dortmund University (2009).

[183] M. A. van Hove, W. H. Weinberg, and C.-M. Chan, *Low-energy electron diffraction: experiment, theory and surface structure determination*, Springer Berlin, Heidelberg, Heidelberg, 1 ed. (1986).

[184] SPECS Surface Nano Analysis GmbH, Berlin, Germany, *IQE 12/38, Ion Source*, v2.2 ed. (2013).

[185] FOCUS GmbH, Huenstetten-Kesselbach, Germany, *EFM Evaporators, Electron Beam Evaporators for Ultra-Pure Submonolayer and Multilayer Thin Film Growth*, rev. 9 ed. (2019).

[186] G. Sauerbrey, *Verwendung von Schwingquarzen zur Wägung dünner Schichten und zur Mikrowägung*, Zeitschrift für Physik **155**, 206 (1959).

[187] A. G. Shard and B. P. Reed, *Al Kα XPS reference spectra of polyethylene for all instrument geometries*, Journal of Vacuum Science & Technology A **38**, 063209 (2020).

[188] J. Osterwalder, M. Sagurton, P. Orders, C. Fadley, B. Hermsmeier, and D. Friedman, *Electron trajectory analysis of the spherical-sector electrostatic spectrometer: focussing properties and multichannel detection capability*, Journal of Electron Spectroscopy and Related Phenomena **48**, 55 (1989).

[189] H. Sjuts, *Channel Electron Multipliers Series KBL & Complete Measurement Systems*, http://www.sjuts.com/index_english.html (2022), retrieved: 2022-09-28.

[190] S. Mobilio, F. Boscherini, and C. Meneghini, *Synchrotron Radiation: Basics, Methods and Applications*, Springer Berlin, Heidelberg, Heidelberg, 1 ed. (2015).

[191] J. B. Parise and J. Brown, Gordon E., *New Opportunities at Emerging Facilities*, Elements **2**, 37 (2006).

[192] M. Höner, *Investigation of transient processes at the DELTA electron storage ring using a digital bunch-by-bunch feedback system*, Ph.D. thesis, TU Dortmund University (2015).

[193] Lightsources.org, *Light sources of the world*, https://lightsources.org/lightsources-of-the-world/ (2022), retrieved: 2022-09-28.

[194] C. Westphal, U. Berges, S. Dreiner, R. Follath, M. Krause, F. Schäfers, D. Schirmer, and M. Schürmann, *The plane-grating monochromator beamline at the U55 undulator for surface and interface studies at DELTA*, Journal of Electron Spectroscopy and Related Phenomena **144-147**, 1117 (2005).

[195] J. Yuhara, Y. Fujii, K. Nishino, N. Isobe, M. Nakatake, L. Xian, A. Rubio, and G. Le Lay, *Large area planar stanene epitaxially grown on Ag(1 1 1)*, 2D Materials **5**, 025002 (2018).

[196] L. Kesper, J. A. Hochhaus, M. Schmitz, M. G. H. Schulte, U. Berges, and C. Westphal, *Tracing the structural evolution of quasi-freestanding germanene on Ag(111)*, Scientific Reports **12**, 7559 (2022).

[197] H. Roloff and H. Neddermeyer, *High-resolution photoemission from Ag(100), Ag(110), and Ag(111)*, Solid State Communications **21**, 561 (1977).

[198] P. S. Wehner, R. S. Williams, S. D. Kevan, D. Denley, and D. A. Shirley, *Valence-band structure of silver along Λ from angle-resolved photoemission*, Physical Review B **19**, 6164 (1979).

[199] G. V. Hansson and S. A. Flodström, *Angular-resolved photoemission from low-index crystal faces of silver - bulk and surface contributions*, Physical Review B **17**, 473 (1978).

[200] C. Godet, D. David, H. Sabbah, S. Ababou-Girard, and F. Solal, *Bulk and surface plasmon excitations in amorphous carbon measured by core-level photoelectron spectroscopy*, Applied Surface Science **255**, 6598 (2009).

[201] J. Leiro, E. Minni, and E. Suoninen, *Study of plasmon structure in XPS spectra of silver and gold*, Journal of Physics F: Metal Physics **13**, 215 (1983).

[202] S. K. Kwon, Z. Nabi, K. Kádas, L. Vitos, J. Kollár, B. Johansson, and R. Ahuja, *Surface energy and stress release by layer relaxation*, Physical Review B **72**, 235423 (2005).

[203] M. Dávila, L. Lew Yan Voon, J. Zhao, and G. Le Lay, *Chapter Four - Elemental Group IV Two-Dimensional Materials Beyond Graphene*, in *2D Materials*, *Semiconductors and Semimetals*, vol. 95, edited by F. Iacopi, J. J. Boeckl, and C. Jagadish, Elsevier, 149–188 (2016).

[204] W. Wang, H. M. Sohail, J. R. Osiecki, and R. I. G. Uhrberg, *Broken symmetry induced band splitting in the* Ag_2Ge *surface alloy on Ag(111)*, Physical Review B **89**, 125410 (2014).

[205] S. Narasimhan and D. Vanderbilt, *Elastic stress domains and the herringbone reconstruction on Au(111)*, Physical Review Letters **69**, 1564 (1992).

[206] M. Lackinger, S. Griessl, W. M. Heckl, and M. Hietschold, *Coronene on Ag(111) Investigated by LEED and STM in UHV*, The Journal of Physical Chemistry B **106**, 4482 (2002).

[207] K. V. Emtsev, F. Speck, T. Seyller, L. Ley, and J. D. Riley, *Interaction, growth, and ordering of epitaxial graphene on SiC{0001} surfaces: A comparative photoelectron spectroscopy study*, Physical Review B **77**, 155303 (2008).

[208] R. Haerle, E. Riedo, A. Pasquarello, and A. Baldereschi, sp^2/sp^3 *hybridization ratio in amorphous carbon from C* 1*s core-level shifts: X-ray photoelectron spectroscopy and first-principles calculation*, Physical Review B **65**, 045101 (2001).

[209] L. Zhang, P. Bampoulis, A. N. Rudenko, Q. Yao, A. van Houselt, B. Poelsema, M. I. Katsnelson, and H. J. W. Zandvliet, *Structural and Electronic Properties of Germanene on* MoS_2, Physical Review Letters **116**, 256804 (2016).

[210] A. Molle, G. Faraone, A. Lamperti, D. Chiappe, E. Cinquanta, C. Martella, E. Bonera, E. Scalise, and C. Grazianetti, *Stability and universal encapsulation of epitaxial Xenes*, Faraday Discussions **227**, 171 (2021).

[211] S. Suzuki, K. K. H. De Silva, M. Yoshimura, and T. Nakayama, *Segregation of metallic germanium atoms at the graphene/metal interface toward germanene growth*, Japanese Journal of Applied Physics **59**, SN1004 (2020).

[212] S. Suzuki, T. Iwasaki, K. K. H. De Silva, S. Suehara, K. Watanabe, T. Taniguchi, S. Moriyama, M. Yoshimura, T. Aizawa, and T. Nakayama, *Direct Growth of Germanene at Interfaces between Van der Waals Materials and Ag(111)*, Advanced Functional Materials **31**, 2007038 (2021).

[213] J. Oh and J. C. Campbell, *Thermal desorption of Ge native oxides and the loss of Ge from the surface*, Journal of Electronic Materials **33**, 364 (2004).

[214] I. Iatsunskyi, M. Kempiński, M. Jancelewicz, K. Załęski, S. Jurga, and V. Smyntyna, *Structural and XPS characterization of ALD* Al_2O_3 *coated porous silicon*, Vacuum **113**, 52 (2015).

[215] P. S. Bagus, G. Pacchioni, and F. Parmigiani, *Surface core-level spectroscopy of Cu(100) and Al(100)*, Physical Review B **43**, 5172 (1991).

[216] J. Yuhara, H. Shimazu, M. Kobayashi, A. Ohta, S. Miyazaki, S. ichi Takakura, M. Nakatake, and G. Le Lay, *Epitaxial growth of massively parallel germanium nanoribbons by segregation through Ag(110) thin films on Ge(110)*, Applied Surface Science **550**, 149236 (2021).

[217] L. Kesper, M. Schmitz, M. G. H. Schulte, U. Berges, and C. Westphal, *Revealing the nano-structures of low-dimensional germanium on Ag(1 1 0) using XPS and XPD*, Applied Nanoscience **12**, 2151 (2022).

Chapter

Publications

Articles

1. Wolfgang Tillmann, David Kokalj, Dominic Stangier, Qingqing Fu, Frank Einar Kruis, Lukas Kesper, Ulf Berges, and Carsten Westphal, *On the synthesis and structural evolution of artificial CrN/TiN nanocomposites*, Applied Surface Science **535**, 147736 (2021).

2. Christopher Kohlmann, Lukas Kesper, Richard Hönig, Takayuki Muro, Yasumasa Takagi, Akira Yasui, and Carsten Westphal, *Hard X-ray Photoelectron Diffraction applied to the system pyrite (FeS_2) for Direct Atom Imaging by means of Chemical Sensitive Photoelectron Holography: proof of principle study*, SPring-8/SACLA Research Report **9**, 195 (2021).

3. Marie Schmitz, Lukas Kesper, Malte G. H. Schulte, Peter Roese, Ulf Berges, and Carsten Westphal, *Surface and interface analysis of a low-dimensional Au-Si surface alloy on Au(110) by means of XPS and XPD*, Journal of Physics: Condensed Matter **33**, 275001 (2021).

4. Wolfgang Tillmann, Nelson Filipe Lopes Dias, Dominic Stangier, Jasper Berndt, Stephan Klemme, Lukas Kesper, Ulf Berges, Carsten Westphal, Carl Arne Thomann, and Jörg Debus, *Rare-earth modified amorphous carbon films: Effects of erbium and gadolinium on the structural evolution and mechanical properties*, Diamond and Related Materials **123**, 108898 (2022).

5. Lukas Kesper, Marie Schmitz, Malte G. H. Schulte, Ulf Berges, and Carsten Westphal, *Revealing the nano-structures of low-dimensional germanium on Ag(1 1 0) using XPS and XPD*, Applied Nanoscience **12**, 2151 (2022).

6. Lukas Kesper, Julian A. Hochhaus, Marie Schmitz, Malte G. H. Schulte, Ulf Berges, and Carsten Westphal, *Tracing the structural evolution of quasi-freestanding germanene on Ag(111)*, Scientific Reports **12**, 7559 (2022).

7. Wolfgang Tillmann, Dominic Stangier, Nelson Filipe Lopes Dias, Lukas Kesper, Ulf Berges, Carsten Westphal, Jasper Berndt-Gerdes, Peter Awakowicz, *On the structure of sputtered transition metal boride PVD coatings*, Materials Letters (manuscript in preparation).

Conference Talks

1. Lukas Kesper, Peter Roese, Karim Shamout, Ulf Berges, and Carsten Westphal, *Investigation of two-dimensional germanium on Ag(110) by means of XPS*, DPG Spring-Meeting 2019, Regensburg, Germany (2019).

2. Lukas Kesper, Christopher Kohlmann, Marie Schmitz, Peter Roese, Malte G. H. Schulte, Ulf Berges, and Carsten Westphal, *XPS-/XPD-studies on the low-dimensional formation of self-assembled germanium on Ag(110)*, 15th DELTA User Meeting, Dortmund, Germany (2019).

3. Lukas Kesper, Christopher Kohlmann, Marie Schmitz, Malte G. H. Schulte, Ulf Berges, and Carsten Westphal, *Low-dimensional germanium: a structural investigation by means of photoelectron spectroscopy and diffraction*, Graphene Korea 2020, Incheon/Seoul, Korea (2020).

    - supported by German Academic Exchange Service DAAD
      project number: 57520644

4. Lukas Kesper, Marie Schmitz, Julian A. Hochhaus, Malte G. H. Schulte, Ulf Berges, and Carsten Westphal, *2D-germanium: a structural investigation of germanene on Ag(111) by means of photoelectron spectroscopy and diffraction*, Graphene Korea 2021, Incheon/Seoul, Korea (2021).

    - supported by German Academic Exchange Service DAAD
      project number: 57588743

5. Wolfgang Tillmann, Nelson Filipe Lopes Dias, Dominic Stangier, Jasper Berndt, Lukas Kesper, Ulf Berges, Carsten Westphal, Carl Arne Thomann, Jörg Debus, *Rare-earth modified amorphous carbon films: effects of erbium and gadolinium on the structural evolution and mechanical properties*, 31st International Conference on Diamond and Carbon Materials (2021).

    - awarded the Silver Young Scholar Award 2021

6. Lukas Kesper, Marie Schmitz, Julian A. Hochhaus, Malte G. H. Schulte, Ulf Berges, and Carsten Westphal, *On the structural evolution of low-dimensional germanium phases forming 2D germanene on Ag(111) studied by XPS and XPD*, APS March-Meeting 2022, Chicago, IL (2022).

    - supported by German Academic Exchange Service DAAD
      project number: 57609952

7. Julian A. Hochhaus, Lukas Kesper, Stefanie Hilgers, Ulf Berges, and Carsten Westphal, *Investigation of sub-monolayer Sn phases on Au(111)*, DPG Spring-Meeting 2022, Regensburg, Germany (2022).

Others

1. Antrag auf Sachbeihilfe, *Passivierung von zweidimensionalen Materialien – Untersuchung der Strukturbildung und -entwicklung von Germanen als verborgene Grenzfläche unter Isolationsschichten*, WE 1649/9-1, Deutsche Forschungsgemeinschaft (DFG), 2020.

2. Antrag auf ein Forschungsgroßgerät nach Art. 91b GG (HBFG), *Gerät zur hochauflösenden Photoelektronendiffraktion mit Synchrotronstrahlung*,
   INST 212/458-1, Deutsche Forschungsgemeinschaft (DFG), 2020.
   project number: 440925240

Chapter

Danksagung

Zum Abschluss dieser Dissertation möchte ich mich bei denjenigen Personen bedanken, die mich wesentlich in der vergangenen Zeit unterstützt und mir somit diese Arbeit ermöglicht haben.

Zunächst möchte ich Herrn Prof. Dr. Carsten Westphal dafür danken, meine Promotion betreut zu haben und mir dafür die Infrastruktur seiner Arbeitsgruppe zur Verfügung zu stellen. Ich danke Ihnen darüber hinaus für viele fachliche und nicht-fachliche Diskussionen und Gespräche, immer wenn es nötig war, die meinen Forschungsalltag bereichert haben. Ich bin außerdem dankbar für die vielen, nicht selbstverständlichen Chancen, die Sie mir im Rahmen der Promotion ermöglicht haben.
Ich möchte mich ebenso bei Herrn Prof. Dr. Roland Böhmer bedanken, sich dazu bereitzuerklären, das Zweitgutachten dieser Arbeit zu übernehmen.

Ein besonderer Dank gilt meinen aktuellen und auch ehemaligen Bürokolleginnen und Bürokollegen aus der AG Westphal. Zum Trotz der pandemischen Umstände oder Rückschlägen in der eigenen oder gemeinsamen Arbeit, konnten wir stets einen respektvollen und kollegialen Umgang pflegen, in dem ich mich immer sehr wohl gefühlt habe. Ob im Gruppen- oder Kaffeemeeting, in Präsenz oder in ZOOM, für ein gesundes Maß an aufbauenden Worten oder auch den nötigen Humor abseits von Forschungsfragen war verlässlich gesorgt. Speziell betonen möchte ich hier die fachliche, personelle und mentale Unterstützung rund um das XPS-Experiment von Julian Hochhaus, Ulf Berges, Marie Schmitz und Malte Schulte, wofür ich sehr dankbar bin. Zusätzlich danke ich Malte und Julian für das Korrekturlesen dieser Arbeit.

Des Weiteren möchte ich mich für die effektive und produktive Zusammenarbeit mit dem Lehrstuhl für Werkstofftechnologie, stellvertretend bei Dominic Stangier und Nelson Filipe Lopes Dias bedanken.
Ich danke ebenfalls dem Team von DELTA für die Bereitstellung der Synchrotronstrahlung, ohne die diese Arbeit nicht möglich gewesen wäre.

Zuletzt aber nicht zu gering möchte ich mich bei meiner Familie bedanken, für die uneingeschränkte Unterstützung während und außerhalb der Arbeit. Nur durch euer Zutun, unseren Zusammenhalt und die wertvollen Impulse konnte ich dieser Arbeit nachgehen und ich bin dankbar und stolz, jederzeit wieder auf euch vertrauen zu können. Besonders bedanken möchte ich mich für die Unterstützung meiner Freundin Isabelle, die ebenfalls das Lektorat dieser Arbeit übernommen hat.

Vielen Dank für die Unterstützung!